

Impact damage of composite materials

12th Technical Meeting, 1999
Coimbra, Portugal

ON THE COMPRESSIVE DYNAMIC TESTING OF COMPOSITE PLATES

Gérard GARY

Laboratoire de Mécanique des Solides
Ecole Polytechnique, 91128 Palaiseau, France

Han ZHAO

Laboratoire de Mécanique et Technologie - Cachan
Université Pierre et Marie Curie (Paris 6)
61, Avenue du président Wilson, 94235 Cachan Cedex, France

SUMMARY

Experimental investigations of the failure strength of fibre reinforced polymer matrix composite plates under compressive impact loading is presented in this paper. A split Hopkinson pressure bar (SHPB) is used to measure those properties. The specimen being a plate, its cross-sectional area is small compared with the area of the bars and the failure strength is weak. One has then to use low impedance bars made of a viscoelastic material. Subsequent experimental problems, such as dispersion corrections in viscoelastic bars, are analysed. One also has to use a special anti-buckling device to prevent the overall buckling of the specimen. It is shown that the presented SHPB system provides a precise measurement of forces and displacements at both ends of the specimen. A special attention is then given to the analysis of the test, especially in situations where a non-homogeneous state of stress in the specimen is observed.

1. INTRODUCTION

The compressive failure is a design limiting feature of fibre polymer matrix composite plates as it is always much less than the tensile one. Recent researches indicate that this decrease is mostly due to a localised compressive plastic buckling. A review of those problems is given by Budiansky & Fleck [1], mainly concerning studies on the compressive failure strength of composite plates under quasi-static loading.

As the fibre polymer matrix composite is going to be involved in dynamic loading situations, compressive failure strengths under impact loading are required. In the crash situation of automobiles, the composite plates, when used, are indeed submitted to an in-plane compressive impact loading.

For fibre reinforced composite plates, most of studies at high strain rates report the strength of the composite plates under transversal localised impact or piercing behaviour [2-4]. It corresponds to the most frequently found situations. Meanwhile, other tests to determine the energy absorbing capacity or the tensile impact behaviour are also reported [5-6]. A review of works in this field has been written by Cantwell and Morton [7]. As indicated by them, there are no standard impact tests for composites because it is hardly possible to predict their behaviour from one type of loading to

another. Therefore, one should try to perform the experience in a condition similar to the real application.

This paper presents an original testing method to measure the compressive failure strength of composite plates using a viscoelastic split Hopkinson pressure bar (SHPB). Some initial comparative results for glass fibre polymer matrix composites with different fibre directions are presented.

2. IMPACT TEST MEASUREMENT TECHNIQUES

To test composite plates under impact, there are various testing configurations [7]. For relative low strain rates, Charpy or Izod pendulum tests, drop-weight test and rapid servo-hydraulic machine can be used. On the other hand, in the range of high strain rates, SHPB or gas gun impact tests are employed. To perform a compressive failure test, all those configurations could be used. However, the measuring technique is more or less well adapted. The pendulum test is significantly accurate mainly for the measurement of the energy absorption. Signals obtained with drop-weight impact tests or servo-hydraulic machine tests often contain perturbations due to the vibration of the testing machine [8]. It has been proved that for instance those measurements depend on the location of the sensors [9-10].

An adequate measurement technique for impact loading is the Hopkinson bar, which is a widely used experimental technique to study constitutive laws of materials at high strain rates [11-12]. The SHPB test has gained a great popularity in the past decades and many works have contributed to improve the accuracy of the set-up [13-14] and to extend the technique to the tensile (by Harding et al. [15]) and to the torsional loading (by Duffy et al. [16]). The three-dimensional effects in the specimen such as radial inertia and friction have been also studied by Davies & Hunter [17], and more recently by Malinowski & Klepaczko [18]. Those corrections are in agreement with a two-dimensional numerical simulation by Bertholf & Karnes [19]. The assumption of the homogeneous state in the specimen has been also critically analysed by means of the transient wave simulation by Jahsman [20] and by Gary & Zhao [21].

For composite specimen having a cylindrical form, the Split Hopkinson pressure bar technique has already been used in tension or in compression [22-23]. To perform a compressive impact test on plates with SHPB, some specific difficulties such as low impedance specimen effects or prevention of buckling effects must be solved.

3. USE OF SHPB TECHNIQUE

3.1 Classical SHPB analysis

A SHPB setup is composed of long input and output bars with a short specimen placed between them. By the impact of a projectile at the free end of the input bar, a compressive longitudinal incident wave $\varepsilon_i(t)$ in the input bar is developed. This incident wave will induce a reflected wave $\varepsilon_r(t)$ in the input bar and a transmitted wave $\varepsilon_t(t)$ in the output one. With strain gages cemented on the two bars, one can record those three waves which

allow for the determination of the forces and particle velocities at both faces of the specimen.

Assuming that F_{input} , F_{output} , V_{input} , V_{output} denote forces and particle velocities at the specimen-bar interfaces and S_B , E and C_0 are respectively the cross section of the bars, Young's modulus, and the longitudinal wave speed, the following equations are used to obtain forces and velocities at both ends of specimen :

$$\begin{aligned} F_{input}(t) &= S_B E (\varepsilon_i(t) + \varepsilon_r(t)) & V_{input}(t) &= C_0 (\varepsilon_i(t) - \varepsilon_r(t)) \\ F_{output}(t) &= S_B E \varepsilon_i(t) & V_{output}(t) &= C_0 \varepsilon_i(t) \end{aligned} \quad (1)$$

In order to obtain the stress-strain curve of the specimen from the forces and the velocities at both specimen faces, the simplified analysis is limited to the hypothesis of the homogeneity of stresses and strains within the specimen. The result is in the form of equation (Eqn. 2):

$$\dot{\varepsilon}_s = \frac{V_{output}(t) - V_{input}(t)}{l_s} \quad (2.a)$$

$$\sigma_s(t) = \frac{F_{output}}{S_s} \quad (2.b)$$

An improved analysis, when input and output forces are slightly different, consists of using the average of the two forces in the calculation of the stress.

$$\sigma_s(t) = \frac{F_{input} + F_{output}}{2S_s} \quad (2.c)$$

3.2 Viscoelastic SHPB setup

To use SHPB technique to measure the compressive failure strength, one must overcome a major difficulty, which consists in the low crushing force of the tested plates. Indeed, when the force in the specimen is small compared to the force associated with the incident wave, the transmitted wave will be weak, and one has to use a more sensitive measuring device to amplify the signal. On the other hand, $\varepsilon_r(t)$ is almost equal to $-\varepsilon_i(t)$ according to the equation (1). The input force cannot be then precisely measured because of the difference of two almost equal values and there is no way to improve that. The use of common metallic bars to test composite specimens is then difficult, even when the specimen is cylindrical and has the same cross sectional surface as the bar, as shown by Griffiths & Martin [22].

Thus, the SHPB setup made of a low impedance material is needed, for example, PMMA or nylon bars. Those polymeric low impedance bars always demonstrate a viscoelastic behaviour. As compared with a conventional SHPB, the use of viscoelastic bars in a SHPB setup introduces the following complications. The first is due to the wave dispersion in a viscoelastic bar. The second concerns the calculation of stress and particle velocity from the measured strain.

The wave dispersion in an elastic bar has been studied by Davies [24]. On the basis of the Pochhammer and Chree's longitudinal wave solution [25,26] for an infinite cylindrical

elastic bar, a dispersion correction has been proposed. Even though the Pochhammer-Chree solution is not exact for a finite bar, it is easily applicable and sufficiently accurate for long bars. Such a correction is then accepted and applied by many authors [27-28]. On the basis of a similar 3D frequency equation obtained for viscoelastic bars [29], this approach is extended to the case of viscoelastic bars [30]. The solution of this equation gives a dispersive relation between wave's number ξ and frequency ω . Once the dispersive relation is known, one can calculate the wave propagated at a distance Δz , $u_z^p(t)$, from the measured wave $u_z^m(t)$ as follows.

$$u_z^p(t) = FFT^{-1} \left[e^{i\xi(\omega)\Delta z} FFT[u_z^m(t)] \right] \quad (3)$$

Such a correction is very important, especially when dealing with viscoelastic bars. In our case, the input bar is 40 mm in diameter and 3 m long. Figure 1 illustrates this point in the case of a test without specimen where the equality of input and output forces has to be checked. The result without dispersion correction shows a significant gap between both forces.

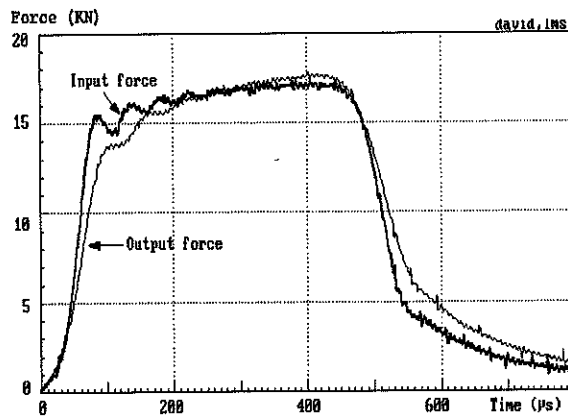


Fig. 1a Input and output forces without dispersion correction

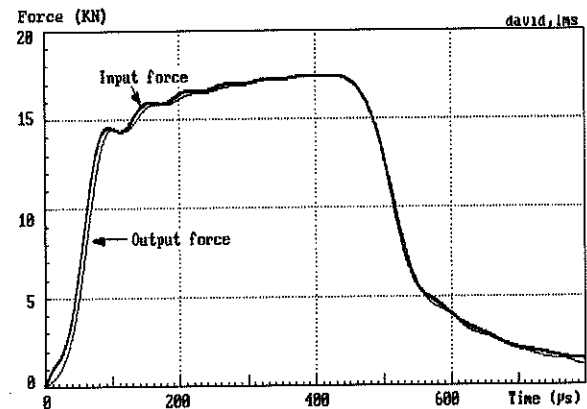


Fig. 1b Input and output forces with dispersion correction

The forces and the particle velocities associated with a viscoelastic wave can be calculated after the strain using the Fourier analysis. When the constitutive relation (complex modulus) of the bar is known, one can find the Fourier coefficients of the stress and of the particle velocity.

4. EXPERIMENTAL

As mentioned by Budiansky & Fleck [1], the most frequent mode of compression failure for composite plates is the localised plastic buckling. The experimental aim is then to determine the failure strength of the studied composite plate in the case of this mode of failure. Therefore, other modes of failure should be avoided in the test.

The contact conditions between the composite plate and the bars could induce a dispersion of the results. The composite plate is not attached to the bar in order to prevent the perturbations of measurements due to additional interfaces [5-6, 22-23]. It is then just in contact with the bars and the probability of elastic buckling is increased with such supporting conditions. To eliminate those effects, the chosen solution is to use honeycomb structures as complementary supports (Fig. 2). Those structures are just placed in contact with the plates so that they can induce a reaction to prevent the overall elastic buckling. Since their stiffness is very weak in the direction of the bars, they cannot perturb the axial measurements made with the SHPB set-up.

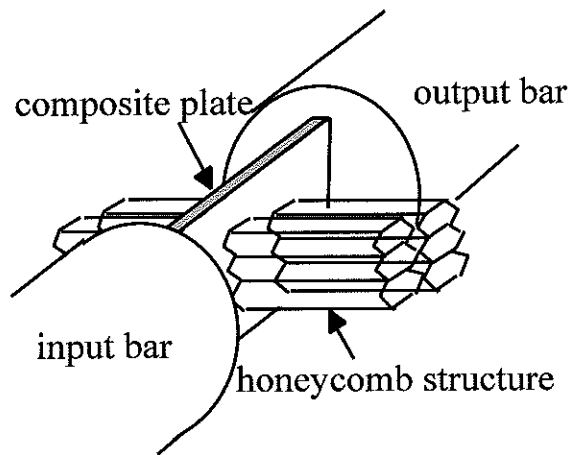


Fig. 2. Detail of the experimental device

The material to be tested is an industrially made glass/epoxy composite plate of 3 mm thickness. Square specimen 36 mm x 36 mm are cut from it. Using the viscoelastic SHPB made of PMMA (Young's modulus being about 6×10^9 MPa), forces and velocities at both ends of the specimen are measured. Using the conventional analysis (Eqn. 2) the average stress and strain rate can be calculated. A typical

result is shown in Fig. 3.

The composite plates exhibit an apparent elastic-plastic behaviour before the failure and they give a response like that of metal beams under impact compression for which a buckling model under impact has been developed [31]. A similar model used for those tests indicates that only local buckling can occur. Experimental results in the fibre direction (0°) are shown in Fig. 4. The increase of the failure strength with the strain rate is observed.

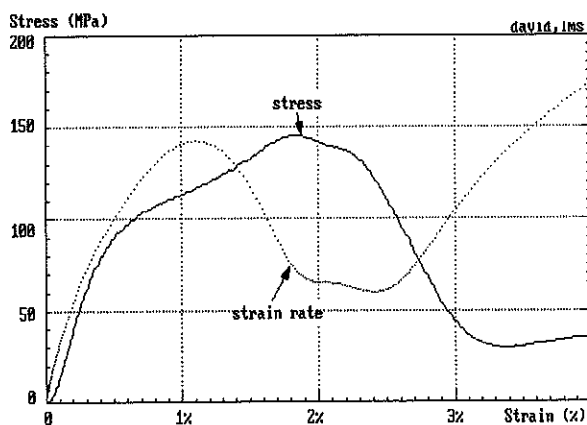


Fig. 3. Stress and strain rate vs. strain

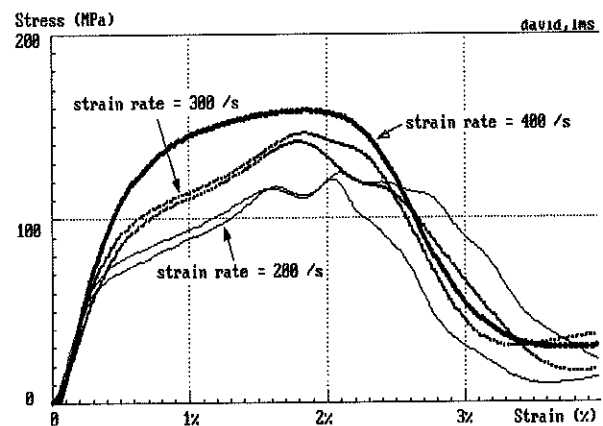


Fig. 4. Influence of strain rates

*A Partale vitrose, on 5 verres
du plombage.*

5. INFLUENCE OF THE FIBRE DIRECTION

The compressive failure model of Budiansky & Fleck indicates a failure strength dependent on the fibre direction. In order to investigate the influence of the fibre orientation, impact tests are done in the fibre direction (0°) and in the direction perpendicular to the fibre (90°) for one-directional fibre plates. Similar results as shown in Fig. 4 have been obtained in the direction perpendicular to the fibre (90°).

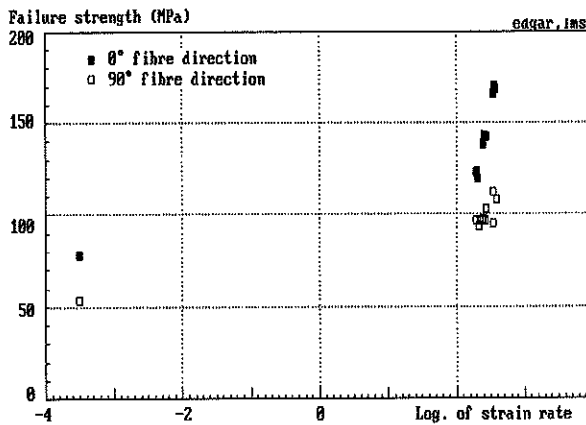


Fig. 5. Failure strength vs. strain rates

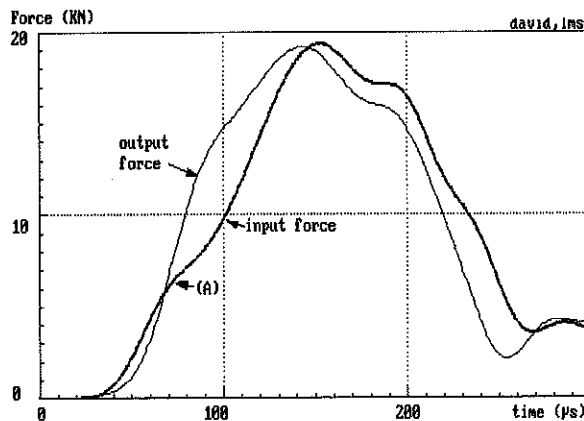


Fig. 6. Input force and output forces

The fibre direction has indeed an influence on the failure strength. A significantly higher failure strength is obtained in the fibre direction (0°) in quasi-static and dynamic cases (Fig. 5). This is in agreement with theoretical results [1]. It shows also that the failure strength in the fibre direction (0°) is more rate sensitive than that in the direction perpendicular to the fibre (90°).

The results presented above are calculated using the classical SHPB analysis (Eqn. 2). The use of such an analysis is correct when stress and strain field are homogenous. This hypothesis is not exactly verified as it can be seen on the example in Fig. 6. To obtain a more accurate and detailed interpretation of the measurements (forces and velocities), a transient calculation [32] using a failure model must be performed. Such a calculation could explain, for instance, the unusual observation of the output force becoming greater than the input one after a short time [33-34] (at point A, Fig. 6). This point could be related to the damage initiation in the composite plate.

6. CONCLUSIONS

Experimental results on the compressive failure strength of glass fibre epoxy matrix composite plates under dynamic loading are analysed. It is observed that the failure strength is rate sensitive. As predicted by the theory used for quasi-static loading, it is also found that the fibre orientation has an influence on the failure strength.

The use of a viscoelastic SHPB setup is an indispensable technique to obtain accurate measurement under an impact loading when low impedance specimens are used. The situation is especially critical for reinforced polymer matrix composite showing a relatively low failure strength. In particular, the measurement of both input and output force is made possible. It shows that the classical analysis of the test can be improved.

REFERENCES

- [1] Budiansky B. and Fleck N.A., Compressive failure of fibre composites, *J. Mech. Phys. Solids*, 41 (1993), 183-211.
- [2] Davies C.K.L., Turner, S. and Williamson K.H., Flexed plate impact testing of carbon fibre-reinforced polymer composite, *Composite*, 16 (1985), 279-285.
- [3] Liu D. and Malvern L., Matrix cracking in impacted glass/epoxy plate, *J. of composite Mater.*, 21 (1987), 595-609.
- [4] Glinicki M.A., Vautrin A., P. Soukatchoff, and Brazier J.F., Plate impact testing method for GRC materials, *Cement & concrete composite*, 16 (1994) 241-251.
- [5] Harding J. and Welsh L.M., A tensile testing technique for fibre-reinforced composites at impact rates of strain. *J. Mater. Sci.*, 18 (1983), 1810-1826.
- [6] Harding J., Impact damage in composite materials, *Sci. and Engng. of composite Mater.*, 1 (1989), 41-68.
- [7] Cantwell W.J. and Morton J., The impact resistance of composite materials - a review. *Composite*, 22 (1991), 347-362.
- [8] Beguelin P. and Barbezat M., caractérisation mécanique des polymères et composites à l'aide d'une machine d'essai rapide, *Proc. 5th Journée Nationale Dymat*, France, 1989.
- [9] Tan T.M. and Sun C.T., Use of statical indentation laws in the impact analysis of laminated composite plates. *J. Appl. Mech.*, 52 (1985), 6-12.
- [10] Genin D., Endommagement de plaques composites sous sollicitation de choc, *Ph. D. thesis*, 1993, Université Claude Bernard-Lyon I, Lyon.
- [11] Hopkinson B., A method of measuring the pressure in the deformation of high explosives by the impact of bullets, *Phil. Trans. Roy. Soc.*, **A213** (1914), 437-452 .
- [12] Kolsky H., An investigation of mechanical properties of materials at very high rates of loading, *Proc. Phys. Soc. London, Series B* **62** (1949), 676-700.
- [13] Kolsky H., *Stress Waves in Solids*, (1963), Clarendon Press, Oxford.
- [14] Lindholm U.S, Some experiments with the split Hopkinson pressure bar, *J. Mech. Phys. Solids*, **12** (1964), 317-335.
- [15] Harding J., Wood E.D. and Campbell J.D., Tensile testing of materials at impact rate of strain, *J. Mech. Engng. Sci.*, **2** (1960), 88-96.

- [16] Duffy J., Campbell J.D. and Hawley R.H., On the use of a torsional split Hopkinson bar to study rate effects in 1100-0 aluminium, *J. Appl. Mech.* **38** (1971), 83-91.
- [17] Davies E.D.H and Hunter S.C., The dynamic compression testing of solids by the method of the split Hopkinson pressure bar, *J. Mech. Phys. Solids*, **11** (1963), 155-179.
- [18] Malinowski J.Z. and Klepaczko J.R., A unified analytic and numerical approach to specimen behavior in the split Hopkinson pressure bar. *Int. J. Mech. Sci.*, **28** (1986), 381-391.
- [19] Bertholf L.D. and Karnes J., Two-dimensional analysis of the split Hopkinson pressure bar system, *J. Mech. Phys. Solids*, **23** (1975), 1-19.
- [20] Jahsman W.E., Reexamination of the Kolsky Technique for measuring dynamic Material behavior, *J. Appl. Mech.*, (1971), 77-82.
- [21] Zhao. H and Gary G., On the use of SHPB techniques to determine the dynamic behavior of materials in the range of small strains. *Int. J. Solids & Structures.* **33** (1996) 3363-3375
- [22] Griffiths L.J. and Martin D.J., A study of the dynamic behavior of carbon-fibre composite using the split Hopkinson pressure bar. *J. Phys. D: Appl. Phys.* **7** (1974), 2329-2341.
- [23] Sierakowski R.L., Nevill G.E., Ross, C.A., and Jones E.R., Dynamic compressive strength and failure of steel reinforced epoxy composites. *J. composite mater.*, **5** (1971), 362-377.
- [24] Davies R.M., A critical study of Hopkinson pressure bar, *Phil. Trans. Roy. Soc.*, **A240** (1948), 375-457.
- [25] Pochhammer L., Uber die Fortpflanzungsgeschwindigkeiten Kleiner Schwingungen in einem Unbergrenzten Isotropen Kreiszyylinder, *J. für die Reine und Angewande Mathematic*, **81** (1876), 324-336.
- [26] Chree C., The equations of an isotropic elastic solid in polar and cylindrical co-ords., their solutions and applications, *Cambridge Phil. Soc.*, Trans. **14** (1889), 250-369.
- [27] Follansbee P.S. and Franz C., Wave propagation in the split Hopkinson pressure bar, *J. Engng. Mater. Tech.*, **105** (1983), 61-66.
- [28] Gong J.C., Malvern L.E. and Jenkins D.A., Dispersion investigation in the split Hopkinson pressure bar, *J. Engng. Mater. Tech.*, **112** (1990), 309-314.
- [29] Zhao H. and Gary G., A three dimensional analytical solution of longitudinal wave propagation in an infinite linear viscoelastic cylindrical bar. Application to experimental techniques, *J. Mech. Phys. Solids.* **43** (1995), 1335-1348.
- [30] Zhao H., Gary G. and Klepaczko J.R., On the use of a viscoelastic split Hopkinson pressure bar, *Int. J. Impact Engng.*, **19**(1997), 319-330.
- [31] Gary, G. Dynamic buckling of an elastoplastic column, *Int. J. Impact Engng.* **1**, (1983),357-375.
- [32] Zhao H., A study of specimen thickness effects in the impact tests on polymers by numeric simulations, *Polymer*, **39**(1998) 1103-1106.
- [33] Zhao H., A study on testing techniques for concret-like materials under impact loading. *Cement & concrete composites*, **20**(1998) 293-299.
- [34] Gary G. and Zhao H., Measurement of dynamic behaviour of concrete under impact loading, In: *Proc. 2nd Int. Symp. on Impact Engng.* Beijing, China, 208-213 (1996).

DYMAT 99 Technical Meeting
Coimbra, Portugal, October 14/15, 1999

PENETRATION PERFORMANCE OF COMPOSITE MATERIALS AND COMPOSITE STRUCTURES

H.-J. Ernst, K. Hoog, T. Wolf

French-German Research Institute of Saint-Louis (ISL)
PO 34, F-68301 SAINT-LOUIS CEDEX, France

Depth of penetration (DOP) experiments with long rods (tungsten alloy, $D=7.25$ mm, $L=20 \cdot D$) impacting differently thick target blocks (100×100 mm²) with high velocities (1800 m/s) yield residual penetrations in a steel-backing (RHA) which indicate the ballistic performance of the material itself as well as the target construction. In a first step composite materials (GRP) are compared with ductile and brittle target materials. In a second step composite targets are investigated consisting of sandwich constructions made of armour steel and promising brittle materials.

The first aim of this investigation is to separate the dependence of the material of a target layer on the protective power from the influence of its environment, e.g. confinement or the neighbouring layers. It has been proven for brittle materials that one material parameter, called ductile limit of the equivalence factor, sufficiently describes the protective power of the target material under consideration. An attempt is made to apply the same approximation for composite materials.

The final aim of the research is to optimise the material choice as well as the sandwich design, concerning the protection potential of the target against a high velocity long rod threat.

INTRODUCTION

Brittle materials such as industrial ceramics and glass as well as composite materials such as GRP (*Glass- Fibre Reinforced Plastics*) are often applied to design light weight armours. The protective power of these inert materials against KE-threat ($KE = \text{Kinetic Energy}$) is generally evaluated by DOP experiments ($DOP = \text{Depth Of Penetration}$) with cylindrical projectiles. The impact velocities are sufficiently high to ensure a perforation of the blocks and a measurement of the residual penetration depths in a thick steel backing directly fixed to the block. By analysing the penetration performance in the considered target (i.e. block of target material plus backing) in comparison with the one achieved in a reference steel block of semi-infinite thickness, different ballistic parameters may be calculated to describe the protective power of the material.

The ballistic protective power of an inert material against a given threat depends on the target layer thickness as well as on the constructive configuration which is often called confinement [1]. It is known from literature and from our own experiments that the ballistic performance of brittle materials decreases with increasing block thickness [2, 3, 4]. Furthermore, it has been shown that the protective power of several brittle materials is all the higher as they are better confined [5, 6, 7]. Additionally, a ballistic parameter has been developed allowing a joint protective power ranking of brittle and ductile materials.

This investigation has two aims: Firstly, the thickness and confinement dependent protective power of composite materials (GRP) is evaluated using the above mentioned assessment. Secondly, composite target structures consisting of steel-ceramic-steel sandwiches of constant volume are compared by looking for an optimal ceramic layer position.

EXPERIMENTAL DESIGN

An APDSFS-projectile (APDSFS = *Armour Piercing Discarding Sabot Fin Stabilised*) developed at ISL is used as KE-threat: [figure 1](#). The cylindrical penetrator made of tungsten heavy alloy (DX2HCMF, manufacturer Cime



Figure 1: APDSFS-projectile BMU G 154

heavy alloy (DX2HCMF, manufacturer Cime Bocuse/France, $\rho = 17.6 \text{ g/cm}^3$) has a length of 145 mm and a diameter of 7.25 mm. Related to the 120-mm-calibre, the scale factor is 1 : 3.5. The projectile is accelerated in a smooth barrel of 40 mm calibre by a sabot in four parts made of light metal. At an impact velocity of 1800 m/s it penetrates approxi-

mately 160 mm into RHA (*Rolled Homogeneous Armour*, an armour steel of medium strength about 800 N/mm^2).

Inert target materials have been tested in three configurations, called unconfined, laterally confined and totally confined. [Figure 2](#) schematically shows the target set-up for these DOP-experiments. In the unconfined configuration the target block is directly placed on an RHA-backing of semi-infinite thickness. A laterally confined configuration is encased by steel plates of 20 mm thickness. If an additional front plate with a hole in the impact region is added, the configuration is called totally confined. The hole is necessary in order to have comparable impact conditions for all three configurations.

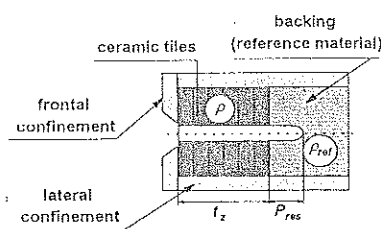


Figure 2: Schematic drawing of target configurations

The target blocks have different thicknesses ($<140 \text{ mm}$) and consist of differently thick layers, which have lateral dimensions of $100 \times 100 \text{ mm}^2$. In the first part the protective power of two composite materials (GFK_01 and GFK_02) mounted in two configurations (unconfined and totally confined) is compared with that of formerly investigated other inert target materials (Al_2O_3 , B_4C , SiC , Si_3N_4 and TiB_2 , glass, high hardness steel and titanium).

In the second part a 20-mm-thick ceramic tile (B_4C , SiC , or TiB_2) is placed in different positions within a totally confined 100-mm-thick sandwich in front of the same RHA-backing; 80 mm of the sandwich thickness consist of HHS plates (*High-Hardness Steel*).

ANALYSIS OF THE DOP-EXPERIMENTS

In the RHA-backing behind the investigated target a residual penetration P_{res} is measured. This ballistic result is compared to the penetration of the projectile at the same velocity in the RHA reference material of semi-infinite thickness P_{ref} . In the case of a homogeneous target block (several layers of one material) the influence of its total thickness t_z is analysed. For the composite sandwich with a constant total thickness of 100 mm the thickness of the first steel plate t_1 in front of the ceramic tile (varying from 0 to 80 mm) is taken as the characterising design parameter.

In order to eliminate the experimentally caused scattering of the impact velocity these two parameters as well as the residual penetration are normalised:

$$t_{z,n} = t_z / P_{ref}, \quad t_{1,n} = t_1 / P_{ref}, \quad \text{and} \quad P_{res,n} = P_{res} / P_{ref}.$$

Though the ballistic performance of the projectile is directly given by the residual penetration in the backing, it is advantageous to define so-called ballistic equivalence factors. They describe the volume gain (subscript s) and the mass gain (subscript m) respectively, of the target block under consideration as compared to an equivalent layer of the reference material that yields the same P_{res} . The volume equivalence factor is defined as

$$F_s = (1 - P_{res,n}) / t_{z,n};$$

if it is multiplied by the density relation ρ_{ref} / ρ (ρ_{ref} = reference material density, ρ = average density of the target) the mass equivalence factor is obtained.

If the projectile hits an unconfined brittle target, the material in front of the interaction zone between projectile tip and crater bottom is pre-fractured by shock and stress waves which run ahead of the penetrator. As these waves have finite propagation velocities, there exists a limit of penetration depth for every given target configuration below which reflected waves cannot cause a predisturbance of the material in front of the impactor. So the beginning of the penetration process is not influenced by confinement measures relatively far away from the impact zone. Consequently, it was assumed in former investigations on ceramic targets that the space equivalence factor for vanishing block thickness reaches the same limit value for all configurations [8]. This hypothesis leads to an appropriate approximation algorithm for the exponential fitting function

$$F_s = F_s(0) \cdot \exp(-\gamma \cdot t_{z,n}),$$

where $F_s(0)$ has the same value for all the confinement configurations. The approximation coefficient γ depends on both the ceramic material and the target configuration.

In order to describe the relation between brittleness and confinement, [figure 3](#) shows qualitative diagrams of such approximation functions for F_s (right-hand side) and $P_{res,n}$ (left-hand side) dealing with a hypothetical brittle material in five different target configurations. The thick horizontal line in the F_s diagram marks the quasi-ductile penetration behaviour which is also found in the linear relation in the $P_{res,n}$ diagram ($\gamma = 0$). The non-linear penetration curves are represented by $\gamma > 0$. Increasingly dashed lines signify increasing γ -values, which means a decreasing confinement strength and a decreasing protective power for a constant target thickness and an increasing ballistic limit thickness $T_{z,n}$ of the target [5, 6, 8].

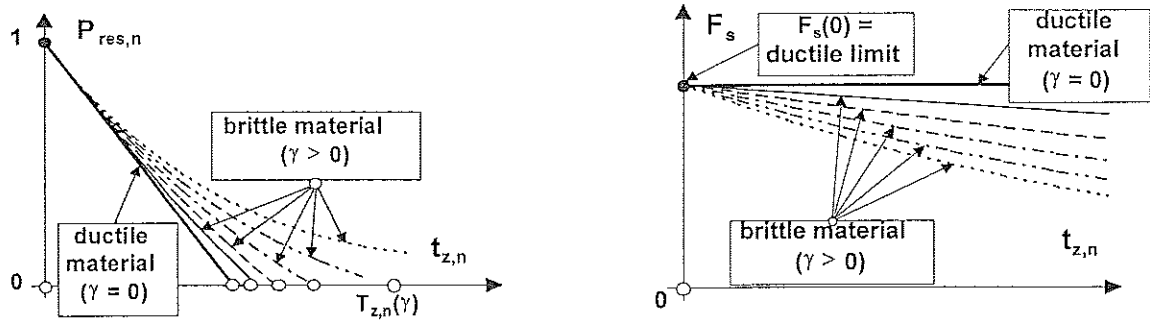


Figure 3: Schematic diagrams of residual penetration and volume equivalence factor as a function of the material thickness for a hypothetical brittle material in different target configurations

$F_s(0)$ is the highest possible space equivalence factor of a brittle material which equals the one occurring in an optimally confined target where the penetration behaviour of a ductile material can be reached. Consequently, it characterises the above-mentioned ductile limit. In this sense the ductile limit of the volume equivalence factor is a material parameter characterising the behaviour of a brittle material under the considered ballistic loading [9].

For the composite materials under consideration the dependence of the space equivalence factor on target thickness and confinement is analysed with the same approximation algorithm to compare the penetration behaviour of these materials to the former investigated ductile and brittle ones.

The evaluation of the results of composite targets (steel-ceramic-steel sandwiches) is less complex. Here a first analysis attempt contents with the dependence of the space equivalence factor on the position of the ceramic layer, defined by the thickness of the first steel plate.

RESULTS

a) Optimal Ceramic Layer Position in a Composite Target

Figure 4 shows the space equivalence factor as a function of the normalised thickness of the first steel plate in front of a 20-mm-layer of the three ceramics (B_4C , SiC , and TiB_2). All the considered ceramic materials exhibit the same tendency: The F_s -value of the sandwich significantly decreases with increasing thickness of the first steel plate: the 20-mm-ceramic-layer should be placed in front of the steel plates of the target to achieve the maximum protective potential. That means for a real three layer sandwich containing one 20 mm thick ceramic tile that the first steel plate which is perhaps necessary as a protection against small calibre threats or fragments should be as thin as possible.

The above-mentioned predisturbance of a thick ceramic block which is caused by shock and stress waves induced by the impacting projectile will also occur in the ceramic layer of the sandwich a relatively long time before the projectile has perforated the frontal steel plate(s). A hole in the impact region of the frontal steel plate as it is used in the totally confined configuration of the DOP experiments, see fig. 2, would avoid the pre-fracturing. Of course, such a predefined impact region cannot be given for a real sandwich target

and therefore the totally confined DOP-results are not comparable to those of the three-layer-sandwich. The amount of predisturbance is influenced by the contact between steel plate and ceramic layer: thin air gaps or adequate damping measures will reduce the energy of the transmitted waves.

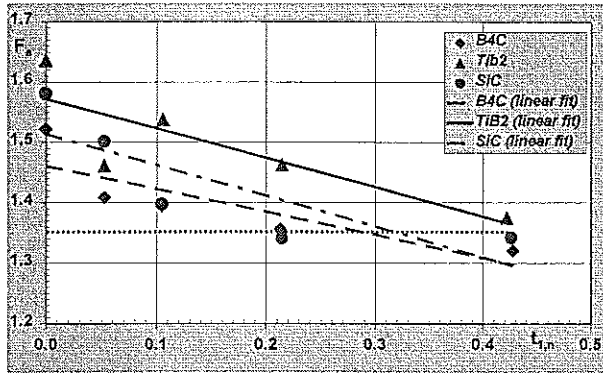


Figure 4: Space equivalence factors of composite targets as a function of the thickness of the first steel plate

Additionally, in fig. 4 a dotted horizontal line is given which represents the mean value (1.35) for the space equivalence factor of a 100-mm-thick homogeneous HHS target (the material which is used in the composite sandwiches). It is obvious that only the TiB₂ layer yields a gain of protective power in all the positions as compared to the HHS block. In the cases of B₄C and SiC the experimental results with a frontal steel plate of 40 mm already reach the F_s-value of the HHS target.

b) Ballistic Performance of Composite Materials (GRP)

1. PROTECTIVE POWER

Detailed results of the DOP experiments with the considered GRP materials, as well as for TiB₂ as an example of a brittle material are presented in figure 5. Each diagram shows

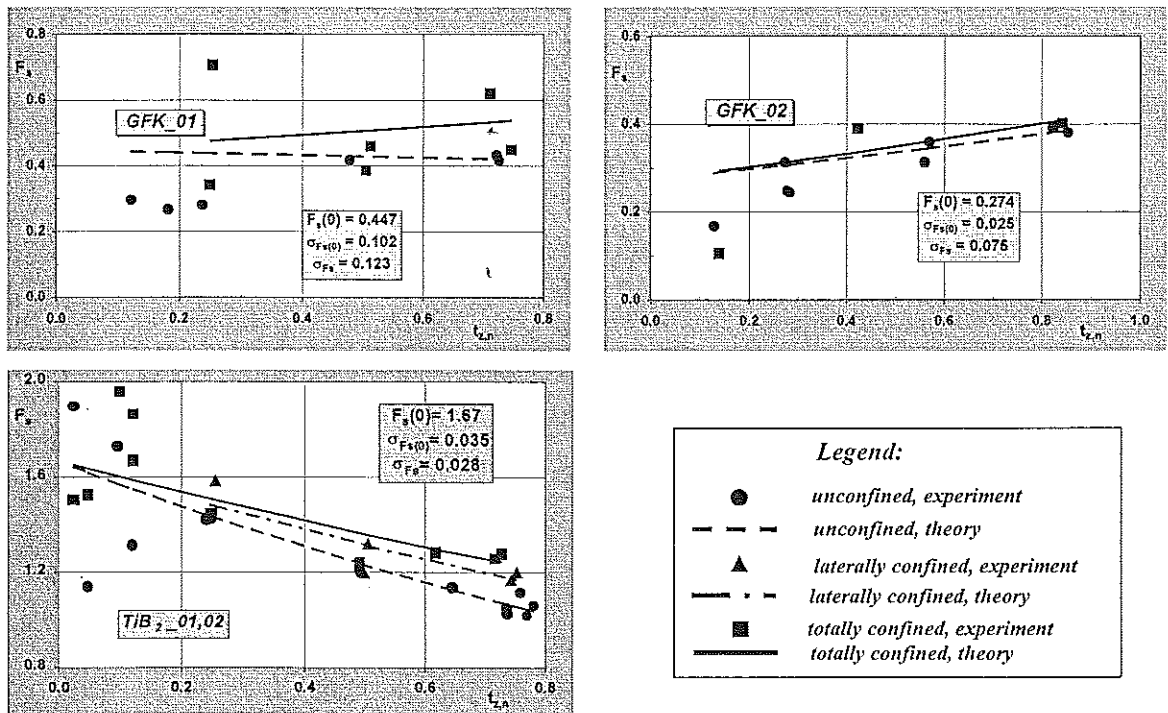


Figure 5: F_s-dependence on t_{z,n} for GFK_01, GFK_02 and TiB₂

experimentally determined F_s-data as well as F_s(t_{z,n})-curves calculated by using the approximation algorithm for the investigated confinement configurations (i.e. for GRP: unconfined and totally confined, and in addition for TiB₂ laterally confined).

The $t_{z,n}$ -dependence of the space equivalence factor of the considered GRP materials significantly differs from the one of the exemplarily shown ceramic material TiB_2 . Only the unconfined configuration of the composite material GFK_01 yields an approximately constant F_s indicating the thickness independence of a ductile material (compare fig. 3). Moreover, the totally confined GFK_01 as well as both configurations of GFK_02 show with a sufficiently high confidence that their space equivalence factors increase with the target thickness. This means that a thick composite block has a higher mean value of the relative protective power than a thin one or, in another interpretation, the target resistance grows with increasing penetration depth. In this context the $F_s(0)$ -value of a GRP material should not be considered as a ductile limit which was introduced for brittle materials. Possibly, a second ballistic material parameter exists for composite materials given by the upper limit of the space equivalence factor. On the other hand, the $F_s(0)$ -values of the GRP materials are considerably lower than the ductile limit of TiB_2 which was the highest one of all ceramics.

The $F_s(0)$ -values of both composite materials are even lower than those of all previously

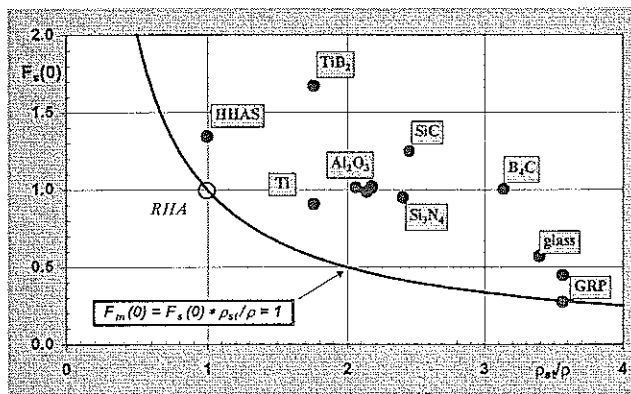


Figure 6: Ballistic material ranking, based on the $F_s(0)$ -value of the space equivalence factor

investigated brittle and ductile materials which can be seen in the material ranking of figure 6. Here, the basic ballistic material parameter $F_s(0)$ is plotted versus the density relation ρ_{st}/ρ . Both, the increasing ductile limit of space equivalence, and the increasing density relation indicate a growing protective power.

The thick hyperbolic line for $F_m(0)=1$ separates the region of mass loss from the one of mass gain of inert target materials as compared to the reference target material RHA. All investigated inert target materials with the exception of GFK_02 are situated in the region of mass gain. But, considering the $F_s(t_{z,n})$ -curves of fig. 5, it has to be remarked, that thicker GRP targets yield a higher mass gain than the $F_m(0)$ -value indicates, e.g. 1.6 for GFK_01, which has the same magnitude as titanium. Therefore GRPs are interesting materials for light armour design.

2. PENETRATION BEHAVIOUR

A first possibility to interpret the growing ballistic resistance during the penetration of a KE-projectile into GRP targets is given by the entrance crater in the backing after the perforation of a GRP block. By comparing the entrance craters in the first backing plate directly behind a thin and a thick GRP target, as shown in figure 7, it seems to be possible to assign two different diameters of the projectile tip after perforation of the GRP to the block thicknesses, respectively to the GRP penetration depths.

The variation of the crater diameter with increasing block thickness of the composite targets is quantified in the diagram of figure 8. Three different diameters were measured: The maximum diameter at the front side $D(0mm)$ yields the beginning of the cratering in the backing. A diameter in a depth of 5 mm $D(5mm)$ approximately marks the transition to the stationary phase of the penetration process in steel. The minimum diameter



Figure 7: Crater entrance in the backing ($100 \times 100 \text{ mm}^2$) behind a 23-mm thick (left) respectively 138-mm thick (right) GFK_02 block

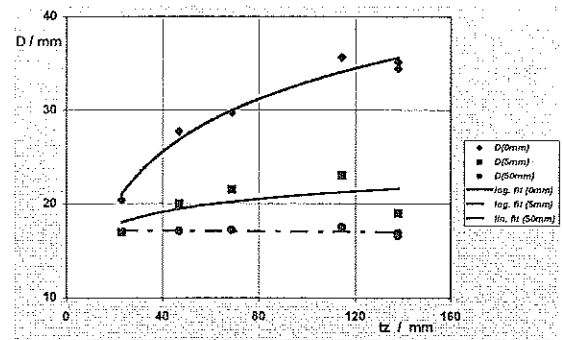
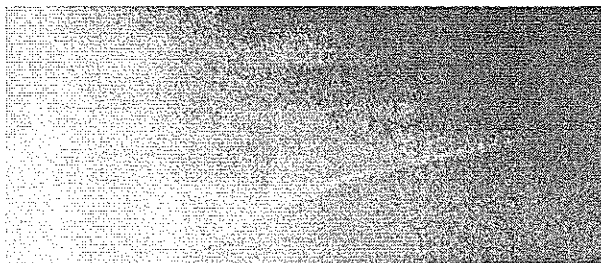


Figure 8: Crater diameters in the first backing plate behind differently thick GRP blocks

$D(50\text{mm})$ measured at the rear side of the backing plate is nearly constant and corresponds to the crater diameter in steel.

The increase of the entrance diameter $D(0\text{mm})$ with increasing block thickness $t_{z,n}$ may be explained by an enlarged mushrooming of the projectile during the penetration in GRP. This hypothesis is encouraged by looking at the double exposed X-ray picture of figure 9.



VN 33068, $v_z=1785 \text{ m/s}$, $\Delta t \approx 40 \mu\text{s}$, $t_z=138 \text{ mm}$

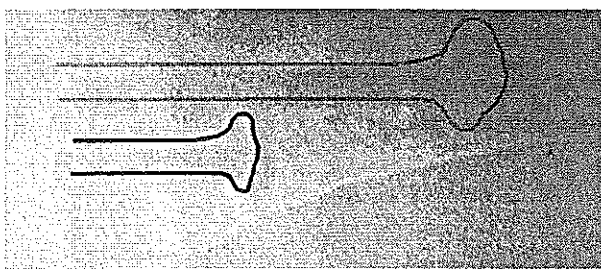


Figure 9: Eroding rod during the penetration in a thick GRP target, double exposed X-ray picture (lower picture with assumed tip contour)

The quality of the exposures is relatively poor, because this X-ray set-up is normally used for flight control of the impacting projectile. Nevertheless, the contours of the mushrooming projectile at two penetration depths with a time delay of $40 \mu\text{s}$ can be imagined as it is marked in the lower picture. In the upper contour corresponding to the deeper penetration depth an enlargement of the projectile tip seems to be visible. Of course, this phenomenon needs further verifications to be able to identify the governing mechanism of the GRP behaviour under high velocity impact loading. A first working hypothesis is based on the statement of the Tate model that density is one of the target material parameters controlling the penetration process [9]. Consequently, a density growth in front of the penetrating projectile may be assumed in accordance with other experiences in impact loading of GRP plates [10].

But looking at all ballistic results available today it is obvious that GRP is a material of which the target resistance increases during the penetration process in contrast to the experiences made with brittle and ductile target materials.

But looking at all ballistic results available today it is obvious that GRP is a material of which the target resistance increases during the penetration process in contrast to the experiences made with brittle and ductile target materials.

CONCLUSIONS

The formerly approved protective power evaluation on the basis of the thickness dependence of space equivalence factor which yields for brittle materials a well defined ballistic material parameter named ductile limit was applied to two composite materials

(GRP). In contrast to the brittle and ductile materials the considered GRPs showed increasing equivalence factors with increasing target thickness. So $F_s(0)$ is not the highest F_s -value and probably not the only ballistic material parameter.

Though the $F_s(0)$ -values of the considered composite materials were relatively small, the $F_m(0)$ -value and/or the increasing mass gain of thick GRP blocks reach the protective power potential of titanium. Therefore these materials remain interesting for light weight armour applications.

The diagnostics of the penetration phenomena, the physical interpretation of the ballistic resistance increase during the penetration of GRP materials have to be improved. A density growth in front of the penetrating projectile as a possible explanation of the governing mechanism has to be confirmed in further investigations.

For the considered composite sandwich target it turned out, that a steel plate in front of the ceramic tile made of B_4C , SiC , or TiB_2 should be as thin as possible. Further investigations will be done by varying ceramic tile thicknesses as well as tile number and ceramic materials.

REFERENCES

- [1] Westerling L., Lundberg T., "The Influence of Confinement on the Protective Capability of Ceramic Armour at Two Different Velocities", 15th Int. Symp. on Ballistics, Jerusalem, Israel, 1995, Vol. 1, pp. 283-290
- [2] Andersen Jr. C.E., Walker J.D., Lankford J., "Investigations of the Ballistic Response of Brittle Materials", SWRI-Technical Report, 1995
- [3] Yaziv D., Parton Y., "The Ballistic Efficiency of Thick Alumina Targets against Long Rod Penetrators", 14th Int. Symp. on Ballistics, Quebec, Canada, 1993, Vol. 2, pp. 331-340
- [4] Hauver G.E., Netherwood P.H., Benck A.F., Gooch W.A., Perciballi W.J., Burkins M.S., "Variation of Target Resistance During Long-Rod Penetration into Ceramics", 13th Int. Symp. on Ballistics, Stockholm, Sweden, 1992, Vol. 3, pp. 257-264
- [5] Ernst H.-J., Hoog K., Wiesner V., "Ballistic Impact Behaviour of Some Ceramics in Different Environments", EURODMAT 94, Oxford, UK, J. Phys. IV, Coll. C8, Suppl. J. Phys. III, Vol. 4 (1994), pp. 677-682
- [6] Ernst H.-J., Hoog K., Wiesner V., Wolf T., "DOP and Continuous Cratering Measurements in Differently Confined Ceramics", 1st Europ. Arm. Fighting Vehicle, RMCS, Shrivenham, UK, 1996
- [7] Rupert N.L., Grace F.E., "Penetration of Long Rods into Semi-infinite, Bi-element Targets", 14th Int. Symp. on Ballistics, Quebec, Canada, 1993, Vol. 2, pp. 469-478
- [8] Hoog K., Ernst H.-J., Wolf T., "A New Parameter Characterising the Ballistic Performance of Ceramics", EURODMAT 97, Toledo, Spain, J. Phys. IV France 7, Coll. C3, Suppl. J. Phys. III, (1997), pp. 241-246
- [9] Tate, A., "A Theory for the Deceleration of Long Rods After Impact", J. Mech. Phys. Solids, Vol. 15, 1967, p. 387ff
- [9] Hoog, K., Ernst, H.-J. "Ductile Limit of the Ballistic Response of Steel Backed Ceramics", 17th Int. Symp. on Ballistics, Midrand, South-Africa, 1998, Vol. 3, pp 57-64
- [10] Unckenbold, W.F., personal communication, 1999

DYNAMIC FRACTURE OF GRAPHITE-EPOXY LAMINATES UNDER IN-PLANE IMPACT LOADING

F.G. Benitez

School of Engineering, University of Sevilla
Av. Camino de los Descubrimientos, Sevilla-41092, Spain
e-mail: benitez@cica.es

ABSTRACT

Results for in-plane impact loaded carbon-epoxy composite plates, and the use of optical techniques applicable to composites by the careful preparation of the surfaces necessary to get images of sufficiently low noise level, are included.

Along this paper an experimental set-up for visualizing cracks propagating under impact loads is presented. The objective is to determine crack length versus time and, from it, to obtain the propagating speed. In addition to this the set-up is also used for monitoring strain gradients versus time by means of the optical method of caustics and diffractive Moire during the dynamic process.

1. INTRODUCTION

Two of the most noteworthy characteristics that qualify carbon-fibre-epoxy resin composite materials for being used in engineering applications are the high strength and stiffness per unit of weight. These two attributes make this material particularly attractive for its use in mobile structures. On the other hand, this application reveals one of the greatest disadvantages of this material: its low strength to impact loadings and, in particular, the difficulties in detecting the damages produced by this type of loadings.

The somewhat low impact resistance of composite materials has limited the broad use of these materials in aircraft structures. Various modes of impact damage of laminated composites exist. Low velocity impact normal to laminated panels (as when dropping a tool on an airplane wing) will cause internal resin failure and delamination [11,5]. The damage will cause loss of stiffness and is difficult to detect visually. Tougher matrix material will improve the resistance. High velocity impact normal to the laminate will cause tear-out, with damage to a smaller part of the surrounding material [3]. The damage resistance can be improved through use of woven fabric rather than UD material, and choosing tougher fibres such as Kevlar, where large amounts of micro failures around each filament and energy demanding fibre pull-out will absorb the impact energy, and prevent penetration [10]. There have been a great number of studies on the bending-type impact on plates or beams, but very few on the through-the-thickness response [7]. When a small object strikes on a composite skin, the problem can be divided into two of different scales. The first is the propagation of compression waves perpendicular to the plate plane. The second is the bending of the laminate. The time required for the waves to travel the distance between the two outer surfaces of the plate is very short compared to the characteristic time for bending, therefore the two problems can be analyzed independently. In-plane impact, as birds hitting the outer guide vanes of a jet-engine or floating objects hitting the wings of a hydrofoil

boat etc., can also cause matrix and/or fibre failure. Low velocity impact can be prevented from initiating damage by ensuring a resin rich leading edge. Damage caused by high velocity impact can be reduced by carefully choosing the fibre type and architecture. Analogously to the out-of-plane impact case, the approach to the in-plane impact problem would follow two family of studies. The first corresponds to loadings with a high rate where the mechanisms of failure are governed by compression and traction stress waves. The second one is guided by bending waves. The waves implied in these two cases differ in at least one order of magnitude, and characterization of mechanisms of both problems can be investigated separately.

The behaviour of laminated composites is therefore important to characterise, and the impact resistance of these materials is desirable to find related to the impact loading nature.

This paper reports on additional investigation carried out in this last type of response [2], the specimens are loaded with a plane wave traveling in a direction parallel to the laminate plane. The goal pursuit is to assess the severity of through-the-thickness cracks by determining propagation and arrest parameters. We start with a description of the test-rig which can be used for the purpose, and how the individual parts of the apparatus are interfaced to consort; followed by the basics of the optical technique used for monitoring the dynamic event. Section 3 focusses on the specimens tested and the results obtained. Finally, the last section is dedicated to some concluding remarks and the outline of future research directions.

2. EXPERIMENTAL SETUP AND BACKGROUND

2.1. Description and Instrumentation

The test rig is basically an air gun that impels a steel bar against the specimen, which is supported by a holder. A schematic draw is shown in figure 1. The loading rig comprises a compressed air reservoir for accelerating the striker bar towards a second bar (input bar). The striker bar speed is captured by a velocity measuring device.

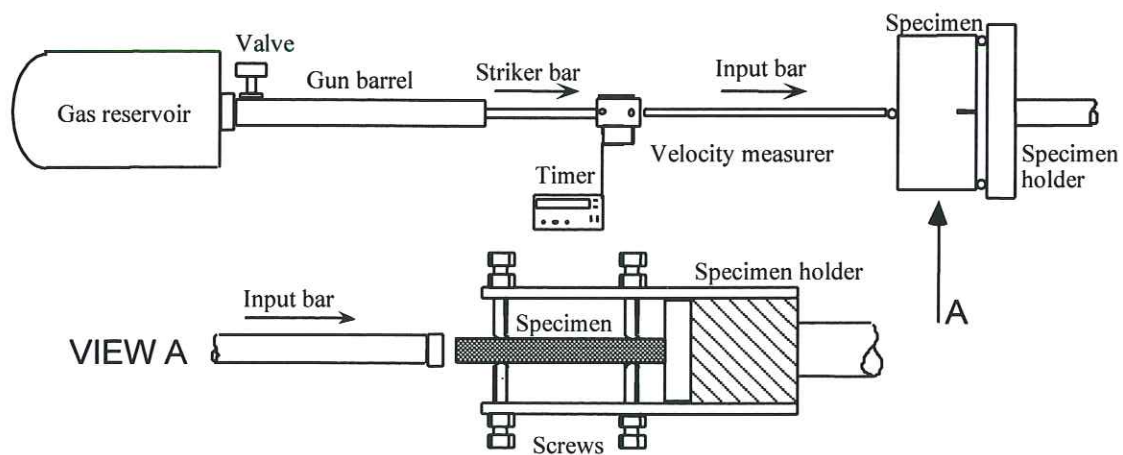


Fig. 1. Schematical view of the test rig.

The specimen holder and the input bar form a three point bending rig, where the strain wave traveling through the input bar causes an impact action-force on the specimen, and the specimen holder the two reaction-forces. The specimen is held so that the impact load causes a crack to grow from the notch towards the point of impact, and provisions are made so the specimen can be accurately aligned with the striker bar and input bar, to avoid compression-bending coupling and flexural waves in the input bar.

The event is recorded using a Cordin high speed film-camera capable of capturing 500 frames at up to 200,000 pictures per second (fps), and a high speed video-camera with a speed of up to 40,500 fps. Both systems can be used independent or simultaneously for monitoring crack and additional optical parameters.

For illuminating the whole event a laser beam is used as light source, which is expanded up to a collimated beam of 10 cm diameter. The film-camera is provided with a mechanical shutter which opens early enough previous to the time-window the event takes place and closes far after the period of interest, this forces the experiment to be carried out in darkness.

An operational amplifier with a latch up circuit is used for triggering the illumination in from the signal given by one of the photodiode used by the bar-speed measurer. The illumination is extinguished when a tacho signal from the film-camera is received corresponding to the instant the whole film has been fully exposed. This procedure precludes a multiple exposition of the film. The same signal that triggers the illumination in is used for triggering the video-camera, which runs till it reaches a fixed number of images (1,024 pictures).

An Ion laser of 6 Watts in continuous wave was used to provide a collimated beam of single wave length (514 nm, 2.4 w.), coherent vertical polarised light. An acousto-optical cell was used to provide a means of rapid on-off switching of the laser beam, in order to expose the camera-film the correct amount of time. When this modulator is activated an amount (95 %) of this light (1st order beam) is bled off, through an iris which is lined-up with the beam-expander optics. This portion of the laser beam is then expanded to provide the required light source for the illumination of the specimen.

After illuminating the specimen by the collimated light, this is directed to a lens arrangement in order to visualize the crack tip neighbourhood during the process of testing. This technique is used due to the specimen opacity, which forces to work under reflexion. The created image is sent to both cameras, the film-camera and the video-camera, by using a beam splitter situated so that the reflected light from the specimen can be directed to both of them simultaneously for capturing purpose.

The test rig is designed to accommodate plate specimens with maximum dimensions of up to 300x200x30 mm. The specimens are opaque. In order to have a flat reflector, needed for the application of the optical methods by reflexion, a half-a-wavelength flatness surface has to be created. Owing to the inevitable imperfections of woven composites in and near the surface, this had to be covered. The coating needs to be thin, so it does not affect the behaviour of the composite and elastic so it follows the deflections without cracking. This was achieved by grinding the surface to be observed, coating it with a thin resin-coat film cured under pressure over a flat glass panel to give a plane and perfectly smooth surface and claded with a layer of vapour deposited aluminium, to obtain a reflective surface, see figure 7. A distance grid in a contrasting colour was also applied to the specimen in order to evaluate the crack tip position versus time.

2.2. Loading Technique

After specimen, camera and optics have been set up and adjusted, cameras are started, and when the set speed is reached in the rotating drum (for film-camera), both cameras are armed. When executing the test, the camera shutter is opened immediately before the quick release valve of the compressed air reservoir is opened and the shutter timer set to close it shortly after. This is to minimize any unwanted stray light exposing the film.

The use of laser as the light source requires a similar procedure to the one outlined above. The acousto-optical cell is driven by a modulator which must be switched on just before the impactor hits the specimen and off just before the film-camera begins a second exposition of the film. The camera writing time is large enough to capture the time-window through which the crack propagates.

2.3. Optical Techniques

Two different optical techniques have been used for monitoring the strain field surrounding the tip of the crack. The first is a local field method: caustics, the second one corresponds to a full field procedure: Moire diffraction.

A schematic of the optical arrangement for the application of the caustic technique is depicted in figure 2.

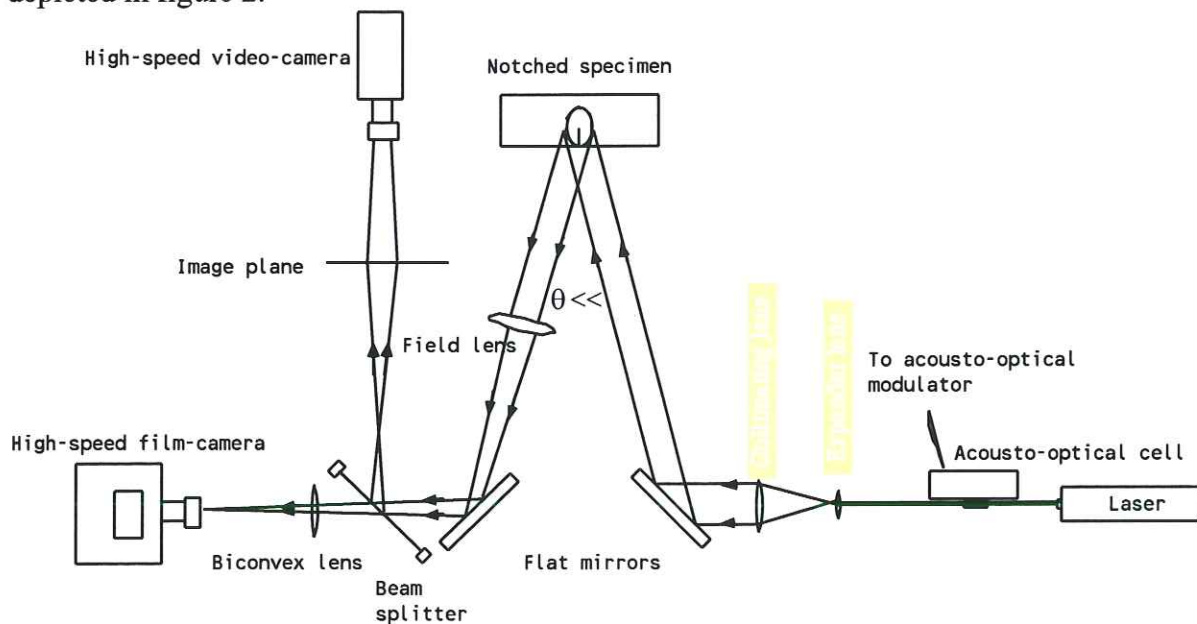


Fig. 2. Schematics of the optical set-up for caustics.

To enable capture of an extended field, the laser beam must be expanded. This is obtained by passing the beam through a bi-concave lens, to give a diverging beam. The light is then passed through a bi-convex lens, with a focal length function of the required light beam diameter. This expanded beam is deflected by a mirror, to illuminate the specimen.

After illuminating the specimen by the collimated light, this is directed to a lens which focusses an imaginary plane distant z_0 from behind the specimen plane, in order to visualize a caustic created during the process of testing.

The reflected beam is converged by a bi-convex lens of a large focal distance (3.5 m) and send by a mirror to the optical recording system. After this mirror a beam splitter is situated which will deflect the reflected light from the specimen onto the film-camera and an image screen from which a video-camera captures the event. By positioning a lens with respect to specimen-plane the shadow optical technique of caustics is utilized for monitoring the crack-tip caustics from which the stress-intensity factor as a function of time can be determined. One or both cameras must be focused on the image plane rather than the specimen in order to visualize the generated caustics.

The basics of the optical method of caustics can be found in Manogg [6] and Rosakis et al.[9]. A collimated laser beam is incident on a polished, optically flat specimen surface which includes a crack. The reflected light is imaged in a camera focussed on a virtual object plane at a fixed distance behind the specimen. When the specimen is loaded, its surface gets deformed. Due to this deformation, a light ray incident at a point of the specimen surface is mapped to a point on the virtual object plane. The resulting image contains a shadow-spot surrounded by a bright caustic. The transverse diameter of the caustic can be shown to be proportionally related to the out-of-plane displacement field.

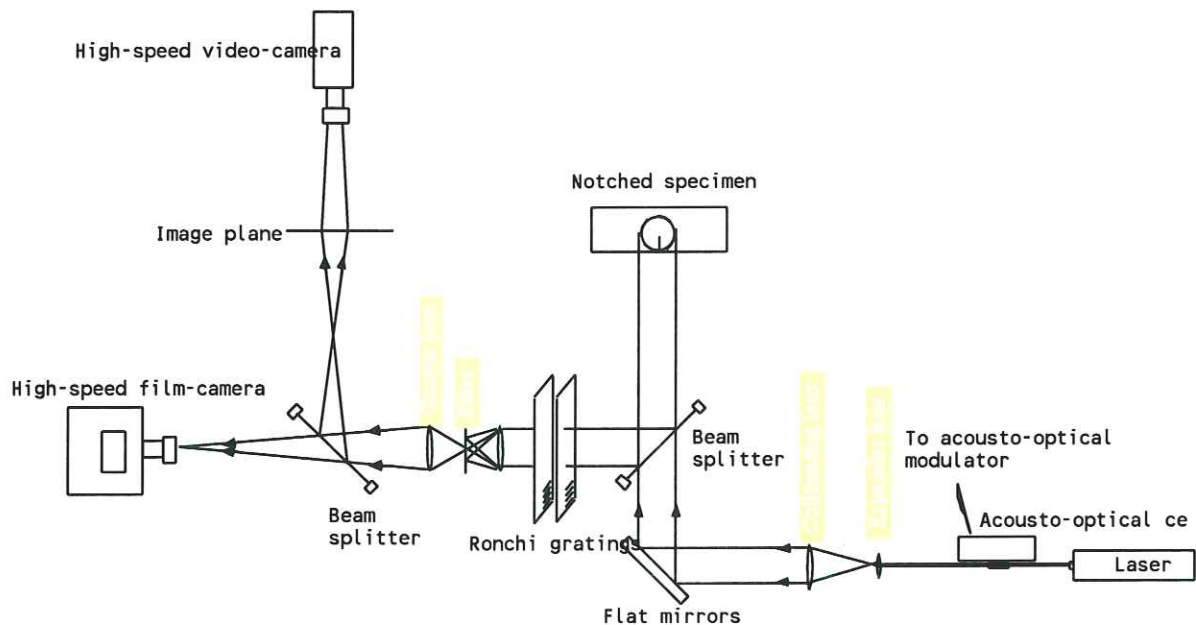


Fig. 3. Schematics of the optical set-up for Moire diffraction.

The optical scheme for the application of Moire diffraction is outlined in figure 3. In this arrangement the outgoing reflected light from the specimen is sent through two grating plates and a filter set. The processed light is later captured by the cameras.

The physical principle of the technique [4] is based on passing the reflected beam through two sinusoidal gratings parallel and separated a fixed distance. The diffracted rays from the first grating are again diffracted by the second one. By exiting from the second grating, the rays interfere with the others. A convergent lens located at a more advanced place refract rays of the same diffractive order into spots to generate a Fourier transform plane. By choosing diffraction order +1 or -1, the obtained beam contains information associated to the incident angle of the rays over the gratings, function of the reflecting angle suffered by the rays. This deformation is due to the out-of-plane strain experienced by the specimen

image surface. The image obtained is in form of a pattern of fringes. Order of fringes are related to reflexion angle on the specimen surface by the expression:

$$\frac{\partial u_z}{\partial x} = N \frac{p}{2\delta}$$

where N , p and δ stand for fringe order, grating pitch and separation gratings; x is the in-plane axis normal to grating orientation and u_z the out-of-plane displacement.

2.4. Basics Fundamentals and Hypothesis

In order to assess crack severity it is necessary to determine the critical parameters which govern the fracture process for a later quantification. Several parameters have customarily been handled. Some of them are directly observable: crack velocity, crack acceleration, deformation and have a direct physical interpretation. Others can be rated through indirect measurements, for example energy release and stresses. And even there are many of them which establish a comparative scenario with well known cases, i.e. stress intensity factors, stress/strain concentration factors.

Along this investigation two parameters have been used as quantifiable magnitudes: crack velocity and stress intensity factor (s.i.f). What follows collect a discussion of the assumed hypothesis and errors implied.

Related to crack velocity determination by optical measurement procedures the greatest error stems from precisising the exact position of crack tip during the dynamic process of fracture propagation. For instance, by using film cameras, at a rate of 200,000 f.p.s. (with an effective shutter time of 0.82 microseconds) the position of the tip of a crack propagating at a speed of 1000 m s^{-1} will be undetermined in a length of 0.82 millimeters. In addition to the above the film grain finess precludes an exact determination of tip position, factor enlarged by the fact that high sensitivity films are needed due to the scarcity of available light power at high dynamic testing. Moreover, data from crack tip position can not be collected in a continuous manner; framing film cameras impose time windows throught which the event can be recorded; outside them an interpolation technique has to be used in order to predict propagation. For a camera with a record speed of 1 million f.p.s, the interframe time is 1 microsecond (time enough for our example crack to travel 1 mm). This sort of undetermination should also be taking in mind as a source of error.

Referred to s.i.f., it is worth noting the following assumptions:

- A numerous amount of analytical solutions associated to two-dimensional problems are available nowadays: for different fracture specimen geometries, for distinct loadings and boundary conditions, for asymptotic and full-field approaches, and even for different materials (elastic, non-elastic, isotropic, orthotropic). However for three-dimensional geometries, even for the simplest ones -plate type-, there are not available analytical solutions which relate stress and strain on surface points on the vecinity of crack tip. The case gets worse for laminates with anisotropic/orthotropic material characteristics. This development lack forces that three-dimensional structures as plates are analyzed using the simplest available two-dimensional solutions (plane-stress or plane-strain asymptotic expressions for isotropic/orthotropic elastic materials), which are acceptable approximations for determining stress/strain fields far away from boundary

conditions but which are coarser approaches for evaluating stresses and deformations in the vicinity of crack tip where the geometry is distinctly three-dimensional.

- Taking into account the above considerations, along this investigation the following hypotheses have been assumed:
 - Two-dimensional asymptotic plane-stress solutions for a semi-infinity crack subjected to Mode I loading at infinity, in a homogeneous, elastic, isotropic, small deformation material is considered.
 - The existence of a region of K_I dominance is considered. Said a region surrounding the crack, away from the tip a distance sufficient to neglect three-dimensional effects and bounded by a contour over which the asymptotic analysis is not longer valid, where the two-dimensional expressions are valid.
 - The lack of material homogeneity due to fibres along the in-plane geometry, as due to laminae piling-up and orientation in the cross-sectional geometry is also neglected. This means that each laminate composite plate coupon is considered as a homogeneous isotropic geometry in which the two previous hypotheses are applicable.
- Taking into account the above hypotheses and the approximation of the two-dimensional solutions by the first order terms, the transverse diameter $D(t)$ of the caustic and dynamic s.i.f. K_I are related through the expression:

$$K_I = \frac{2E\sqrt{2\pi}}{3\nu\alpha_1 h z_0 F(\nu)} \left(\frac{D(t)}{3.17} \right)^{2.5}$$

where h is the plate specimen thickness, E and ν are Young's modulus and Poisson's ratio of the material, ν the instantaneous crack speed, α_1 the longitudinal wave speed, z_0 the distance between the specimen and focal plane of the camera, and $F(\nu)$ a function of longitudinal and shear wave speeds [8].

In case the approximation of the two-dimensional plane-stress asymptotic solutions takes into account three terms, the diameter of the caustic and s.i.f. are related in a more complex way. Derivation of s.i.f. precises a previous knowledge of the exact position of tip, during crack propagation. This more accurate theoretical technique, although very elegant, does not eventually improve experimental results, as the equations to be solved, in order to obtain values for the s.i.f., are stiff and very sensitive to experimental data errors.

3. EXPERIMENTAL RESULTS

3.1. Specimens

The specimens tested are plate-type coupons of different sizes, with length varying between 170 and 310 mm, width in the range 55-120 mm, and thickness in the interval 12 to 60mm. Specimens geometry is shown in figure 4.

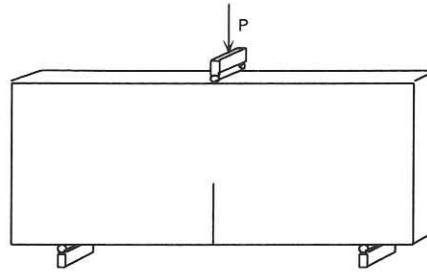


Fig. 4. Specimen geometry.

The material is a graphite-epoxy laminate (woven or tape), used for aeronautical applications (Douglas, Airbus, Boeing). The material properties, for different specimens, are in the following range. Density ρ : 1,502 - 1,686 Kg m⁻³, Poisson ratio ν : 0.3, Young's modulus E : 138,000 MPa.

Woven specimens are made by piling up, with identical orientation, laminae of epoxy resin impregnated graphite woven. Tape specimens are obtained by laying up several tape laminae with different orientations.

In order to obtain a high reflective surface in the coupons, one of the surfaces suffers a treatment divided in several phases:

- Firstly the surface is sandpapered in successive steps up to a finess of 9 μm .
- Secondly, a coating of epoxy resin, 10 μm thick, is laid on top of the surface (the resin is poored on a glass flat plate over which the specimen is pressed).
- Thirdly, the resin coating is again polished and latter covered with a new resin deposition.
- Finally, an aluminium vapour deposition leaves the surface mirror-liked.

Specimens are statically tested in order to obtain the critical s.i.f., K_{I1} , in function of applied load and crack length at the fracture instant. Two-dimensional analytical expression for isotropic and homogeneous materials. This K_{I1} varies between 38.7 MPam^{1/2}, for woven Z-19.749, and 44.6 MPam^{1/2}, for woven Z-19.738, and in the range 40-70 MPam^{1/2} for tape Z-19.785 .

3.2. Results

The specimens were tested at impactor velocities in the range 20-30 ms⁻¹, and its reflective surface recorded by the optical techniques formerly described.

The focal plane is located at a distance in the range 1,450 to 3,595 mm in the technique of caotics. Care has been taken for not collecting data from inside the three-dimensional zone, region surrounding crack tip inside a circle of radius 40% of specimen thickness ($r < 0.4 t$).

Figures 5a and 5b depict dynamic s.i.f. versus time for woven material Z-19.749 and tape material Z-19.772.

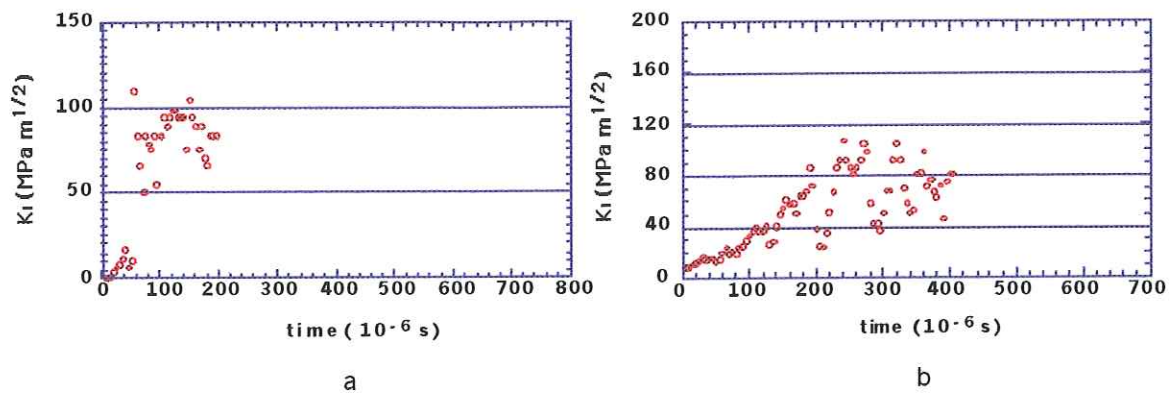


Fig. 5. Stress intensity factor versus time for woven (a) and tape (b) laminated plates.

A recording of crack propagation provides a sequence of photograms, as shown in figures 6 and 8 for woven and tape materials, respectively.

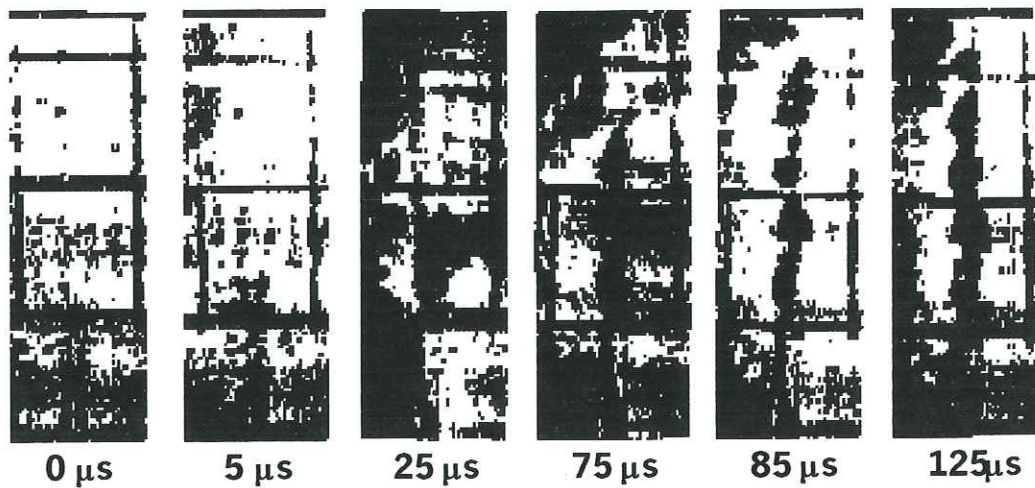


Fig. 6. A propagating crack in woven carbon fibre-epoxy laminate specimen.

In figures 9a and 9b, crack length versus time yield an average crack speed of 216 ms^{-1} for woven and 100 ms^{-1} for tape with minimum and maximum picks of 19 and 696 ms^{-1} for woven, respectively and 27 and 386 ms^{-1} for tape. Two tested specimens are depicted in figure 7.

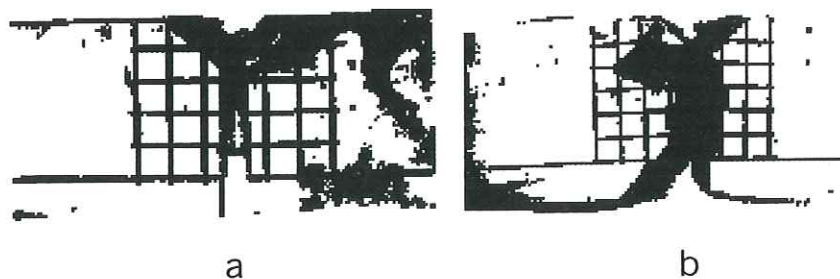


Fig. 7. Tested specimens a) woven b) tape.

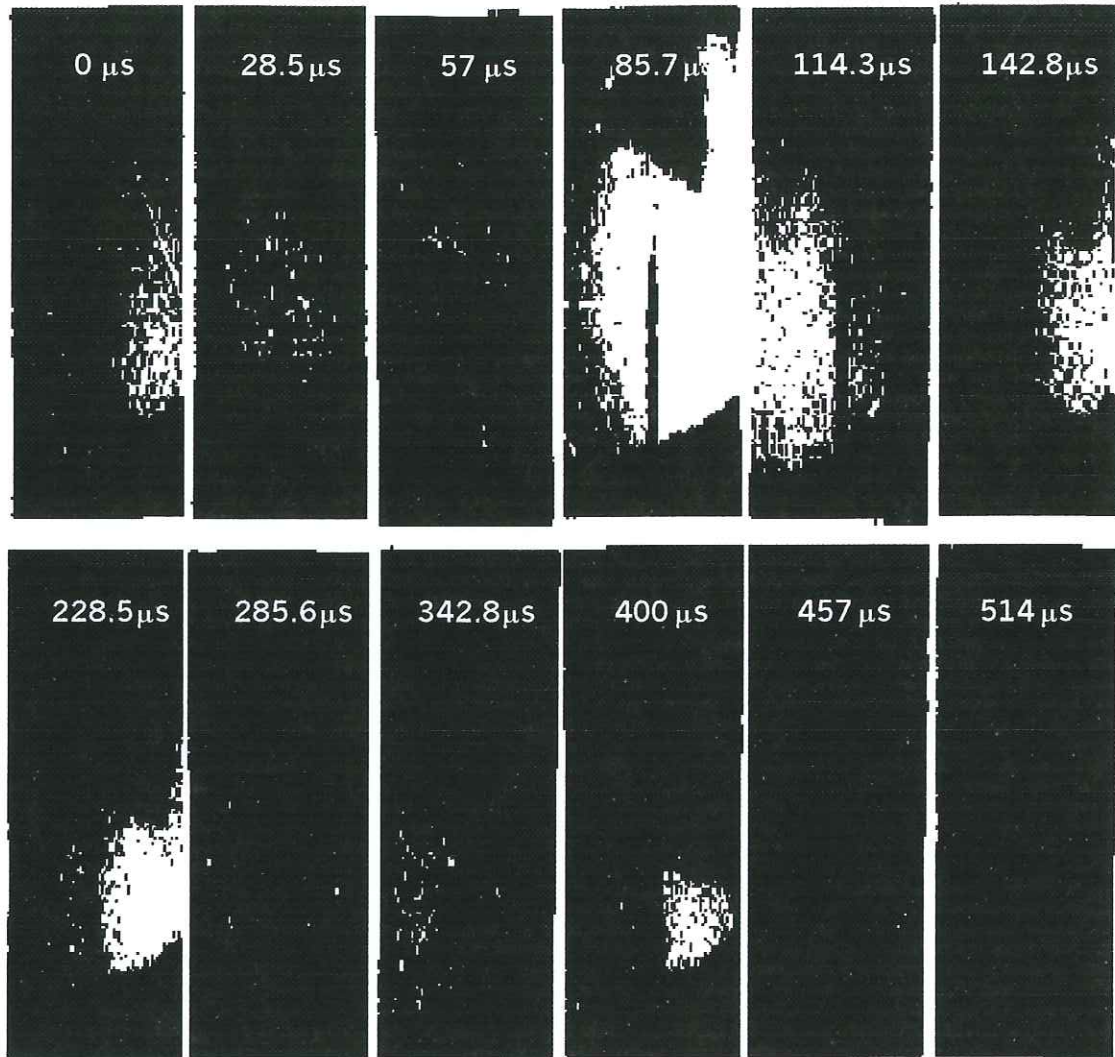


Fig. 8. A propagating crack in tape carbon fibre-epoxy laminate specimen.

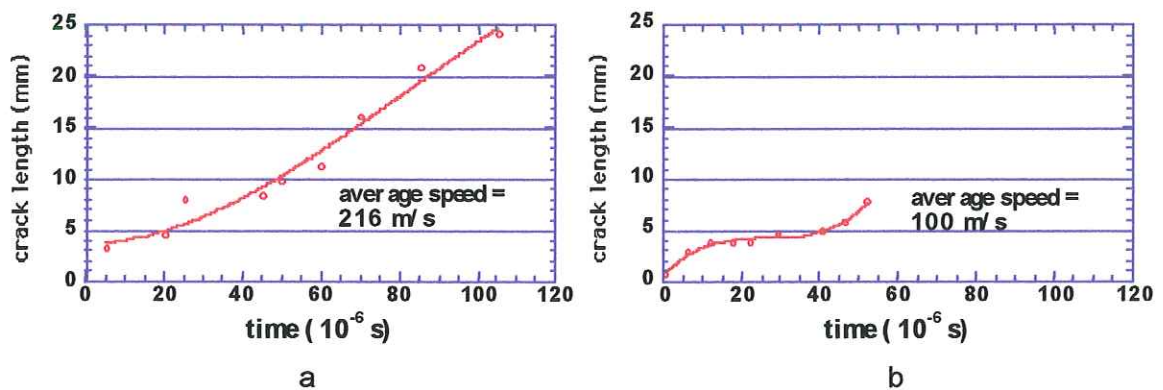


Fig. 9. Crack growth versus time in woven (a) and tape (b) carbon fibre-epoxy laminates.

A sequence of pictures showing caustic and Moire diffraction fringes formation for tape material is depicted in figures 10 and 11 respectively, where only a selection of photograms are shown. The recording rate is 200,000 fps.

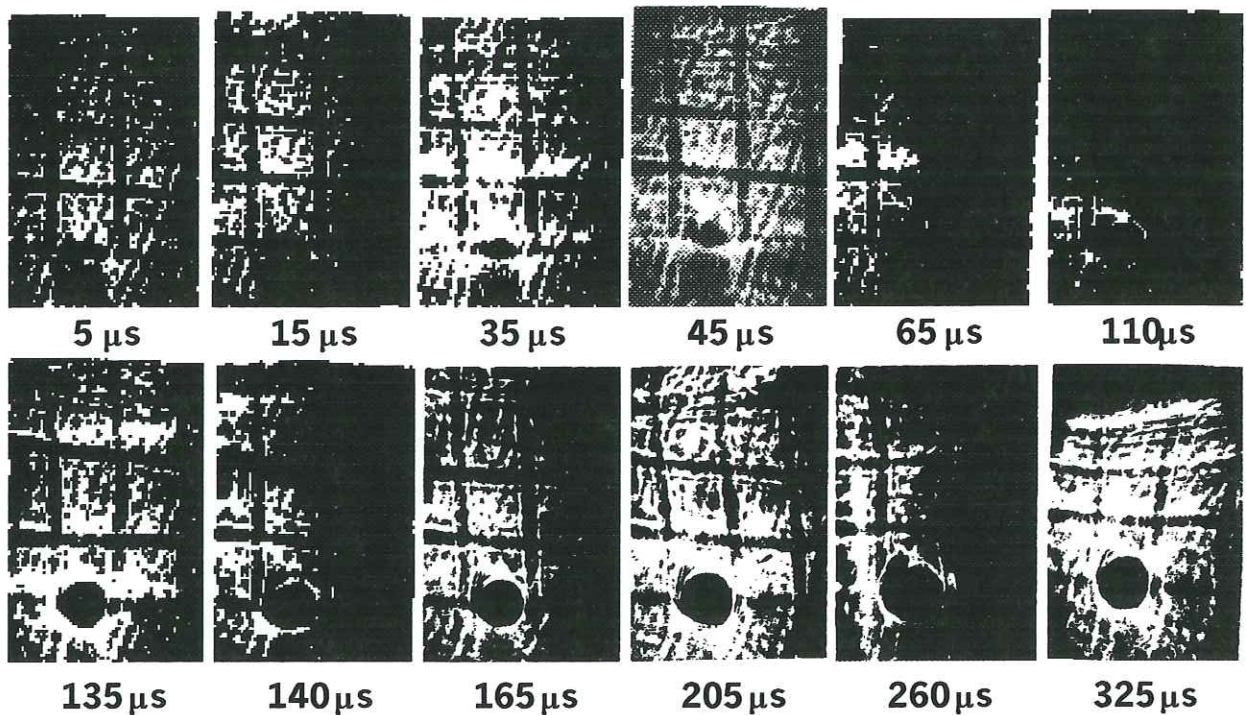


Fig. 10. Sequence of caustics formation for tape carbon fibre-epoxy laminate.

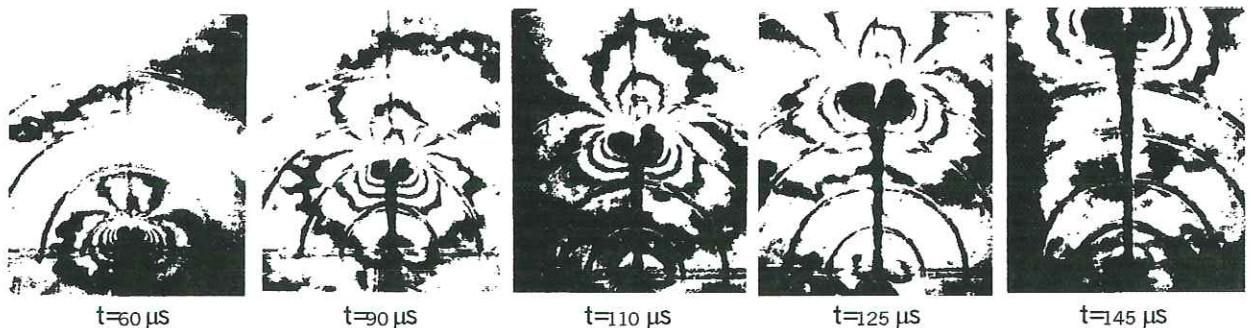


Fig. 11. Sequence of Moire diffraction fringes for tape carbon fibre-epoxy laminate.

4. CONCLUSIONS

Through-cracks in graphite-epoxy laminated propagate at very different speeds depending on the laminae structure, the average speed is 100 ms^{-1} and 200 ms^{-1} for tape and woven laminates, respectively. During the propagation event picks of higher speed take place, but the lower values of crack velocity indicate a non-severe mechanism and an easy arrest. Under impact loadings there is not a clear K_I -dominant region. This result draws attention into the validity of the stress intensity factor as an absolute magnitude to evaluate crack severity in these materials.

As a practical technological application, the results show that the use of through-cracks in these materials might not be the best mechanism to originate an unstable fracture in the cases a material separation is sought.

5. ACKNOWLEDGMENTS

The support of Ministry of Science from Spain (CICYT grant MAT95-0569) and Ramon Areces Foundation are thankfully acknowledged. Contribution from SACESA for providing the material for testing is fully regarded. This contribution includes part of the work performed with some of my collaborators at Sevilla. These include Professors P. Pintado, J.M Castillo, postdoctoral fellow Dr. G. Hognestad and my graduate students L. Andrades, C. Pedraza and J.I. Sanabria.

6. REFERENCES

- [1] Andrades, L. Evaluacion optica de la tenacidad a la fractura en comportamiento dinamico ante cargas de impacto en PMMA y laminados de grafito-epoxy. Doctoral dissertation, University of Sevilla, Spain, 1999.
- [2] Benitez, F.G.; Andrades, L. In-Plane Impact Loading of Composites: Optical Evaluation and Crack Severity Assesment for Graphite-Epoxy. *J. de Physique IV*, III-C3, 169-174, 1997.
- [3] Chun-Gon Kim; Eui-Jin Jun. Impact Resistance of Composite Laminated Sandwich Plates. *Journal of Composite Materials*, Vol. 26, No. 15, pp 2247-2261, 1992.
- [4] Cloud, G. *Optical Methods of Engineering Analysis*. Cambridge University Press, 1995.
- [5] Hyung Yun Choi; Fu-Kuo Chang. A Model for Predicting Damage in Graphite/Epoxy Laminated Composites Resulting from Low-Velocity Point Impact. *Journal of Composite Materials*, Vol. 26, No. 14, pp 2134-2169, 1992.
- [6] Manogg, P. *Anwendung der Schattenoptik zur Untersuchung des Zerreißvorgangs von Platten*. Doctoral dissertation, Freiburg, West Germany, 1964.
- [7] Pintado, P.; Pedraza, C.; Castillo, J.M.; Benitez, F.G. Dynamic Response of Graphite-Epoxy Composite Laminates Under Compression. *ICCM-9 International Conference on Composite Materials. Composites Behaviour* (Ed. A. Miravete), Woodhead Publishing Limited, U.K. pp.438-444. 1993.
- [8] Rosakis, A.J. Two optical techniques sensitive to gradients of optical path difference: The method of caustics and the coherent gradient sensor (CGS). *Experimental Techniques in Fracture*, Ed. J.S. Epstein. VCH. ISBN: 1-56081-641-4(V3), 1993.
- [9] Rosakis, A.J.; Zehnder, A.T. On the method of caustics: An exact analysis based on geometrical optics. *Journal of Elasticity*, 15, 4, 347-367, 1985.
- [10] Strait, L. H.; Karasek, M. L.; Amateau, M. F. Effects of Stacking Sequence on the Impact Resistance of Carbon Fiber Reinforced Thermoplastics Toughened Epoxy Laminates. *Journal of Composite Materials*, Vol. 26, No. 12, pp 1725-1740, 1992.
- [11] Wang, H.; Vu-Khanh, T. Damage Extension in Carbon Fiber/PEEK Crossply Laminates under Low Velocity Impact. *Journal of Composite Materials*, Vol. 28, No. 8, pp 685-707, 1994.

Compression after impact of low velocity impacted composite panels

L. Reis, A. Silva and M. de Freitas

Instituto Superior Técnico, Dep. Eng.^a Mecânica, Av. Rovisco Pais
1049-001 Lisboa, Portugal

ABSTRACT

Low velocity impact loading in aircraft composite panels is a matter of concern and can be caused either due to maintenance accidents with tools or in flight impacts with debris. The consequences of impact loading in composite panels are matrix cracking, inter laminar failure and eventually fiber breakage for higher impact energies. Even when no visible impact damage is observed at the surface on the point of impact, matrix cracking and inter laminar failure can occur, and the carrying load of the composite laminates is considerably reduced. The greatest reduction in loading is observed in compression due to laminae buckling in the delaminated areas.

The objective of this study is to determine the limit loading capacity and the damage growth mechanisms of impacted composite laminates when subjected to compression after impact loading. For this purpose a series of impact and compression after impact tests are carried out on composite laminates made of carbon fiber reinforced epoxy resin matrix with stacking sequences representative of four different elastic behaviors. Finite element analyses are computed in order to analyze the delamination behavior of the different panels when subjected to impact loading using two different failure criteria.

INTRODUCTION

The design and maintenance procedures of modern aircraft is changing with the establishment of new technologies, and earlier concepts as safe life and fail safe are being up dated with modern ones such as damage tolerant design. There has been a continuous increase of components that use composite panels in aeronautic and aerospace structures due to their high strength/weight ratio. The presence of fibers in the plane increase the strength of the laminates under membrane or bending loads but the stiffness and the strength in the through the thickness direction of laminated composite panels, is poor since no fibers are present in that direction. The out-of-plane loading can be caused by impact either by low-velocity impact or ballistic impact. Low velocity impact loading in aircraft composite panels is present either due to maintenance accidents with tools or in flight impacts with debris. The low-velocity impact of CFRP laminates creates damage that may involve indentation, matrix cracking, fiber matrix debonding, delamination, inter laminar failure and eventually fiber breakage for higher impact energies. Low-velocity impact is considered

potentially dangerous mainly because the damage might be left undetected. In many situations [1-3], the level of impact at which visible damage is formed is much higher than the level at which substantial loss of residual properties occurs. Visible damage occurs if an impact is above a threshold impact energy that depends on the laminate stiffness [4,5]. Even when no visible impact damage is observed at the surface of impact (energies below Barely Visible Impact Damage, BVID), matrix cracking and inter laminar failure can occur, and the carrying load of the composite laminates is considerably reduced. The greatest reduction in after impact loading is observed in compression due to laminae buckling in the delaminated areas. The laminate residual strength and modulus after delimitation depend on the stacking sequence and the location of the delimitation in the laminate. Considerable research [6-10], has therefore been devoted to analyzing the impact properties and post-impact compression behavior with a view of improving impact damage tolerance.

This presentation has two objectives: first, to explain the techniques used for detection, measurement and numerical calculations of the delaminated areas in composite panels due to low velocity impact loading; second, the tests that are currently used to determine the limit loading capacity of impacted composite laminates when subjected to compression after impact loading. For this purpose a series of tests were carried out on composite laminates made of carbon fiber reinforced epoxy resin matrix. Four stacking sequences representative of four different bending and compression behavior and an instrumented falling weight impact machine were used. A discussion and some concluding remarks are presented.

EXPERIMENTAL PROCEDURE

Materials

Composite panels were made from two materials: carbon fibers IM7 with the epoxy resin 977-2 and T800 carbon fibers in a 5245C epoxy resin respectively of nominal thickness 0.135 mm and 0.190 mm for 60% V_p , and four stacking sequences of 24 layers were used:

lay-up B : [45₃/0₃/-45₃/90₃]S

lay-up C : [45/0/-45/90/45₂/0₂/-45₂/90₂]S

lay-up D : [45₄/-45₄/0₃/90]S

lay-up E : [45₃/-45₃/0₅/90]S

The elastic properties of the individual laminae and global properties for each panel were obtained by identification of the material properties using experimental vibration data [11] and can be found in Reis et al. [12]. Lay-up B and C correspond to a quasi-isotropic stacking sequence; in lay-up D and E different global elastic properties are obtained for each direction.

Specimens with dimensions of 150x100 mm were cut from the panels; for each lay-up, five specimens with the 0° direction aligned with the 100 mm width (lay-up B, C, D and E) and three

specimens with the 0° direction aligned with the 150 mm length (lay-up B*, C*, D* and E*) were obtained.

Impact testing

A wide range of impact energies was chosen in order to obtain different delamination areas. An instrumented falling weight impact machine was used where the different nominal impact energies were obtained through discrete masses of 2 to 10 Kg and a variable height up to 2 m.

The instrumentation associated with the impact machine measures the force during impact, using a force transducer just above the impactor indenter. The system also provides for the measurement of the velocity at the moment of impact. The velocity during impact is calculated by integrating acceleration over time, where the acceleration is given by the force felt by the drop mass, divided by its mass. The calculated velocity is then used to derive the displacement of the impactor during impact (and consequently the deflection of the specimen) using further integration. The energy is calculated by integrating force over distance. With this measurement and calculation procedure, one obtains not only the impact energy but also the absorbed energy through the energy/time curve.

The impactor used was a hemi-spherical steel one with 16 mm diameter and the specimen was clamped in a standard impact testing fixture with a window of 125x75 mm.

Delamination area

A C-scan NDI ultrasonic technology with a pulse-echo and an immersion scanning method, Physical Acoustics, was used, with the following C-scan data:

- Scan frequency: - 5 MHz
- Scan speed (X axis): - 30 mm/sec
- Index axis : - Y axis
- Scan interval index: - 0.05 mm

There are two kinds of data processing in pulse-echo C-scanning: echo amplitude (.AMP) view and time of flight (.TOF) view. The latter data can be converted into a delamination depth view through the transverse sound velocity in CFRP laminates. The TOF files obtained together with an image processing software allowed the determination of the delaminated area for each specimen and energy level. An example of the images obtained by C-scan procedure and .TOF data are shown in figure 1a, showing the damage after impact of one of the specimens with lay-up B impacted with 12.1 Joule. It shows that for a quasi-isotropic stacking sequence and a low level impact energy, a small and symmetrical delaminated area is obtained.

Compression After Impact

The compression after impact tests of the specimens was conducted on a universal testing machine. The tests were conducted in displacement control with a velocity of 0.5 mm/min. The testing fixture described in the Boeing/Airbus testing procedure was used. In this fixture and to prevent global buckling during compression, the specimens were clamped at both ends and simply supported at the side edges. In order to establish the buckling behavior of the delaminated area during testing and final failure, three LVDT were attached to the specimen: one at the center of the impact zone, the second one at the opposite side and the third one on the testing fixture to monitor the vertical displacement of the specimen during the test. A schematic view of the instrumented compression after impact (CAI) testing fixture with a specimen and the three LVDT in testing position, can be found in [12,13]. Concerning the damage growth during compression, it corresponds to a typical buckling failure where the damage growth is obtained suddenly leading to the complete failure of the specimen, shown in figure 1b. As can be seen on the C-scan images of figure 1a and 1b, the delamination growth is obtained in the lateral direction, perpendicular to the applied compression load. The delamination growth observed in the vertical direction was much lower than on the lateral direction

RESULTS AND DISCUSSION

Failure analysis

In order to analyze the different behavior of the four laminates, a finite element analysis was carried out using a commercial finite element code COSMOS/M.

The analysis was performed modeling the specimen with a quadrilateral composite shell element with 4 nodes and six degrees of freedom per node (three rotations and three translations). A static analysis was performed using the maximum force measured during the impact tests on the drop weight testing machine. This can be done because the velocity of impact is very low, and no significant dynamic effects are present. Boundary conditions were laid as in the experimental setup and a stress analysis was performed. The finite element model had 9562 degrees of freedom, corresponding to 1536 elements and 1617 nodes.

Two failure criteria were used: first the classical Tsai-Hill failure criteria and second a criteria where the individual failure of matrix cracking, fiber breaking and delamination were determined. All materials and lay-ups were computed numerically and comparison was then made with the images of C-scan. The numerical results obtained using only a plot of transverse stress (the in-plane stress in the direction perpendicular to the fibers), for the bottom layer, material T800, are presented on figure 2 and characterize matrix cracking. A reasonable good correlation is obtained

between Tsai-Hill criterion and matrix cracking, which identifies clearly the failure mode during impact.

Several specimens were tested at different impact energy levels ranging from 4 to about 80 Joule. These energy levels allowed performing increasing damaged areas in the specimens up to perforation. After impact the delamination area of the specimens and the permanent indentation depth of the impact point were measured. The latter one is the procedure prescribed in AITM 1.0010 to establish the visibility of the surface defect. Figure 3 shows the indentation depth obtained for the range of impact energies used. Despite the scatter of the results, a direct correlation exists between the impact energy and the surface indentation depth. The AITM considers as BVID energy level (Barely Visible Impact Damage), the energy necessary to put a permanent indentation depth of 0.3 mm, and for these lay-ups we have obtained approximately 20 Joule of impact energy.

The shape of the delamination was identified and the delaminated areas measured. Figure 4 shows the delaminated area as a function of the absorbed energy determined as described before. Again a direct correlation exists between the two quantities, but for perforation energy levels the delaminated areas are smaller than expected. There was no practical influence of the stacking sequences on the indentation depth and delaminated areas, since the influence of the impact energy is the most leading factor.

It has been remarked that the compression residual strength of delaminated composite laminates is highly affected due to the buckling mechanisms of the delaminated lamina [12]. As four different stacking sequences were tested in two testing directions, the results may be analyzed either in load (stress) or in strain. Comparing the compressive residual strength as a function of the delaminated area respectively for the B, C, D and E and B*, C*, D* and E* stacking sequences it is expected that the E stacking sequence presents the smallest residual compressive strength while the E* stacking sequence presents the greatest compressive residual strength. This is due to the presence of the 0° and 90° plies, corresponding to higher elastic modulus in those directions. For the B, C and B*, C* stacking sequences since they represent quasi-isotropic stacking sequences, the direction of loading does not affect the compressive residual strength.

These results can be analyzed as a function of strain to failure, based on the elastic properties of each stacking sequence. The compressive residual load is then transformed in stresses and in strains and through the delaminated area related with the absorbed energy. The results presented in strains show a smaller scatter and a uniformity of the strain to failure as a function of the delaminated area and of the absorbed energy. This is shown in Figure 5 together with a linear regression of the points. It is clear that the composite panels with different elastic modulus present similar strain to failure for the wide range of absorbed energies.

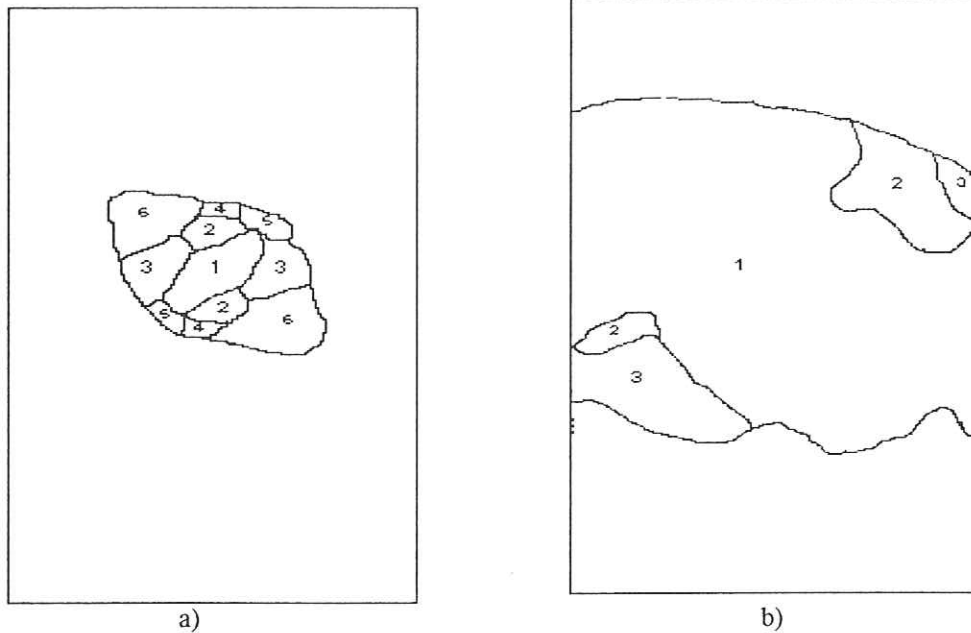
CONCLUSIONS

Low velocity impact and compression after impact tests of laminate composite panels were carried out and allow the following conclusions:

- the delaminated area is a function of the impact energy and relatively independent of the stacking sequences used in this study;
- unstable damage growth, obtained by compression after impact is due to a buckling mechanism in the delaminated area;
- the residual strength is influenced by the delaminated;
- the residual strength when considered in terms of failure load (failure stress for the same thickness) depends of the stacking sequence, but the strain to failure is not affected by the stacking sequence used.

REFERENCES

1. Sjoblom, P.O., Hartness, J.T. and Cordell, T.M., "On Low-Velocity Impact Testing of Composite Materials," *J. of Composite Materials*, Vol. 22, pp. 30-52, 1988.
2. Wu, H.T. and Springer, G.S., "Measurements of Matrix Cracking and Delamination Caused by Impact on Composite Plates," *J. of Composite Materials*, Vol. 22, pp. 518-532, 1988.
3. Delfone, D., Poursartip, A., Coxon, B.R., and Dost, E.F., "Non-Penetrating Impact Behavior of CFRP at Low and Intermediate Velocities," *Composites Materials: Fatigue and Fracture (Fifth Volume)*, ASTM STP 1230, R.H. Martin, Ed., American Society for Testing and Materials, Philadelphia, pp. 333-350, 1995.
4. Found, M.S., Howard, I.C., "Single and Multiple Impact Behaviour of a CFRP Laminate," *Composite Structures*, Vol. 32, pp. 159-163, 1995.
5. Liu, S., Kutlu, Z. and Chang, F.K., "Matrix Cracking and Delamination in Laminated Polymeric Composites Resulting from Transversely Concentrated Loadings," *Proceedings of the 1st International Conferences on Deformation and Fracture of Composites*, pp. 30/1-30/7, Manchester, England, March 25-27, 1991.
6. Madan, R.C., "Influence of Low-Velocity Impact on Composite Structures," *Composites Materials: Fatigue and Fracture (Third Volume)*, ASTM STP 1110, T.K. O'Brien, Ed., American Society for Testing and Materials, Philadelphia, pp. 457-475, 1991.
7. Dost, E.F., Ilcewicz, L.B. and Coxon, B.R., "Effects of Stacking Sequence on Impact Damage Resistance and Residual Strength for Quasi-Isotropic Laminates," *Composites Materials: Fatigue and Fracture (Third Volume)*, ASTM STP 1110, T.K. O'Brien, Ed., American Society for Testing and Materials, Philadelphia, pp. 476-500, 1991.
8. Ishikawa, T., Sugimoto, S., Matsushima, M., Hayashi, Y., "Some Experimental Findings in Compression-After-Impact (CAI) Tests of CF/PEEK (APC-2) and Conventional CF/EPOXY Flat Plates," in *Composites Science and Technology*, Vol. 55, pp. 349-363, 1995.
9. Kinsey, A., Saunders, D. E. J. & Soutis, C., "Post-impact compressive behaviour of low temperature curing woven CFRP laminates", *Composites*, 26, pp. 661-667, 1995.
10. C. Soutis & P.T. Curtis, "Prediction of the Post-Impact Compressive Strength of CFRP Laminated Composites," in *Composite Science and Technology*, Vol. 56, pp. 677-684, 1995.
11. Araújo, A. L., Soares, C.M.M., Freitas, M.J.M., "Characterization of material parameters of composite plate specimens using optimization and experimental vibrational data," *Composites: Part B*, 27B, pp. 185-191, 1996.
12. Reis, L. and Freitas, M., "Damage growth analysis of low velocity impacted composite panels", *Composite Structures*, Vol. 39, 1-4, (1997), pp. 509-516.
13. Reis, L. and Freitas, M., "Failure mechanisms on composite specimens subjected to compression after impact", *Composite Structures*, Vol. 42, No 4 (1998), pp 365-374.



a) b)
Fig 1 – C-scan images of T800-5245C –lay-up D , respectively
 a) after impact and b) after compression after impact

Legend for lay –up D:

- | | | |
|------------------------|-----------------------|-------------------------|
| 1- interface -45°/+45° | 2 - interface +45°/0° | 3 - interface 0°/90° |
| 4 - interface 90°/0° | 5 - interface 0°/+45° | 6 - interface +45°/-45° |

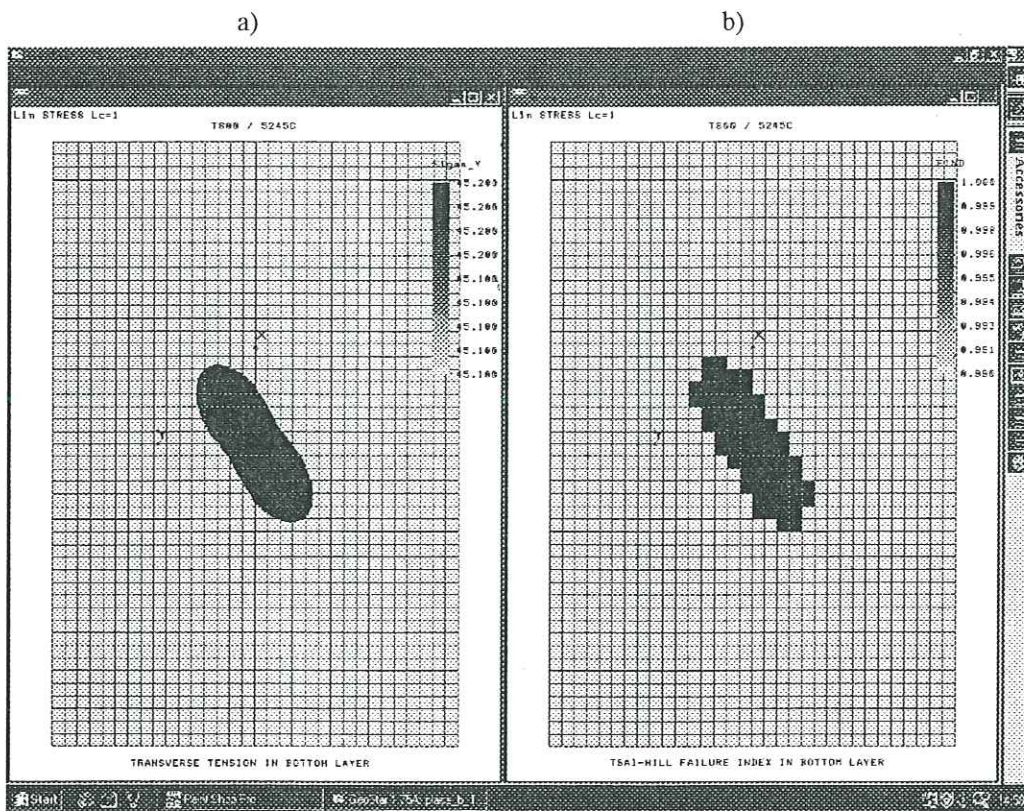


Fig 2 – FEM analysis of T800-5245C, lay-up B, bottom layer

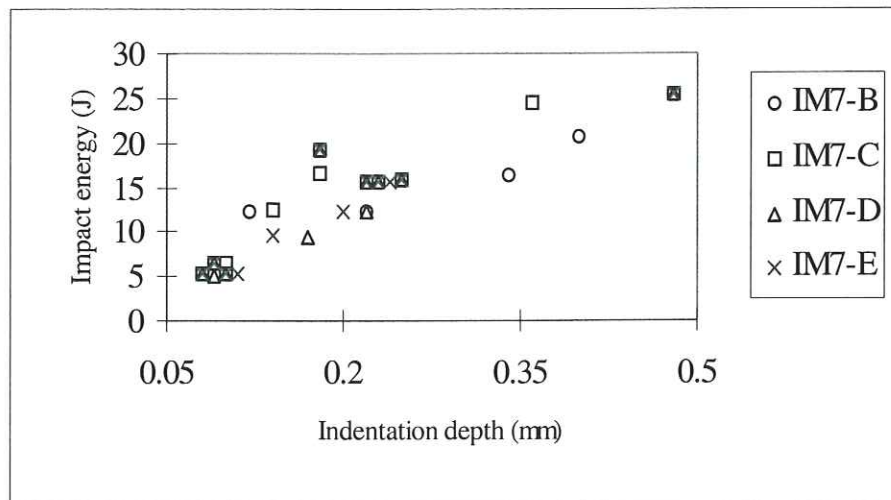


Fig 3 – Indentation depth for material IM7/977-2

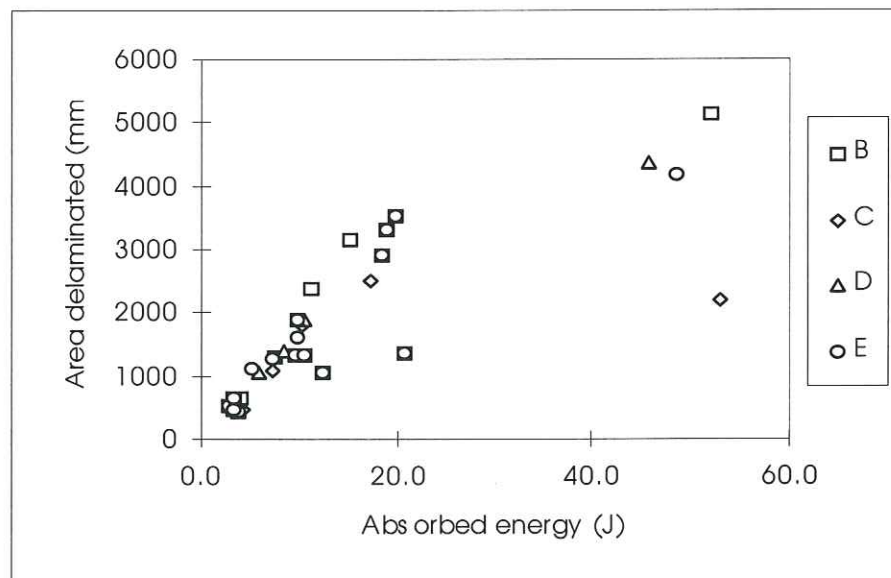


Fig 4 – Delaminated area for material IM7/977-2

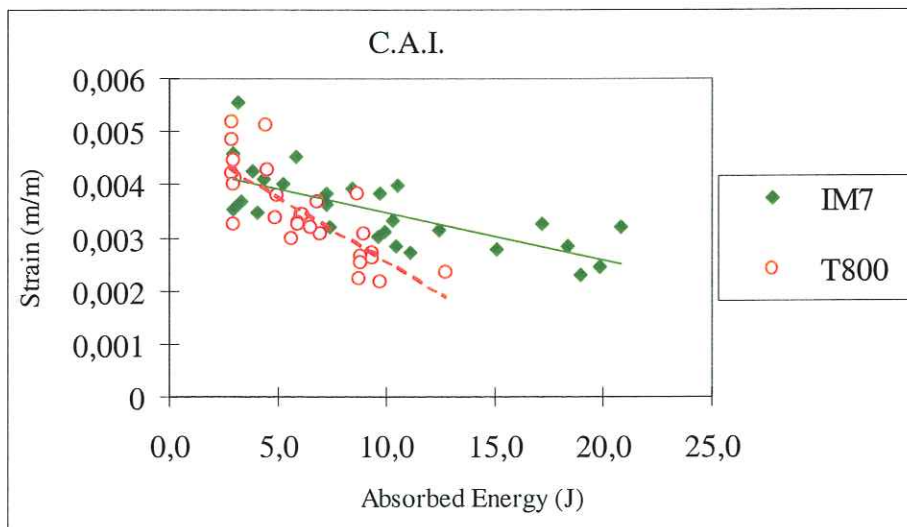


Figure 5 – Residual strength for all materials and stacking sequences

Study of glass-fibre reinforced plastic for structures protected by explosive reactive armour

Sébastien Ginestet, Serge Jonneaux, François Decobert, Hubert Orsini

DGA/CTA, 16 bis avenue Prieur de la Côte d'Or, 94114 Arcueil Cedex, France

Summary :

In the race for weight reduction of weapon systems, glass-fibre reinforced plastic (GRP) materials play a preponderant role. Already present on navy ships and on aircraft, they could be efficiently use for the design of land armoured vehicles, considering the advantages they could offer with their specific properties. However, the damage and the behaviour under shock of GRP must be take into consideration. We study here the behaviour of a GRP structure protected by an explosive reactive armour (ERA). This protection is efficient against shape charges but it ejects a metallic plate at high velocity towards the structure it protects.

The first experimental results showed a large damage in the GRP plate due to the action of the reactive modulus. In order to obtain the maximum of data during the experiments, an adapted instrumentation is used : flash X ray, cracking gauges, position sensors. To reduce the damage of the GRP, we introduce attenuating materials or concepts in front of the structure. A numerical approach is carried out with the code *ABAQUS/Explicit* in order to identify the main parameters before the experiments.

1 - INTRODUCTION

The defence concept changes with the new geopolitical situation. The air transport of military equipment, and in particularly the armoured vehicles, becomes a crucial characteristic. To optimise this component, we are interested in the glass fibre reinforced plastic (GRP) materials. Table I presents a comparison of the specific strengths of GRP and other metallic materials [1][2].

Explosive reactive armours (ERA) are very efficient against shape charges. They consist of a steel/explosive/steel sandwich which detonates when hit by the shape charge jet and disturbs part of this jet. However, its functioning also implies the projection of the steel back plate at high velocity towards the protected structure. The aim of this study is thus to assess the damage induced by an ERA to a GRP structure, and to determine the main parameters. Then, another objective is also to reduce the damage, for example by adding attenuating materials on the GRP structure or introducing adhesive layers within the GRP.

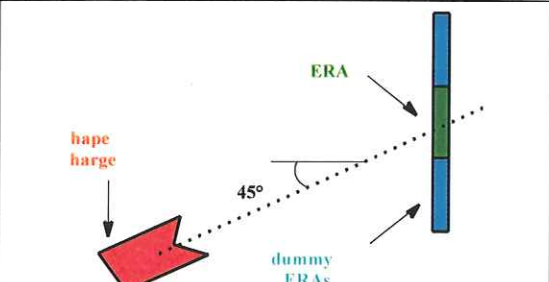
<i>Table I : Comparison of the specific strengths</i>			
Materials	Armour steel	Aluminium alloy	GRP (70 % fibre)
Yield stress (Mpa)	1200	450	400
Density	7.8	2.7	2.1
Specific strength (Mpa)	154	166	190

2 - EVALUATION OF ERA ON GRP

2.1 - Experimental configuration

The experimental configuration is identical for all the experiments. It is presented in Table II, along with the value of the back face deformation (H), evaluated by flash X ray at 100 μ s and 200 μ s after the shape charge jet hit the ERA.

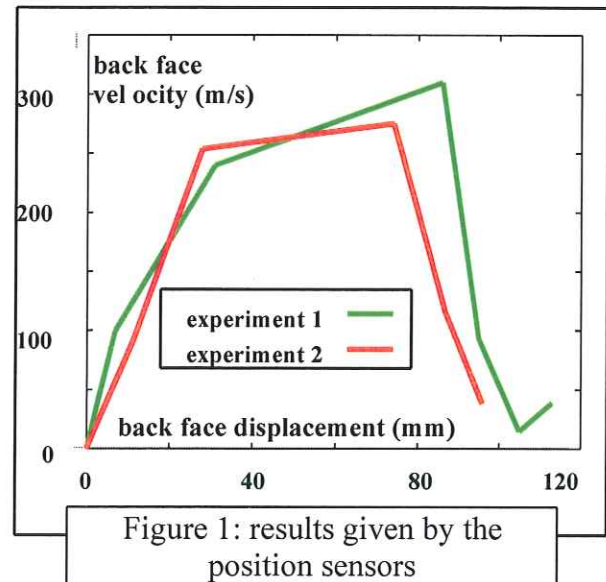
Table II : experimental configuration and results		
Experiment n°	1	2
H at t=100 μ s (mm)	8	7
H at t=200 μ s (mm)	34	31



2.2 - Instrumentation

During the interaction between the GRP plate and the ERA back plate, position sensors provide information on the displacement of the back face of the GRP plate about level with the impact area.

Two kinds of displacement are observed : a global displacement of the whole GRP plate and the expansion of a localised dome under the impact area. Figure 1 presents the back face velocity as a function of the back face displacement. The strong variation observed allows to separate these two displacements. The height of the back face deformation can thus reach an estimated 80 mm.



2.3 - Post-mortem analysis

The configuration ERA + GRP is effective against the considered shape charge : the GRP plate is not perforated. The part of the shape charge jet not disturbed by the ERA is consumed by the GRP. On the other hand, the composite material is strongly delaminated on all its surface. We can also see on the front face of the GRP plate an important stamp caused by the impact. Two different areas of delamination are visible (figure 2).

- *Area A* : during the impact shear stresses appear in the GRP around the extremity of the impact. This shear stresses induce the delamination in the front face. It is present on the right of area A because on the left, the material is loaded in compression. This damage is amplified by the penetration of the shape charge jet.
- *Area B* : during the impact, a compression wave spreads out along the composite thickness. After reflection on the back face, this wave becomes a tensile wave which

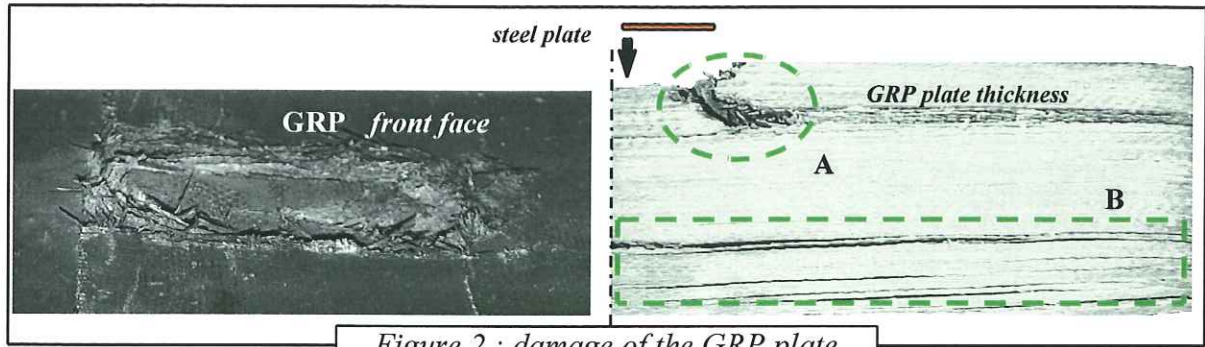


Figure 2 : damage of the GRP plate

delaminates the interfaces. Some interfaces are also delaminated under the effect of the shape charge jet.

2.4 - Numerical simulation

We perform a simulation of the impact between the two plates with the finite element code *ABAQUS/Explicit*. We use 10000 tri-dimensional elements and in a first time we do not introduce cracking model. By symmetrical considerations, we simulate only one quarter of the problem.

We observe, during the calculation, some shear stresses of about 200 MPa and tensile stresses of about 1 GPa in the thickness (figure 3). This fact explains the damage initiation because the resistance of the material is 40 MPa in shear and 20 MPa in tension [3]. The back face displacement calculations correlate well with the experiments for $t=100 \mu s$ but there is a divergences for $t=200 \mu s$ (which can easily be explained by the fact that damage in the GRP is not taken into account in the constitutive equation used).

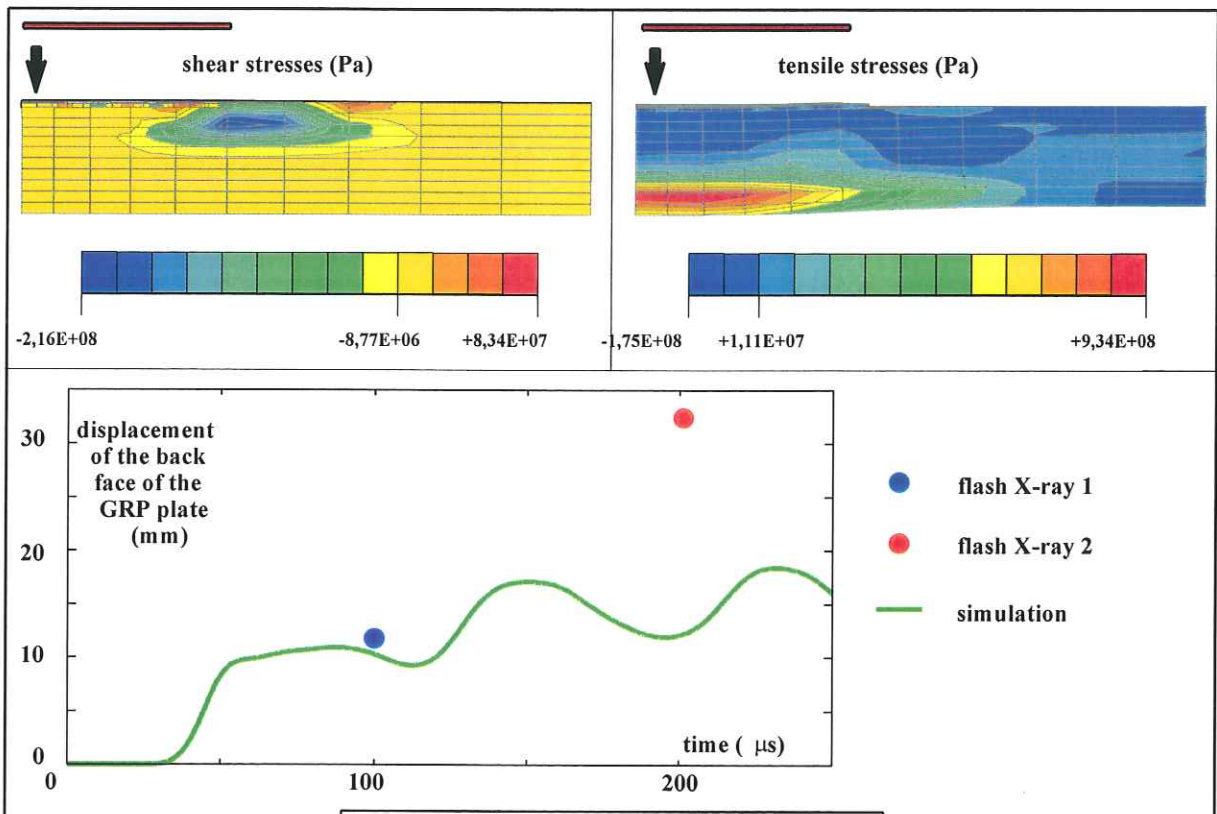


Figure 3: numerical simulation

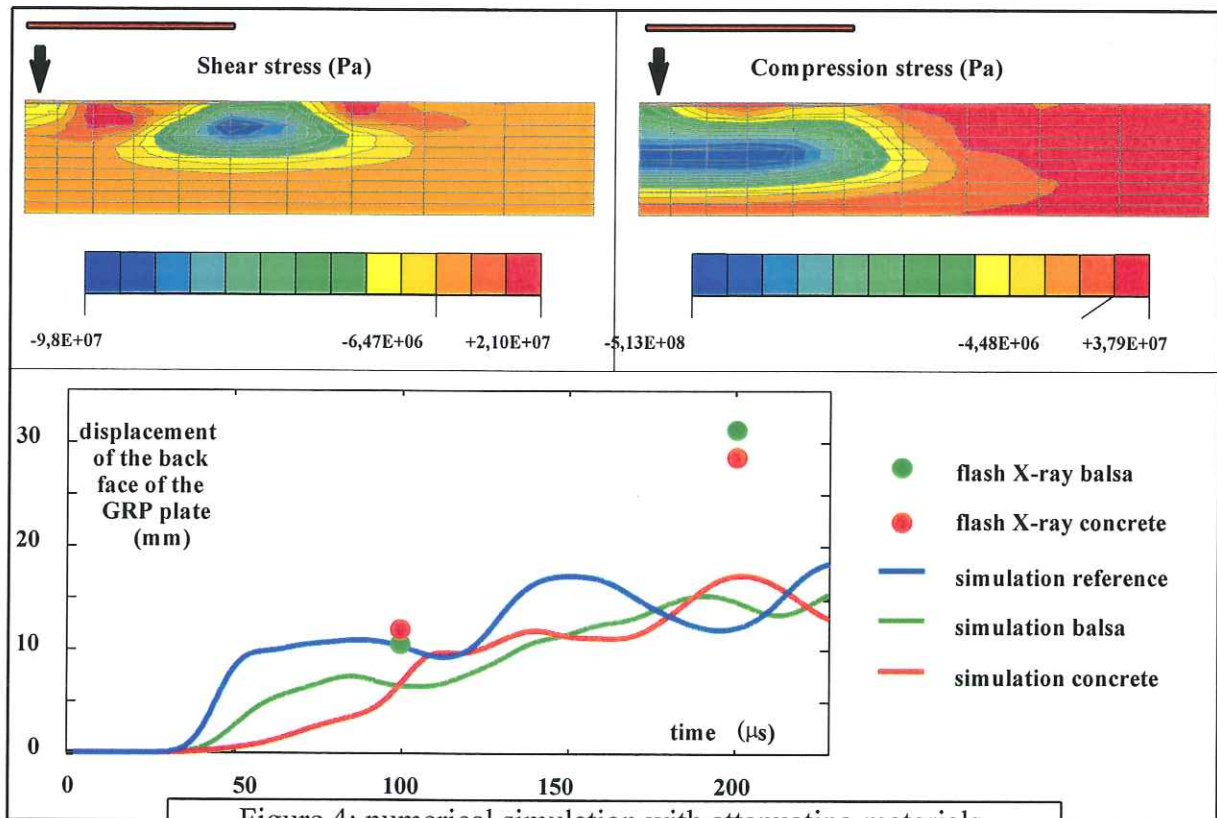
3 - INTRODUCTION OF AN ATTENUATING MATERIALS

Attenuating materials are able to absorb, attenuate and reduce or spread the effects of a compression shock wave [4]. Placed between the ERA and the GRP structure, these materials could limit the damage observed in the GRP.

3.1 - Numerical simulation

We consider the balsa and the air entrained concrete because the behaviour (s,e) have been evaluated at CTA using Hopkinson bars [5]. The simulation (figure 4) shows that the shear and tensile stresses are reduced by about 50 %. Also we note a less important gradient of stress: the shock wave is distributed in the thickness.

The difference of back face displacement between all the configurations is not important.. Like for the first simulations without attenuating materials (figure 3), a good correlation between the experiment and the simulation is obtained only for $t=100 \mu\text{s}$.



3.2 - Experimental results

To choice of an attenuating materials suitable for the considered application is not a simple task. In a first time, six off-the-shelf materials, known for their ability to absorb ballistic shock, are selected. They are described in Table III. In these experiments, the ERA is manually triggered in order to avoid the damage caused by the shape charge jet. The results are given in Table III in terms of displacement of the back face of the GRP plate at $t=100 \mu\text{s}$ and $t=200 \mu\text{s}$

For all the tested attenuating materials except high density honeycomb (HDHC), the difference with the reference is not significant. Nevertheless, the displacement of the back face of the GRP plate seems to be slightly smaller at $t=200 \mu\text{s}$ with Pyrex glass and expanded PVC. For these configurations, the front face is almost intact after impact and the delamination due only to the spalling phenomenon remains.

For the configuration with HDHC, the displacement of the back face of the GRP plate is much more smaller than that of the reference. The front face of the GRP plate is intact after impact and the delamination is greatly reduced. However, this encouraging result requires further tests for confirmation.

Table III : experimental results with attenuating materials

attenuating material	none (reference)	expanded PVC	balsa	air-entrained concrete	Pyrex glass	HDHC	PVC foam
density	--	0.75	0.25	0.6	2.2	0.9	0.25
thickness (mm)	--	57	40	50	40	50	50
H (mm) at $t=100 \mu\text{s}$	12	11	11	12	11	0	18
H (mm) at $t=200 \mu\text{s}$	32	27	31	29	26	3	37

4 - INTRODUCTION OF ADHESIVE LAYERS WITHIN THE GRP

Introducing one or several adhesive layers within the GRP theoretically presents two main advantages. Firstly, the incident shock wave is disturbed on the borderline between adhesive and GRP, because of their different characteristics (e.g. density, wave velocity). Secondly, if the adhesive has a good elongation capacity, the energy absorption by deformation should be greater.

4.1 - Preparation of the samples

The adhesive Crestomer, sold by the company Scott Bader, is chosen for this application. It is currently studied for the repairing of GRP naval structures. Its characteristics are presented in Table IV.

Crestomer joints are made by injection between two GRP plates with a controlled spacing. The absence of porosity is checked by destructive control on a test specimen. Two samples are processed, respectively composed of :

- two GRP plates having the same thickness joined by a Crestomer layer,
- four GRP plates having the same thickness joined by three Crestomer layers.

Table IV : characteristics of Crestomer

Young's modulus (MPa)	716
Yield stress (MPa)	11.9
Ultimate tensile stress (MPa)	15.9
Elongation at rupture (%)	51

4.2 - Experimental results

The two samples were impacted by the back plate of a manually triggered ERA. The results are given in Table V in terms of displacement of the back face of the samples at $t=100 \mu\text{s}$ and $t=200 \mu\text{s}$ (measured with flash X-ray).

It seems that the displacement of the back face of the samples does not depend on the number of adhesive layers. Moreover, at $t=200 \mu\text{s}$, this displacement is greater than that of the reference sample (no adhesive layer).

As it is shown in Figure 5, the GRP plates composing the samples are separated by the impact. The behaviour of Crestomer has become fragile under dynamic loading conditions. It can also be seen that the delamination mainly occurs in the last plate.

Table V : experimental results with adhesive layers

Number of adhesive layers	None (reference)	1	3
H (mm) at $t=100 \mu\text{s}$	12	11	10
H (mm) at $t=200 \mu\text{s}$	32	37	37

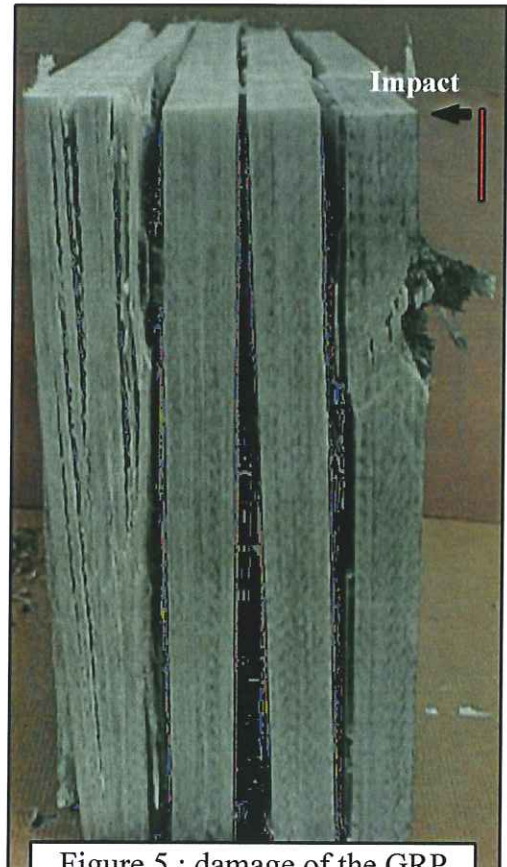


Figure 5 : damage of the GRP sample with 3 adhesive layers.

5 - CONCLUSION

We have seen that the configuration ERA + GRP is ballistically effective : the GRP plate is not perforated by the shape charge jet. However, the important damage observed in the GRP plate, essentially due to the impact of the back plate of the ERA, is not compatible with the considered application.

Introducing adhesive layers within the GRP was theoretically a potential solution to reduce this damage. However, the chosen adhesive appears to be brittle under dynamic loading conditions. It may thus be interesting to find another material exhibiting a ductile dynamic behaviour.

The use of attenuating materials to protect the GRP is not completely satisfactory. The impacted surface of the GRP plate is almost intact, but delaminations still occur within the GRP. This already raises the problem of the determination of an acceptable damage level for the GRP structures. Nevertheless, the use of high density honeycomb seems to allow a significant reduction of the delamination in the GRP, but this encouraging result requires further analysis and additional tests for confirmation.

Another way which could be explored to decrease the damage in the GRP is to enhance its mechanical characteristics. This could be achieved by modifying the fibre weaving in order to increase the tensile rupture strength of the GRP in the thickness direction.

REFERENCES

- [1] «Matériau structural pour caisse de char», note ETAS 94/166/SY/A/AB.
- [2] J.C. Mailé, B. Vivien, B. Hilaire, «Etude des propriétés mécaniques et de l'amortissement en fréquence d'un composite structural», rapport ETCA 94 R 074.
- [3] Trask, Court, «Quasi-static mechanical tests on thick laminates», Defence Research Agency, TD-11314-9601 Rev.0.
- [4] C. Kammerer, «Etat de l'art et synthèse des études dans le domaine des matériaux amortissants pour système d'arme», fiche n_ 49/98 CREA/SMS.
- [5] R. Descamp, «Etude expérimentale et numérique de matériaux amortissants», rapport CREA 97 R 077.

NEW TRENDS ON IMPACT MEASUREMENTS AND VIBRATION ANALYSIS BY HOLOGRAPHIC INTERFEROMETRY

J.F. Silva Gomes and M.A.P. Vaz

Unidade de Mecânica Experimental e Novos Materiais

INEGI/FEUP – Universidade do Porto

Rua dos Bragas, 4099 Porto, Portugal

ABSTRACT

Holographic interferometry and related techniques such as ESPI, TV-holography and Shearography, are very powerful tools in experimental mechanics, particularly for strain measurements, (both static and dynamic), vibration analysis and non-destructive testing.

The most recent successes in applying these techniques to experimental mechanics in general, and to impact and vibration measurements in particular, are undoubtedly associated to the latest developments on pulsed lasers, opto-electronic devices and acquisition and on the automatic fringes analysis by computer image processing routines, which have been making these optical techniques ever more powerful and user friendly.

This paper describes the state-of-the-art of such powerful optical methods and their applications to dynamic experimental mechanics problems and non-destructive inspection of solids and structures.

1. INTRODUCTION

The most recent developments in automatic computation techniques, particularly with the use of the powerful finite element methods (FEM) and other similar numerical tools, allow for the possibility of solving practically any problem in structural mechanics. In fact, today's demands for optimum design can be satisfied, to a great extent, by application of the finite element methods to solve problems for which exact solutions are non-existing, or are very difficult to obtain. However, results obtained by the finite element methods are subjected to the boundary conditions used, rely greatly upon an accurate knowledge of the material properties and a rigorous representation of the object geometry, and they are extremely sensitive to the shape and size of the elements used in modeling.

As is often the case with new and powerful methods, the FEM has been frequently over-used, perhaps even misused. And it is now fully accepted that, in spite of the enormous potentiality of such methods, virtually all versions of FEM contain some shortcomings. As a result of that, the need for coupling FEM in the physical and time domain with other experimental techniques has begun to manifest itself in recent years (see, for instance, Silva Gomes *et al.*, 1994). During the last two decades, the subject of *Experimental Mechanics* has been kept alive all over the world, assisting in the solution of many important physical and engineering problems of concern of society today. Furthermore, the latest developments on computer-based techniques as well as laser-based optical methods, among many other modern technological advances, have added a new dimension to the field of experimentation.

In the mechanical domain, laser interferometry techniques such as Holography, ESPI and Shearography, developed since the beginning of the sixties, have revealed themselves as extremely useful experimental tools for vibration, stress and strain analysis, and non destructive testing (NDT) of structures and mechanical components. Since the holographic interferometry was discovered in the early sixties (Haines and Hildebrand, 1966), it has been always a very interesting topic of research, with many applications in engineering and other fields (Vaz, 1995).

Each of those methods has certain characteristics which make it particularly useful in specific applications. In general, however, all of them have considerable advantages in comparison with other classical techniques for metrology, vibration and experimental stress analysis and quality control. They are fully non-destructive methods, inasmuch as there is no need for any physical contact with the specimen surface. They have a very high degree of sensitivity, allowing for the measurement of displacements with an order of magnitude of the light wavelength or even lower, and they do not require any special object surface preparation either. They also present the additional advantage of providing a global image of the displacements field over the object surface, making it easier to quickly identify stress concentrations or displacement gradients zones.

2. HOLOGRAPHIC INTERFEROMETRY

2.1. Recording and Reconstruction of an Hologram

Holography is an optical technique by which it is possible to record and reconstruct all the information contained in a given wavefront. In this technique, an original laser beam is divided into two beams, as shown in *Fig. 1(a)*. One of the beams (the so called object beam) is made interact with the object, or scene to be recorded, while the other (the so called reference beam) does not interact with the object at all. The two beams are made to overlap over a photographic plate, the result being that they interfere with each other, producing an interference pattern that is recorded. The exposed photographic film, after processing, becomes a hologram. The hologram is reconstructed with the same setup that was used in recording, except that now it is illuminated with the reference beam alone *Fig. 1(b)*.

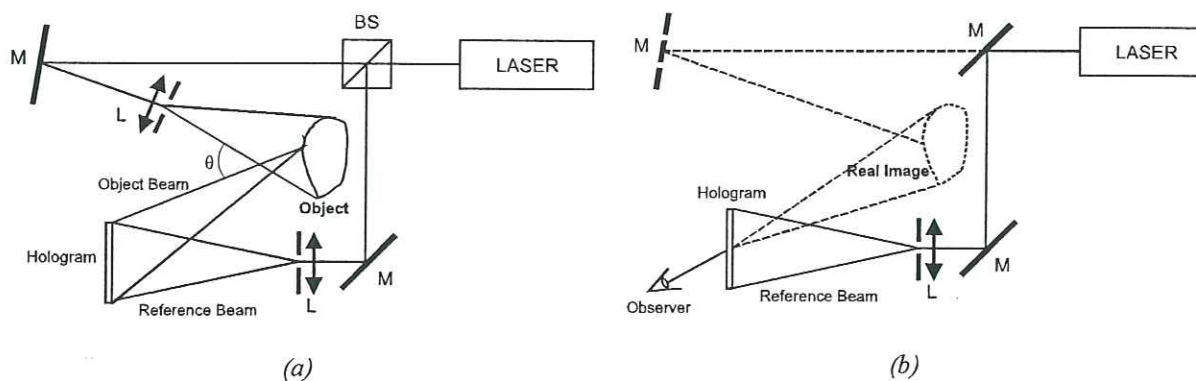


Fig 1: Recording (a) and reconstruction (b) of a hologram

The resulting wavefront fully reproduces the original one, and it is produced by diffraction of the incident radiation through the microstructure of the hologram plate. To observe this virtual image, the reconstruction should be viewed through the hologram as if it were a window. The image is seen in the same space which was occupied by the object while the hologram was recorded, even though the original object had since been removed. The image observed has all the visual characteristics of the original object. In fact, there is no visual test that can differentiate between the two.

A very important characteristic of the physical support to be used for recording the hologram is its spatial resolution, which should be high enough to record the interference pattern resulting from the superposition of the two wavefronts. The spatial frequency of this interference pattern, ν , depends upon the angle θ between the directions of the two beams, according to the following equation:

$$\nu = 2 \sin (\theta/2)/\lambda \quad (1)$$

where λ is the wavelength of the coherent light being used. Having a resolution that can be as high as 5000 lines/mm, photographic emulsions are the support most usually employed for holographic recordings, allowing for records with large values of angle θ .

2.2. Real-time Hologram Interferometry

This technique involves recording a single hologram as shown in *Fig. 1(a)*. The plate is then developed and placed back in its exact original position. The illuminated object and the hologram should then each produce identical wavefronts, from which results an increased brightness of the image of the object. Now, while observing through the hologram the two superimposed images, let the object be slightly loaded so that it deforms. The wavefront from the deformed object will be warped due to its deformation, while the wavefront reconstructed from the hologram remains unchanged. These wavefronts will interfere, producing dark fringes at points where they are $\lambda/2$, $3\lambda/2$, or any odd multiple of half wavelengths apart, *Fig. 2*. The particular advantage of the real-time method is that different types of motion, dynamic as well as static, can be studied with a single holographic expose. On the other hand, it requires a precise replacing of the plate back after development, which is time consuming and extremely difficult. It also requires a very high mechanical stability of the whole experimental setup.

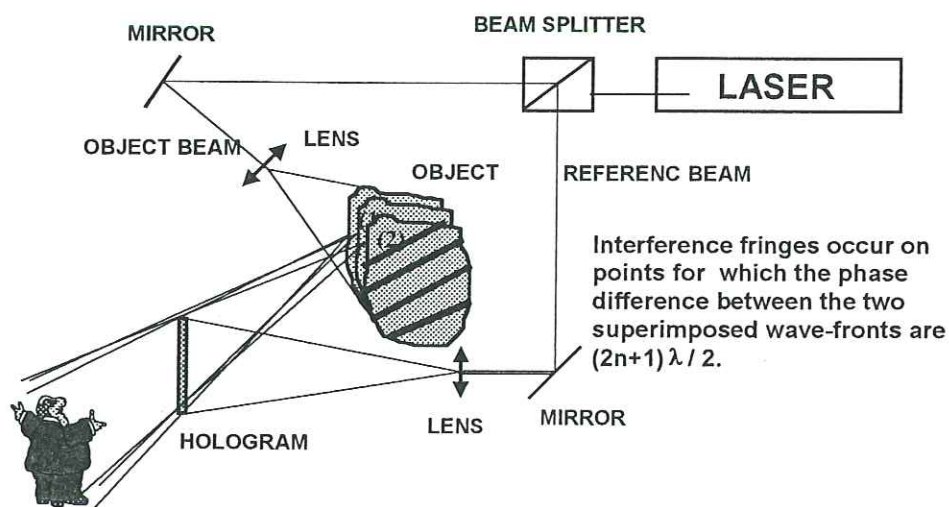


Fig 2: Formation of fringes in real-time interferometry

2.3. Double-Exposure Holographic Interferometry

In this method, the object is displaced and/or deformed between two holographic recordings of the same object on a single holographic emulsion. Therefore, the object beam during the second exposure is different from that used in making the first exposure.

During reconstruction of the double-exposure hologram, both object beams are faithfully reconstructed, forming images of the object's initial and final positions. Since these images are formed in coherent laser light, they interfere with each other forming a set of interference fringes superimposed over the image of the object. These fringes are a direct measure of changes in the object's position and/or shape which occurred between the two exposures. A typical double exposure fringe pattern obtained over the blade of a hydraulic shear machine is shown in *Fig.3*. The illumination and observation directions were nearly perpendicular to the blade surface; the fringes represent contours of out-of-plane displacement, at intervals of half the wavelength of the laser light.

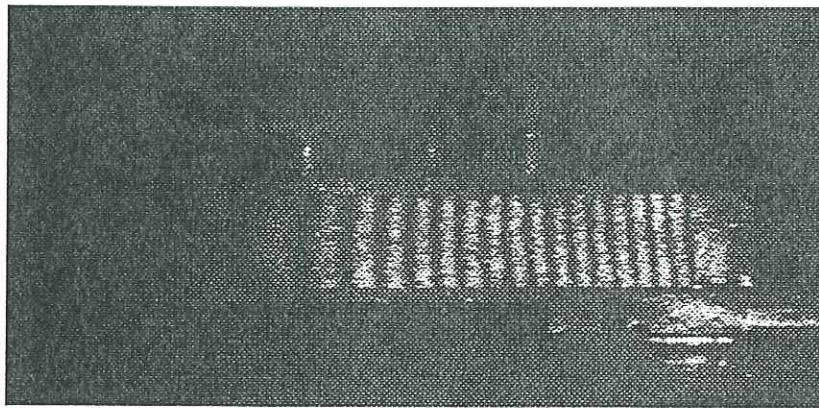


Fig. 3: Double exposure holographic fringes

2.4. Time-average Holographic Interferometry

Holographic interferometry can also be used for vibration analysis of structures. The object should be excited at one of its eigenfrequencies, while a single hologram is recorded in the usual way, except that the exposure time should be several times greater than the period of vibration. First proposed by Powell and Stetson (1965), this technique is called time-average holographic interferometry, and it is an effective way of recording and studying mechanical vibrations, giving direct information about the geometry of eigenmodes and other associated parameters. In the reconstruction of such a hologram, interference occurs between the entire ensemble of the recorded images, with the images recorded near zero velocity contributing most strongly. As such, images reconstructed from the time-average hologram have intensity distribution modulated by the zero-order Bessel function J_0^2 , *Fig.4*.

3. E.S.P.I. TECHNIQUE

The technique usually referred to as ESPI (*Electronic Speckle Pattern Interferometry*) can be thought of in terms of focussed image holography, in which a video target replaces the photographic emulsion used to record a conventional hologram. This allows for the possibility of obtaining 25 or 30 holograms per second (European or American TV-systems),

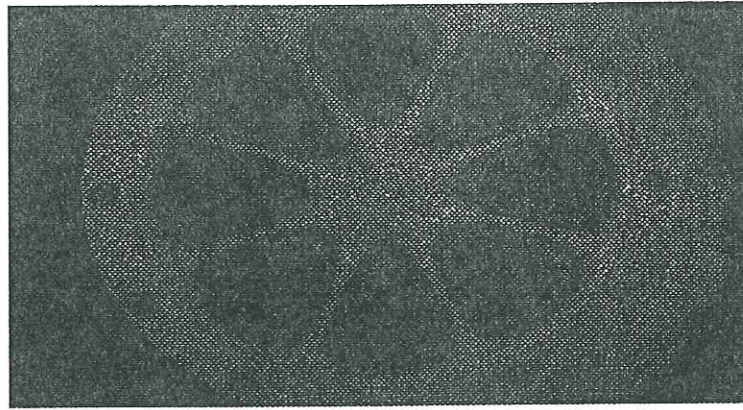


Fig. 4: Eigenmodes by time-average holography

without any chemical processing or repositioning of the hologram. The lower resolution of these detectors, (usually they do not go further than 50 lines/mm), implies the utilization of optical set-ups in straight line, where the angle θ , between the object beam and the reference beam, should be smaller than 1° (Løkberg and Slettemoen, 1987). With this alternative technique, it is necessary to use an optical system for the image of the speckle pattern over the surface of the object to be formed in the foto-sensitive area of a CCD detector, Fig. 5.

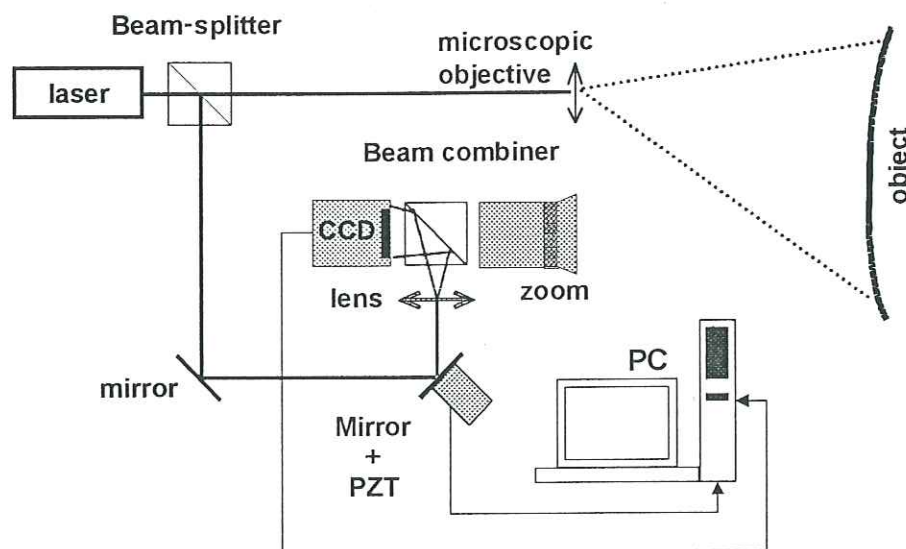


Fig. 5: Schematic diagram for the ESPI technique

There are mainly two different modes of operating an ESPI system: (i)-the time-average method, which is applied to study vibrating objects, and (ii)-the double exposure method, applied to deformation analysis. In both methods, the result is a fringe overlaid image of the object. These fringes are contours of equal amplitude vibration, in time average, or constante surface displacement in double exposure. The aperture of the optical system should be adjusted in order to guarantee that the speckle pattern is resolved by the photo-detector and stored in a digital image processing computer system.

While using ESPI, experimental data processing is strongly facilitated if control over the beam phase is available. This can be obtained by using phase shift techniques (by a PZT

For the application of shearography, always two shearograms of the same object, under two different stress conditions, have to be compared in order to obtain an interference fringe pattern. If the interferometric patterns are recorded in a CCD camera, the observations may be performed in real time, and image processing routines can be used to improve the experimental data analysis. The optical set-up represented above can be easily implemented in a compact system, as illustrated in *Fig. 8*.

The obtained interference pattern represents the out-of-plane displacement gradient across the direction of shear, its sensitivity being conditioned by the magnitude of the shear displacement. Notwithstanding the poor contrast of the images, in comparison with those obtained by other holographic techniques, shearography has become quite popular, mainly because it is almost insensitive to rigid body movements. In fact, being a common path interferometer, rigid body movements lead to the same influence in both arms of the interferometer, and therefore no fringes will appear associated to this type of movements. As it is sensitive to displacement gradients, it is well adapted to detect defects in structures that can lead to localized displacement gradients at the surface, as is the case of debonds and delaminations in composite materials (Silva *et al.*, 1994).

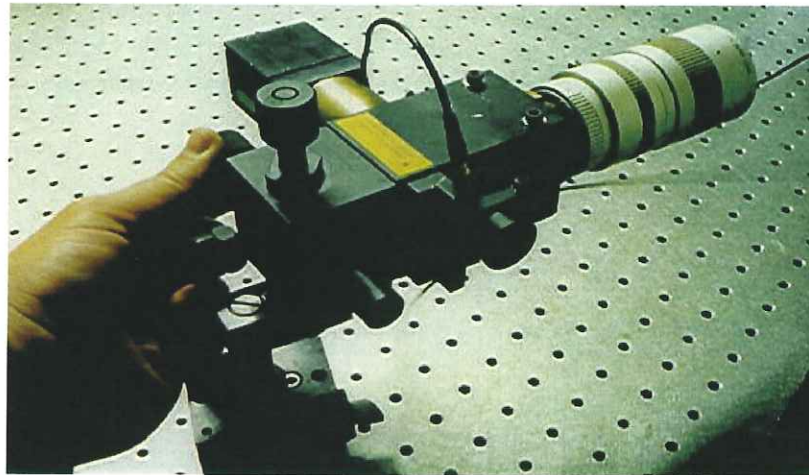


Fig.8: The Shearography compact head

In order to reveal localized defects in composite materials, thermal loading and under pressure are the most used stimulation methods to create the displacement/deformation gradients at the surface of the object, as indicated in *Fig.9*.

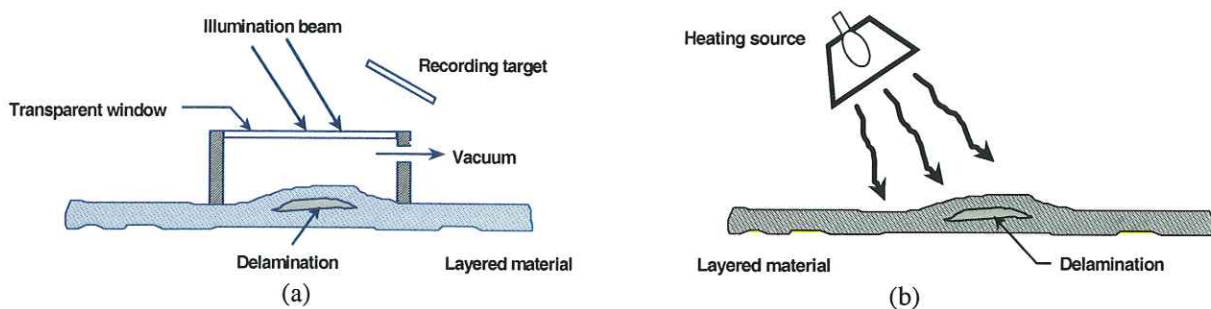
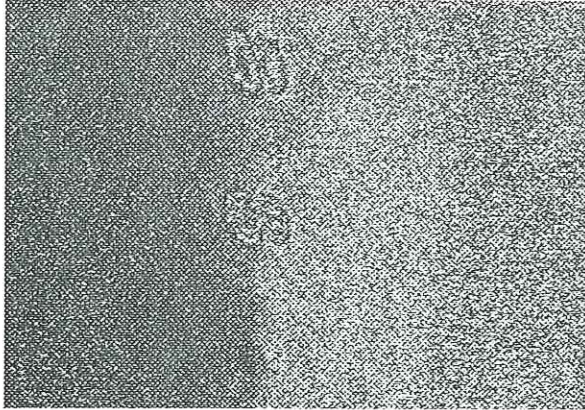
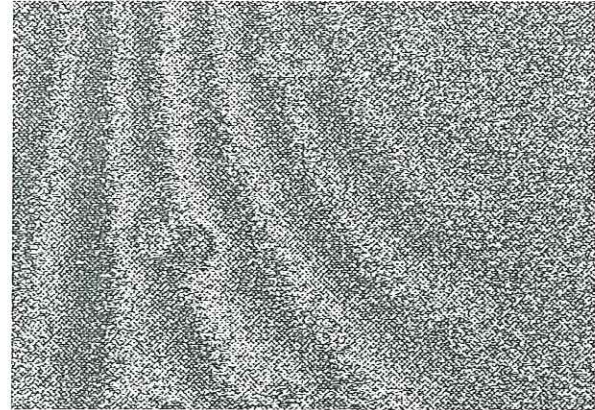


Fig.9: Stimulation methods (a)-under pressure; (b) thermal load

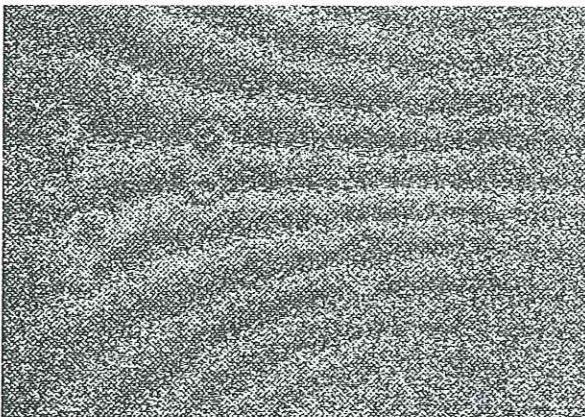
A set of different images obtained by shearography in detecting defects produced by impact on composite material aircraft components is shown in *Fig.10*. In obtaining all these pictures, thermal loading was the method used for stimulating the object. When using shearography technique, insensitiveness to environmental disturbances can still be increased if a pulsed laser is employed as the light source (Spooren et al., 1993).



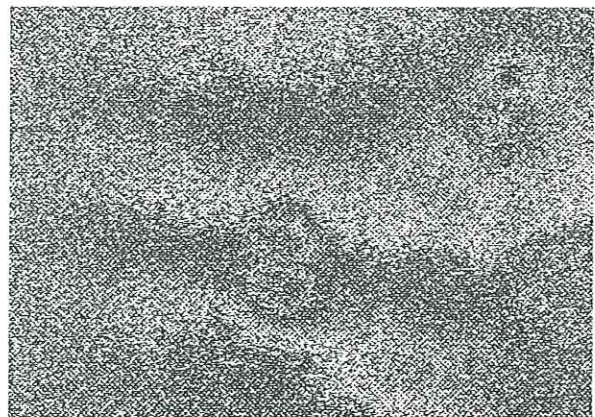
*Impact damages produced on a "Super-Puma"
fuselage sandwich panel (T300/Kevlar-49)
(scanning area: 0.4x0.4 m²)*



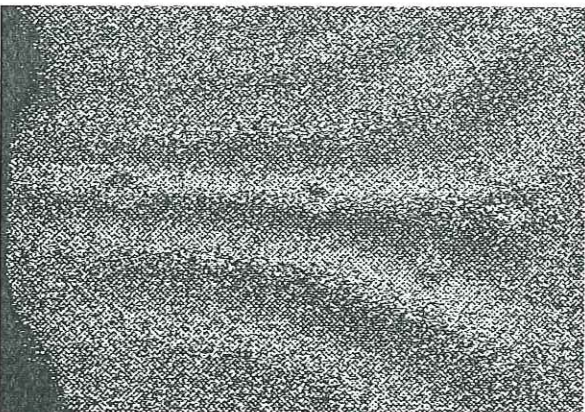
*Impact damages produced on a "C-130"
fuselage aircraft sandwich panel (GFRC)
(scanning area: A4 size)*



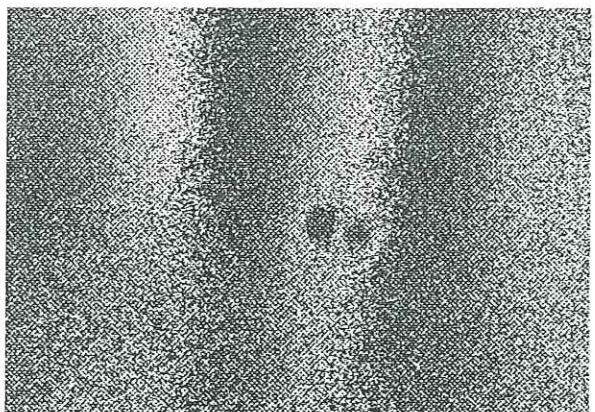
*Impact damages produced on a "C-130"
R/H stabilizer monolithic carbon-fiber panel
(scanning area: 0.5x0.5 m²)*



*Impact damages produced on a "C-130"
fuselage aircraft sandwich panel (GFRC)
(scanning area: A4 size)*



*Impact damages produced on a "C-130"
fuselage aircraft sandwich panel (GFRC)
(scanning area: 0.5x0.5 m²)*



*Impact damages produced on a "Super-Puma"
fuselage sandwich panel (T300/Kevlar-49)
(scanning area: A4 size)*

Fig. 10: Using shearography for detecting defects in aircraft composite panels

5. DIGITAL TV-HOLOGRAPHY

The resolution of CCD cameras and the capacities of personal computers have been constantly increasing during the past recent years, which make possible now to record holograms directly on a CCD camera, and reconstruct the wave front digitally. The work published by Schnards and Juptner (1994) has demonstrated that, at least within certain limits, it is possible to use CCD detectors to record *out-of axis* holograms, usually refered to as Fresnel holograms. With this optical set-up, a video detector is used for recording the interference pattern withthout the need of any lens to form the object image. The reconstruction of the recorded image is made numerically by computation of the two-dimensional Fourier Transform of the interference patterns. This new technique, usually refered to as Digital TV-Holography, enables obtaining correlation fringes corresponding to displacements and the immediate storage of images in digital memory devices, and direct phase calculation with only one interference pattern, so it is well adapted to industrial applications.

Although the procedure for recording the hologram is identical to that used with photographic emulsions, the reconstruction of the video recorded image is obtained in a quite different way. In fact, the technique consists in obtaining the recorded wavefront from a numerical reconstruction performed over the real-image plane. Numerically, this can be done by an approximation to Fresnel theory in terms of discrete Fourier Transform, for which it can be used one of the many FFT algorithms available. The discrete representation of the Fresnel-Kirchhoff integral will then be obtained from the following expression (Yaroslavskii 1980, Schnars 1994):

$$\Gamma(r, s) = \exp\left[-i \frac{\pi}{\lambda \cdot d} \left(r^2 \Delta \xi^2 + s^2 \Delta \eta^2\right)\right] \cdot \sum_{l=0}^{M-1} \sum_{k=0}^{N-1} t(k, l) \cdot \exp\left[-i \frac{\pi}{\lambda \cdot d} \left(k^2 \Delta x^2 + l^2 \Delta y^2\right)\right] \cdot \exp\left[i \cdot 2\pi \left(\frac{k \cdot r}{N} + \frac{l \cdot s}{M}\right)\right] \quad (2)$$

where $\Gamma(r, s)$ is a matrix of $N \times N$ points, which describes the amplitude/phase distribution of the image, (r, s) are object plane coordinates, λ is the wavelength of illumination source, d is the distance between the hologram and object planes, $\Delta \xi, \Delta \eta$ are the pixel dimensions of object plane image, (k, l) are the object coordinates and $\Delta x, \Delta y$ are the pixel dimensions of the CCD target. *Fig. 11(a)* represents an interference fringe pattern in the photo-detector plane, and *Fig. 11(b)* shows the result obtained after reconstruction of the hologram.

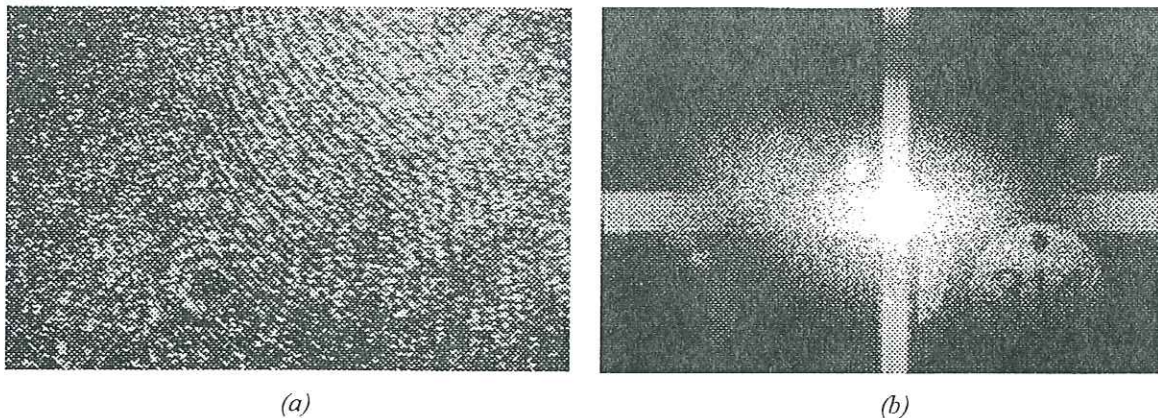


Fig. 11: Digital holographic interference pattern (a) and numerical reconstruction of the hologram (b)

As in classical holographic interferometry, interference fringe patterns can be obtained by correlating two or more digital holograms of the same object. Digital interferograms may be obtained either by addition (as in classical holographic interferometry) or by subtraction of the holograms corresponding to the two positions of the object (Chousal *et al.*, 1998). *Fig. 12* shows the fringe patterns obtained for a metallic circular membrane subjected to a perpendicular concentrated load at the centre (a) correlation by addition of two holograms and (b) correlation by subtraction of the same two holograms.

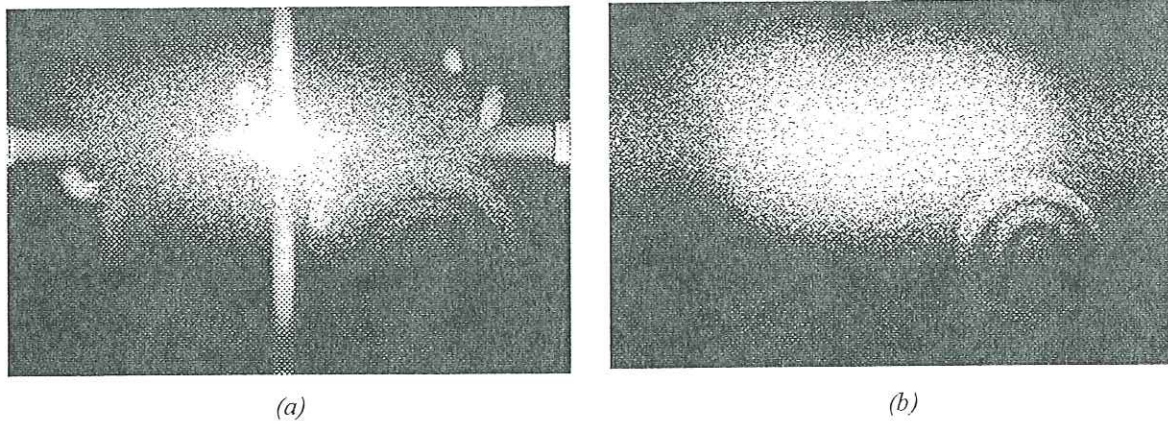


Fig. 12: Interferograms obtained by correlation of two holograms
(a) correlation by addition, (b) correlation by subtraction

By using the subtraction technique, the elimination of the zero order intensity term is achieved, allowing for a considerable improvement of the contrast (compare figures 12a and 12b).

6. IMAGE AND DATA PROCESSING

When image processing is used together with holographic interferometry techniques, quantitative measurements are possible, keeping all characteristics of the optical procedures involved and shortening the time necessary for data analysis. Usually the phase distribution must be calculated, which can be done by using quasi-heterodyne techniques, in classical holographic interferometry (Dandliker and Thalman, 1985), and phase shift techniques in ESPI and Shearography (Creath, 1994). Typically, phase distribution with a resolution up to one hundredth of a fringe can be easily obtained.

Because three or four fringe interferometric patterns with different phases are generally involved, these techniques require that the setup must be kept stable during the time used for data recording. More recently, techniques like digital holography (Schnards and Juptner, 1994) and image digital holography with a slightly off-axis reference (Pedrini *et al.*, 1993) were developed, which allow for phase calculations with a single interferometric recording. The major limitation of these methods can be found in the pixel by pixel calculation of an arc tangent function which is bounded in the range 0 to 2π . This phase distribution is commonly referred to as the wrapped phase map, *Fig. 13(a)*.

The process of converting the wrapped map in a continuous phase variation is called phase unwrapping, *Fig. 13(b)*, and this operation has become one of the most challenging problems and object of intensive investigation in the recent years.

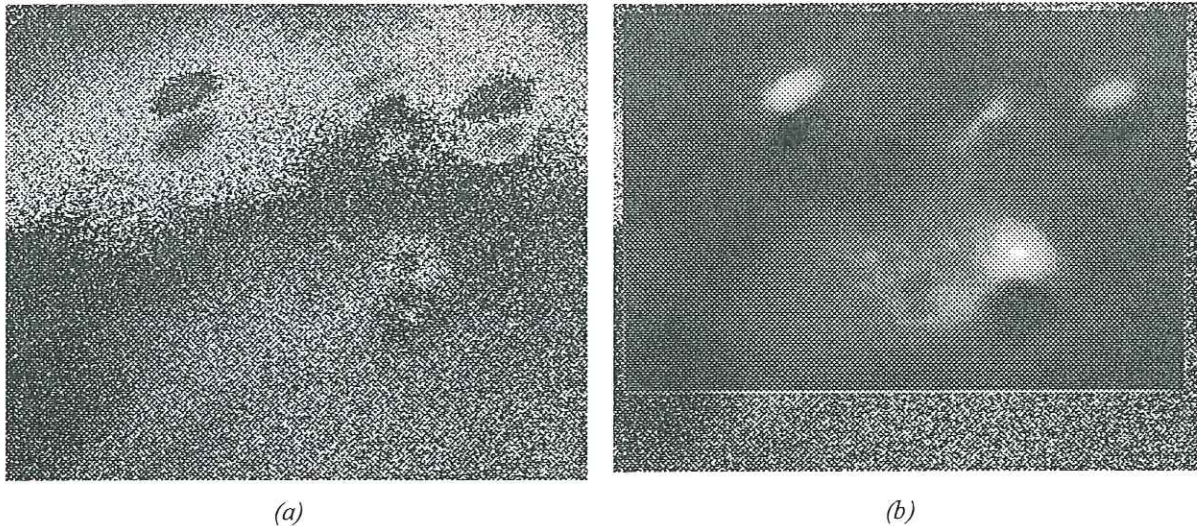


Fig. 13: Phase map image (a) and corresponding unwrapped phase image (b)

7. APPLICATION TO TRANSIENT PROBLEMS

To be possible to apply the phase determination techniques in holographic interferometry to dynamic events, it is necessary to have the possibility of recording the phase for a given position in only one image. Both techniques described above allow those conditions.

The other necessary condition is the use of a laser that grants the emission of two extremely close pulses. Due to time separation involved in double pulse sequence ($10\mu\text{s}$ - $500\mu\text{s}$) we need to use a CCD camera that simultaneously transfers accumulated charge fields from all even/odd lines to the shifted registers. This can be achieved by using an interline transfer type CCD camera.

As Spooren (1991) has shown, it is possible to record two image holograms in consecutive odd fields of an interline transfer CCD, *Fig. 14*. The first pulse arrives just before the charge transfer takes place, while the even field is being read. The second pulse occurs after the charge transfer has been completed. The next odd field after the first pulse contains the accumulated charge from the first exposure. When the second pulse arrives the odd lines are empty, while the even still contain the first pulse charge. Thus the next odd field contains only the charge corresponding to the second pulse. With this technique, the resolution is reduced by half, since only odd lines are used to register the image hologram.

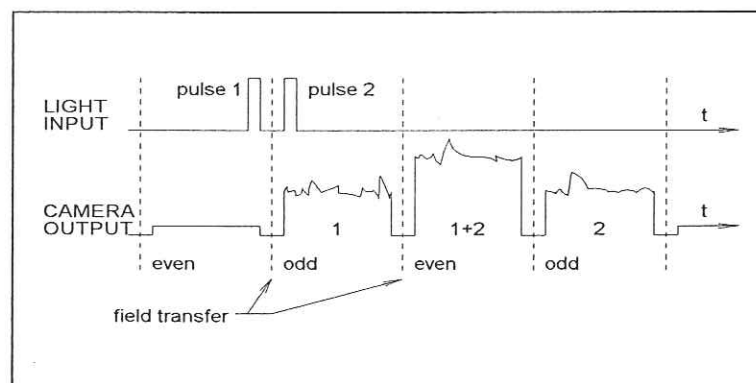


Fig 14 : Timing diagram of a double pulse system (after Spooren, 1991).

If one needs to record images corresponding to more than two instants, further cameras should be used. The difficulty with a multi-camera system is the alignment, since all the images must contain exactly the same area.

8. CONCLUSION

Although only some very few of the numerous examples have been mentioned, this review demonstrates that already early after the development of lasers, by which holography became a practical tool, the different holographic techniques have been used extensively in stress/strain analysis and NDT of structural components and materials. Today, holography and all other related techniques have strongly established their place for experimental mechanics and materials research, both in physics and engineering applications.

In recent years, the extraordinary capabilities of these techniques have been strongly enhanced by the use of image processing routines based upon micro computer systems, easily adapted to a rapid automatic data recording and processing of interferometric patterns. Furthermore, the combined use of these techniques with pulsed lasers will allow, in the very near future, for the design of interferometric systems almost insensitive to environment disturbances

Finally, the miniaturization of high power pulsed lasers, and the increase of CCD cameras resolution and personal computer capabilities will undoubtedly lead to the spread of these techniques as NDT tools, with the possibility of *on site* use, in ordinary industrial environments.

ACKNOWLEDGEMENTS

The work presented in this paper has been supported by FCT (Fundação para a Ciência e Tecnologia), under the Pluriannual Research Funding Programme, and by the Ministry of Defense (Portugal).

REFERENCES

- Creath, K., 1988, "Phase-Measurements Interferometry Techniques", *Progress in Optics*, Vol. XXVI, E. Wolf, Ed., Elsevier Science Publishers, Amsterdam, pp. 351-393.
- Creath, K., 1994, "Phase-Shifting Holographic Interferometry", *Holographic Interferometry*, P.K. Rastogi, ed., Springer-Verlag, Vol. 68, pp. 109-150.
- Dandliker, R. and Thalman, R., 1985, "Heterodyne and Quasi-Heterodyne Holographic Interferometry", *Optical Engineering*, Vol. 24, n° 5, pp. 179-181.
- Haines, K.A. and Hildebrand, B.P., 1966, "Surface-Deformation Measurement Using the Wavefront Reconstruction Technique", *Applied Optics*, Vol. 5, n° 4, pp. 595-602.
- Leendertz, J.A. and Butters, J.N., 1973, "An Image-Shearing Speckle-Pattern Interferometer for Measuring Bending Moments", *Journal Of Physics E: Scientific Instruments*, Vol. 6, pp. 1107-1110.
- Løkberg, O.J. and Slettemoen, G.A., 1987, *Basic Electronic Speckle Pattern Interferometry*, Applied Optics and Optical Engineering, Vol. X, Academic Press Inc., New York.

- Pedrini, G., Pfister, B. and Tiziani, H., 1993, "Double Pulse-Electronic Speckle Interferometry", *Journal of Modern Optics*, pp. 89-96.
- Powell, R.L. and Stetson, K.A., 1965, "Interferometric Vibration Analysis by Wavefront Reconstruction", *Journal of Opt. Soc. of America*, Vol. 55, No. 12, pp.1593-1598.
- Schnards, U. and Juptner, W., 1994, "Direct Recording of Holograms by a CCD Target and Numerical Reconstruction", *Applied Optics*, Vol. 33, No. 2, pp. 179-181.
- Silva, J.F., Justo, J.M., Chousal, J.A., Vaz, M.A.P., Marques, A.T. and Silva Gomes, J.F., 1994, "Non-Destructive Testing of Composite Structures Using Shearography", *Recent Advances in Experimental Mechanics, Proceedings of the 10th International Conference on Experimental Mechanics*, J.F. Silva Gomes *et al.*, eds., A. A. Balkema, Rotterdam, The Netherlands, pp. 373-378.
- Silva Gomes, J.F. *et al.*, 1994, *Recent Advances in Experimental Mechanics*, A. A. Balkema, Rotterdam, The Netherlands.
- Spooren, R., 1991, *Fringe quality in pulsed TV-holography*, Proc. SPIE. 1508: 118-127.
- Spooren, R., Dyrseth, A.A. and Vaz M.A.P., 1993, "Electronic Shear Interferometry Applying a (double) Pulsed Laser", *Applied Optics*, Vol. 32, n° 25.
- Vaz, M.A.P., 1995, *Laser Interferometry and Hybrid Techniques in Experimental Mechanics*, PhD. Thesis, Faculty of Engineering, University of Porto, Portugal.

Impact Behaviour of Magnesium Matrix Composites

Lach E., Kainer K. U.*, Wellige B., Bohmann A. und Scharf M.

ISL, French-German Research Institute of Saint-Louis, F-68301 SAINT-LOUIS

*GKSS, Research Center, Institute of Materials Research, D-21502 GEESTHACHT

The aim of this work is to study the behaviour of short-fiber and particle-reinforced magnesium alloys under dynamic compression load and to evaluate their ballistic performance. Three magnesium alloys, AZ91, QE22 and WE54, were used as matrix materials. Reinforcing materials were 20% short-fiber- Al_2O_3 (Saffil[®]) and 15% SiC-particles combined with 7.5% Saffil[®] (mixed). Composites were produced by squeeze casting. Short-fiber and particle strengthening of magnesium alloys was undertaken to improve properties such as wear resistance, elastic modulus and compression strength. All composites were studied by quasi-static and dynamic compression tests (Hopkinson bar) and compared to long and short fiber-reinforced plastics and to unreinforced magnesium alloys. The influence of matrix material and the anisotropy caused by reinforcing fibers were studied. Fractures were investigated by means of a scanning electron microscope. A metallographic study of microstructure was also performed. The behavior of magnesium matrix composites was studied at a projectile velocity of 1700 m/s. The rod (a tungsten sinter alloy) geometry was 4 mm in diameter x 60 mm long ($L/D = 15$). The target materials used were AZ91, QE22 and WE54 reinforced with 20% Saffil[®] and AZ91 reinforced with 18% carbon short fibers. Impacts caused fractures of these composites. The influence of a backing consisting of unreinforced matrix alloy was also studied. A composite of QE22 reinforced by 7.5% Saffil[®] and 15% SiC-particles with a backing of the same matrix material showed no fragmentation.

1. Introduction

Fiber-reinforced composites with titanium or aluminium as a matrix have for some time been used in the aerospace and motor industries. Due to the promising results reported during the development of these alloys, research has been concentrated on reinforcing the light metal magnesium and its alloys with alumina fibers. Magnesium and its alloys are the engineering materials with the lowest density. The strengthening of magnesium alloys is undertaken to improve critical properties such as elastic modulus, high-temperature strength, wear resistance and thermal expansion.

The low-rate mechanical properties and failure mechanisms of reinforced Mg-alloys have been well characterized [1, 2, 3]. References [4, 5] describe the application of Mg-based composites to the construction of sabots. The influence of particle volume fraction and shape on the behavior of metal-matrix composites at high strain rates was studied in [7].

This work aims at studying the behavior of Mg-based composites in dynamic compression tests and at investigating their ballistic behavior. Dynamic compression tests were performed on a split-Hopkinson-pressure-bar. The diameter and the length of the bars were 20 mm and 1000 mm, respectively. The dimensions of the specimens were 12 mm in diameter and 8 mm in length.

2. Materials

Three magnesium alloys, AZ91, WE54 and QE22, have been chosen as matrix materials. Table 1 shows their chemical compositions. WE54 and QE22 are high-temperature alloys. The mechanical properties obtained by tensile test can be seen in table 2.

Table 1: Chemical composition of Mg-alloys in %

	Al	Zn	Mn	Y	R. E.	Nd	Zr	Ag	Nd rich R. E.	balance
AZ31	3	1	0.3							Mg
AZ91	9	0.7	0.2							Mg
WE54				5.1	1.5	1.8	0.5			Mg
QE22							0.6	2.5	2	Mg

Table 2: Mechanical properties of unreinforced Mg-alloys obtained by tensile test

	R _{p0.2} , MPa	R _m , MPa	A, %	Young's modulus	density
AZ31	160	245	10	40 - 45 GPa	1.8 g/cm ³
AZ91	170	270	4.4	40 - 45 GPa	1.8 g/cm ³
QE22	205	266	4	40 - 47 GPa	1.82 g/cm ³
WE54	205	280	4	40 - 47 GPa	1.85 g/cm ³

Magnesium alloys fiber strengthening has been undertaken in order to improve their properties. The preferred fiber material is Saffil from ICI as, in addition to having the required properties, it is relatively cheap. Saffil consists of δ -Al₂O₃ and has a tensile strength of 2000 MPa, a Young's modulus of 300 GPa, a Mohs hardness of 7 and has a diameter of 3 μ m x 60 μ m [2].

Additionally, a mixed Saffil-SiC_p-Mg-composite and a carbon short-fiber Mg-composite were studied. The diameter of SiC-particles (Mohs hardness 9.7) was 6.2 μ m and the C-fibers had a diameter of 7 μ m x 170 μ m.

The reactivity between the alumina fibers and the magnesium matrix is important as this influences the overall properties of the fiber-reinforced alloy [6]. Reactions may take place during manufacturing while magnesium is still molten or solid-state reactions may also occur during heat treatment. The reinforced Mg-composite was manufactured by using squeeze casting [8].

The Saffil-fiber content amounts to 20 vol.-% and the C-fiber content amounts to 18%. A preform for the mixed Mg-composite consists of 7.5% Saffil and 15% SiC-particles. Figure 1 shows the structure of an AZ91-based composite with 20% Saffil fibers. In preforms, as a result of the manufacturing process, the fibers are randomly oriented in a plane. Infiltration of preforms is carried out predominantly perpendicular to the fibers. The microstructure of the composite is influenced by the solidification behaviour of the matrix alloy. Generally, the fiber addition results in a refinement of the microstructure. The typical cast structure of AZ91 has large regions of Mg₁₇Al₁₂ surrounded by lamellar precipitates of Mg₁₇Al₁₂.

Conventional short-fiber reinforced alloys produced by liquid infiltration show anisotropic properties as a result of the planar isotropic fiber orientation. Particle-reinforced alloys show isotropic properties, but they were normally produced by stir cast, as the infiltration of preforms with fine particles requires a minimum of particles content. The use of mixed reinforcement avoids this problem [3].

3. Quasi-static and dynamic compression tests

Figure 2 shows quasi-static compression tests using unreinforced AZ91 cast alloy and AZ31 wrought alloy as well as Saffil-fiber reinforced AZ91. The compression strength of the composite is remarkably increased, compared to the unreinforced matrix alloy, but the strain to failure is reduced to less than 5%. Tensile stress is induced in fibers by shear stress at the fiber/matrix interface during the plastic deformation of a ductile matrix. Due to this

micromechanism, the high tensile strength of Saffil fibers can be used. This micromechanism mainly affects the macroscopic compression strength. Short fibers also serve as obstacles to dislocations. Strain to failure is reduced because the formation of an internal compression cone is impossible.

As compared to the quasi-static compression tests (figure 2), the dynamic compression tests (figure 3) show the strain rate sensitivity of the three materials. At higher strain rates the hardening component due to dislocation generation increases [9]. The strain to failure in compression of the composite is slightly increased. The higher strain rate increases the local flow stress. This affects the growth of voids and the formation of microcracks is delayed. Only the matrix alloy AZ91 has a reduced strain to failure. AZ91 is a diecast alloy and solidification during squeeze casting is not fast enough. This leads to a coarse grained microstructure. The eutectic composition between primary solidified dendrite crystals is rigid.

Specimens in three axes have been taken from a plate consisting of AZ91-based composite. The orientation of fibers in the specimens can be seen in figure 1. Figure 4 shows the dynamic compression flow curves of the specimens. It shows that the behaviour is quite different in the Z-axis as compared to the X- and Y-axes. The Z-axis is perpendicular to the fiber orientation. The compression strength decreases whereas the ductility increases. Mechanical properties in the X- and Y-axes are quite similar, due to the identical fiber orientation. The strain to failure in the compression of specimens 1 and 2 in figure 4 also confirms an increase in ductility under dynamic load.

Three magnesium alloys reinforced by 20% Al₂O₃-short fiber have been studied in order to find out the influence of the matrix alloy. Figure 5 shows the dynamic compression curves of the three composites. The AZ91-based composite has the highest compression strength. The QE22-based composite is the most ductile material but its compression strength is slightly lower compared to the AZ91-based composite. The brittleness of the WE54 alloy leads to a composite of minor efficiency at ambient temperature.

A reinforcement using SiC-particles mainly increases Young's modulus and the flow stress. AZ91 has a Young modulus of about 45 GPa. Short-fiber reinforcement (Saffil) increases it to 55 GPa. Young's modulus reached by the SiC-particles reinforcement is significantly higher than that obtained by short-fiber reinforcement [3]. Particle reinforcement mainly acts as an obstacle to dislocations. This mechanism does not increase the compression strength as effectively as the micromechanism due to short-fiber reinforcement. Figure 6 shows dynamic compression tests with mixed and short-fiber reinforced AZ91. The compression strength of short-fiber reinforced alloys is always higher.

4. Ballistic tests

The target configuration and details of the ballistic tests can be seen in figure 7. A semi-infinite target of 330 HB30 hardness was used as reference. The E_m -values in figures 9 and 11 represent the thickness of the tested composite and the residual penetration in the backing. The E_m -value for the backing material (semi-infinite target) is also included. In a first test series only the reinforced region (figure 8) was used. Additionally, the reinforced region embedded in the solidified remaining melt (figure 8) was also investigated. For these tests the thickness of the reinforced zone was varied from 20 mm to 48 mm.

Figure 9 shows the results obtained on plates of Mg-based composite. The thickness was 20 mm for all plates. The solidified remaining melt was removed from the reinforced plates by rotary grinding. AZ91 reinforced by 20% Saffil shows the best result. C-fiber reinforcement is less effective because of its poor bonding with the matrix alloy AZ91. Tensile stress cannot be induced optimally into C-fibers. In figure 10 a fractured region of C-

fiber reinforced AZ91 can be seen. A lot of C-fibers are loosened from the matrix alloy. This means that the interface between the C-fibers and the matrix alloy is of minor quality.

Figure 11 shows ballistic results with plates in the as-cast status (figure 8). The confinement and backing of a Mg-composite consist of the same matrix alloy. For that reason good impedance adaption is achieved. All mixed reinforced alloys show comparable results. Mixed reinforcement has a significantly better ballistic performance than short-fiber reinforcement, though the dynamic compression strength is higher. SiC-particles influence the ballistic results by erosion of projectiles. The mixed reinforcement of AZ91 was performed in three thicknesses. As during squeeze casting (AZ91 is a diecast alloy) the remaining melt of AZ91 cannot be solidified fast enough, the coarsening of grains occurs and the alloy becomes rigid. So no influence of backing and thickness of the reinforced region can be found out.

The plate using QE22 as matrix alloy shows cracking only along the interface between the reinforced and unreinforced regions (figure 12), but no catastrophic cracking occurs. QE22 forms intermetallic phases which act as a grain refinement additive. The grain size amounts to one third of that of AZ91 and the ductility increases. Two ballistic tests using the same plate could be performed.

5. Conclusion

Short-fiber and particle-reinforced magnesium alloys also have excellent properties also under high dynamic load. A SiC-particle reinforcement mainly increases Young's modulus and a short-fiber reinforcement increases the compression strength. Ballistic tests show that SiC-reinforced Mg-based composites have a better ballistic performance than short-fiber reinforced Mg-based composites in spite of their lower compression strength. SiC-particles cause an erosion of projectiles. QE22 is more ductile than AZ91 if it is squeeze-cast. Short-fiber reinforced Mg-based composites are suitable for components which are exposed to a dynamic load like sabots, for instance.

References

1. Kainer K. U., Mordike B. L., *Herstellung und Eigenschaften von kurzfaserverstärkten Magnesiumlegierungen*, Metall, 44 (1990), pp. 438-444
2. Kainer K. U., Mordike B. L., *Magnesium-Alumina Composites-Production and Properties*, Proceedings Verbundwerk '90, S. 17.1 - 17.15, Ed.: Schnabel S., FNW Forschungsinstitut Neue Werkstoffe, Frankfurt, BRD, 1990
3. Kainer K. U., *Isotropic Properties of Mixed Saffil-SiC_p-Magnesium Composites*, Advanced Composites 93, Eds.: Chandra T., Dhingra A. K., The Minerals, Metals & Materials Society, 1993, pp. 1,213-1, 219
4. Lehr H.F., Lach E., Wiese U., Bohmann A., *On the Application of Fiber-Reinforced Materials of Low Density in Construction Elements Subjected to High Loads*, in: J. Phys IV France 7(1997), Euro Dymat, Toledo, Spain, 1997
5. Lach E., Bohmann A., Wiese U., Lehr H.F., *Untersuchung eines Magnesium-Aluminiumoxyd-Verbundwerkstoffs auf seine Verwendbarkeit in der Treibspiegeltechnologie*, PU 322/96, 1996
6. Li Y., Ramesh K. T., *Influence of Particle Volume Fraction, Shape, and Aspect Ratio on the Behavior of Particle-Reinforced Metal-Matrix Composites at High Rates of Strain*, Acta mater., 46 (1998), pp. 5633-5646
7. Gräf L., Kainer K. U., *Effect of Heat Treatment on Alumina Short-Fiber-Reinforced Magnesium Composites*, Prak. Metallogr. 30 (1993), pp. 540-557
8. Kainer K. U., Böhm E., *Squeeze-Casting of Magnesium Alloys*, VDI Reports No1235, 1995, pp. 117-125
9. Vaidya R. U., Song S. G., Zurek A. K., *Dynamic Mechanical Response and Thermal Expansion of Ceramic Particle Reinforced Aluminium 6061 Matrix Composites*, Philosophical Magazine A, 70 (1994), pp. 819 - 836

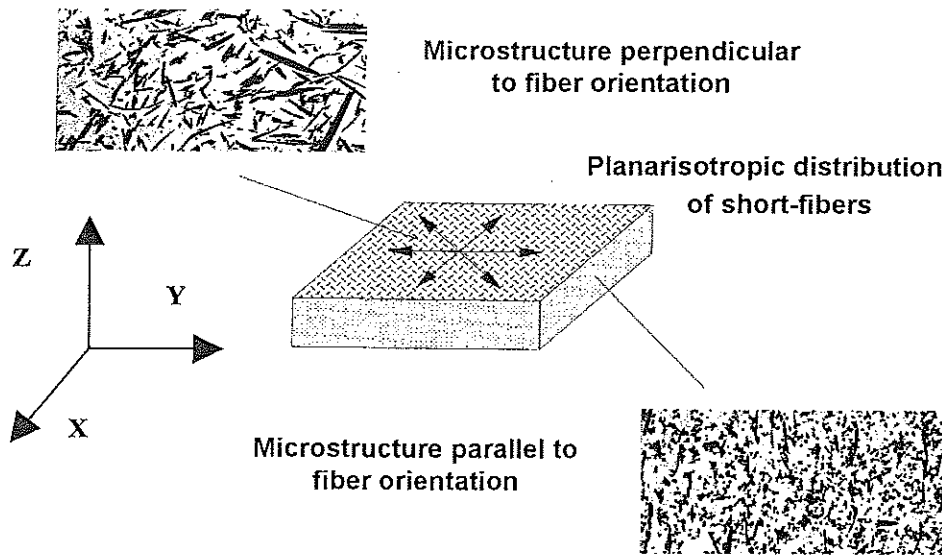


Figure 1: Microstructure of short-fiber reinforced AZ91

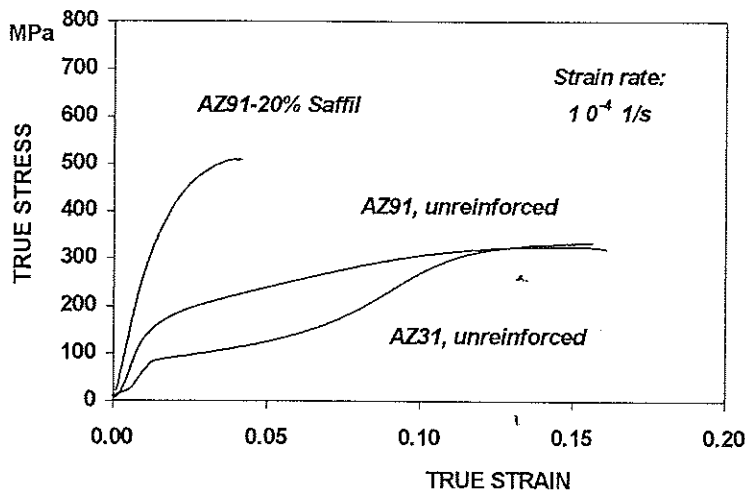


Figure 2: Quasistatic compression tests

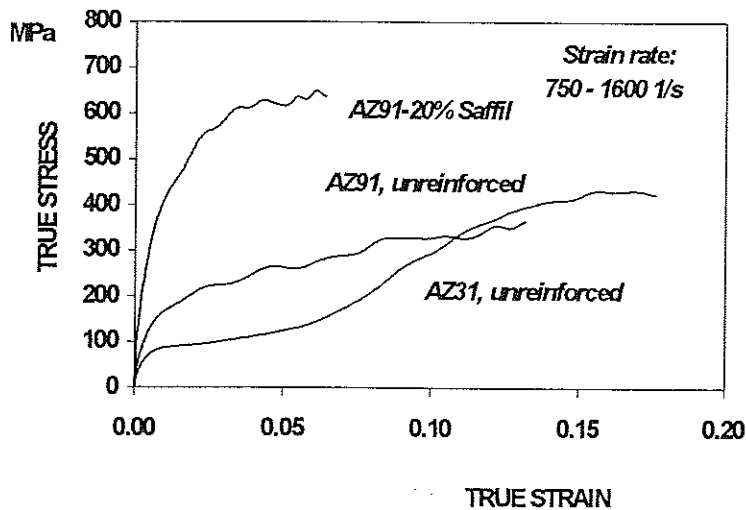


Figure 3: Dynamic compression tests

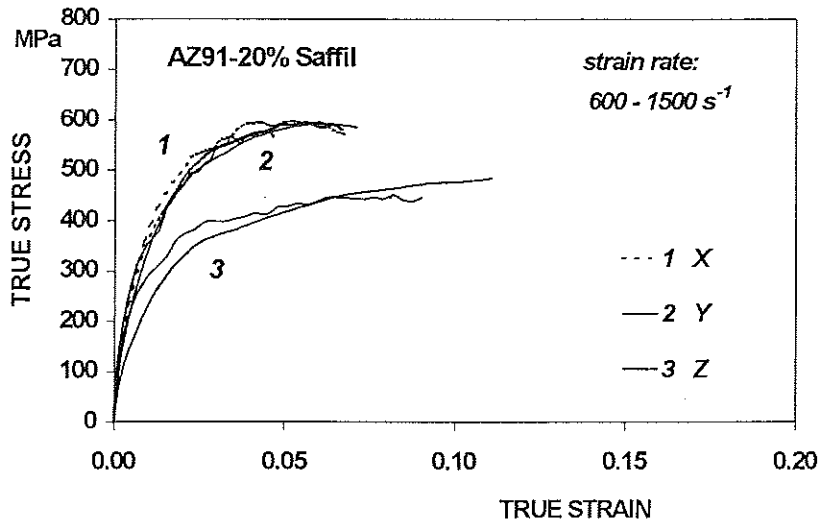


Figure 4: Dynamic compression tests, specimens direction in figure 1.

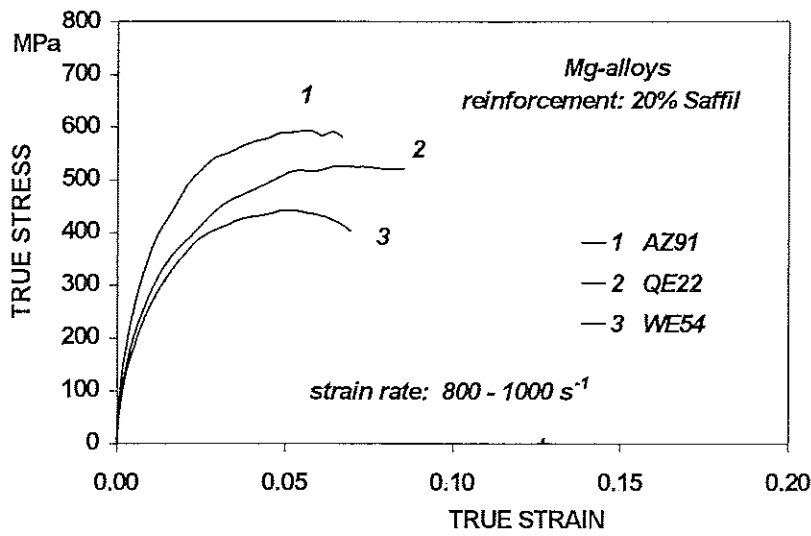


Figure 5: Dynamic compression tests, three matrix alloys

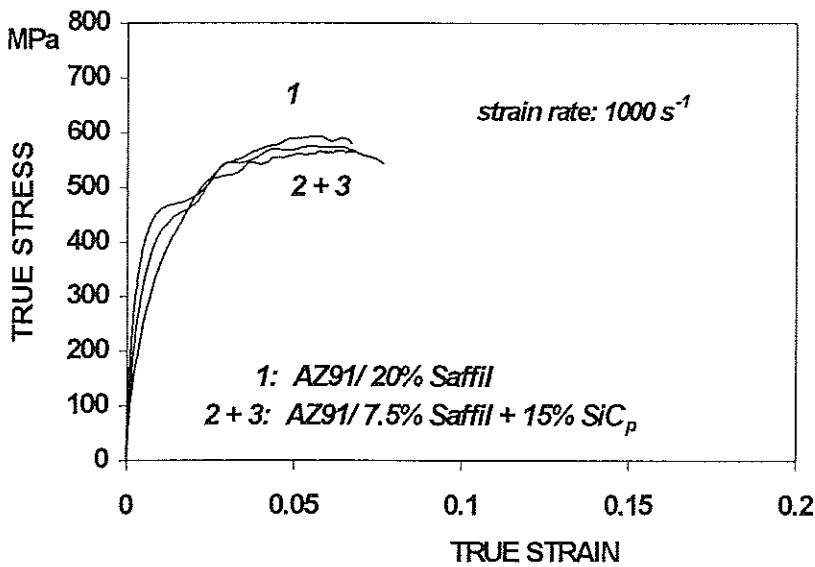


Figure 6: Dynamic compression tests, comparison between short-fiber and mixed reinforcements

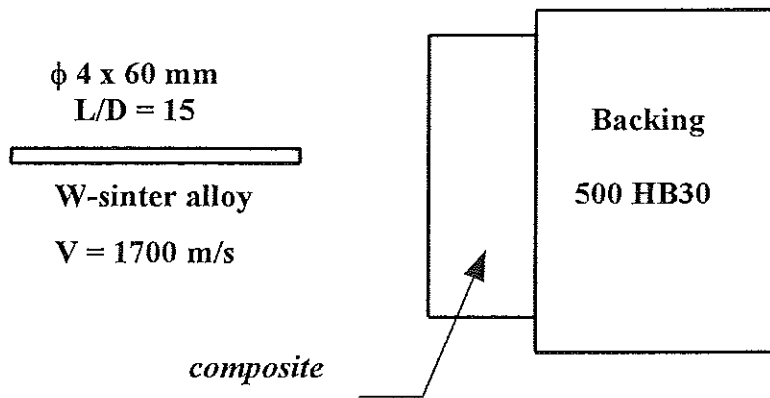


Figure 7: Target configuration for ballistic tests

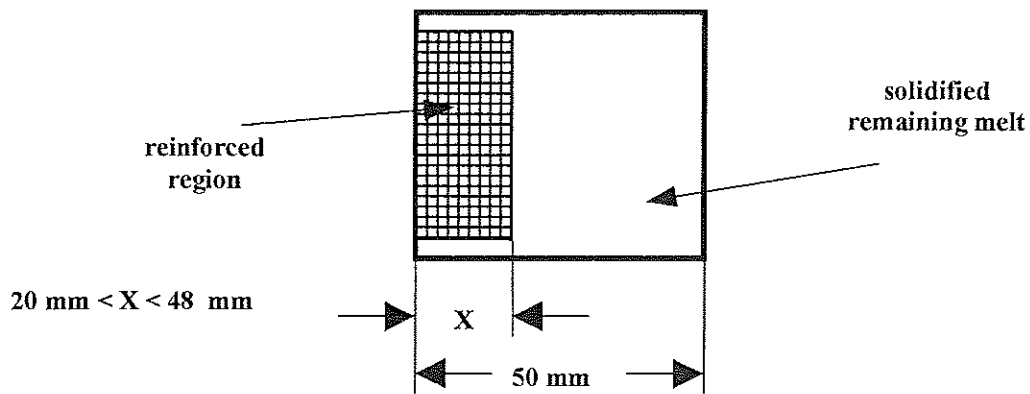


Figure 8: As-cast status of target material

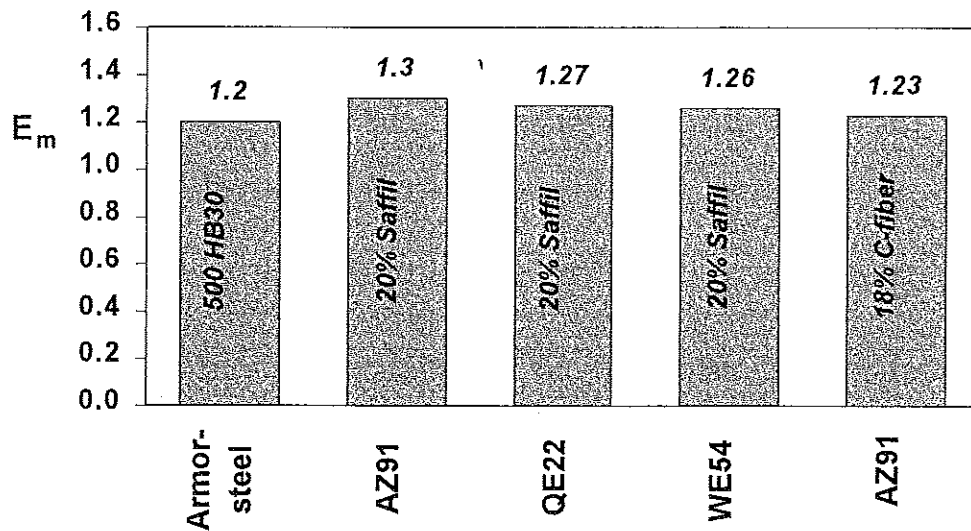


Figure 9: Ballistic results of short-fiber reinforced Mg-alloys

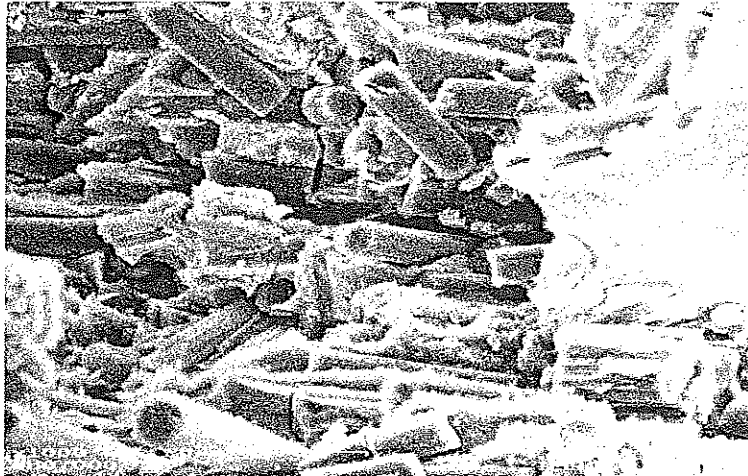


Figure 10: Ballistic test using C-fiber reinforced AZ91, SEM photograph

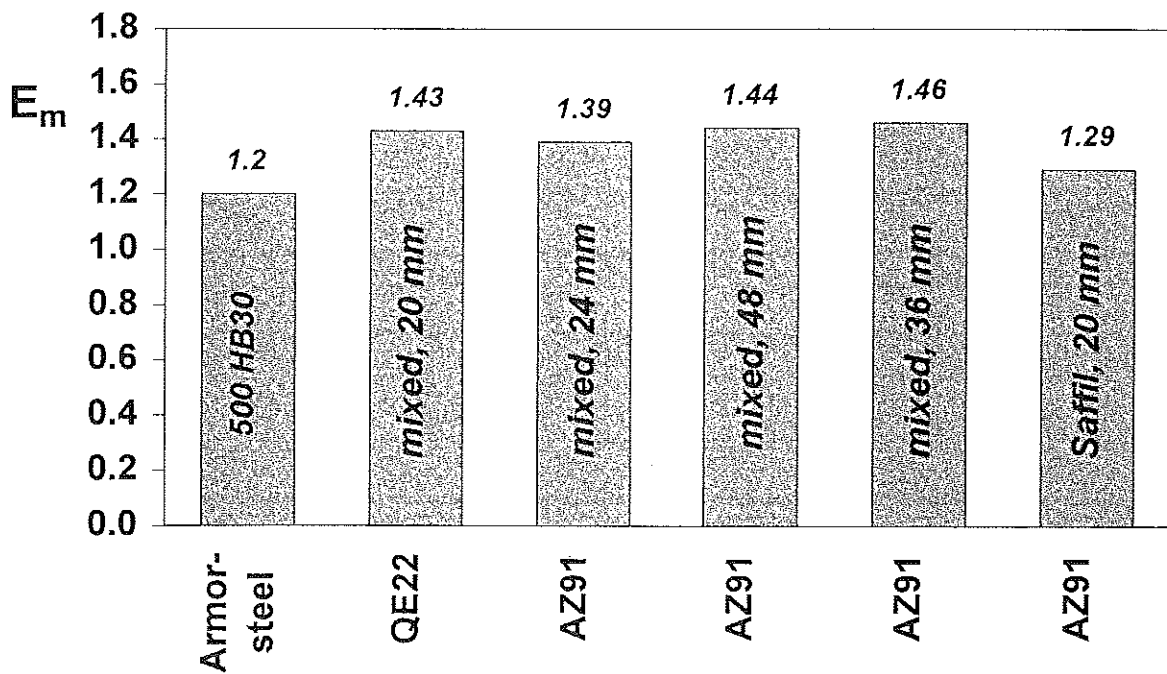


Figure 11: Ballistic results of reinforced Mg-alloys in the as-cast status

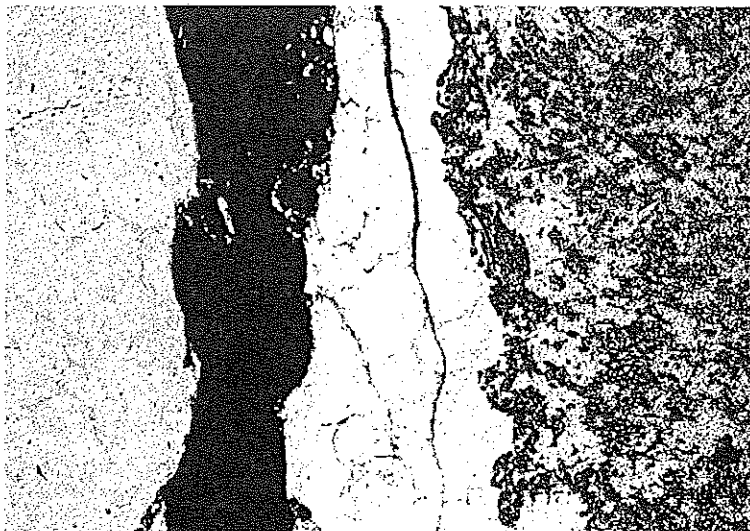


Figure 12: Interface between reinforced Mg-alloy and solidified remaining melt

DYNAMIC BEHAVIOR OF CERAMIC MATRIX COMPOSITES PROCESSED BY DRY PRESSING

E. Barbero, J. Fernández-Sáez and C. Navarro

Department of Mechanical Engineering
Universidad Carlos III de Madrid
Avda de la Universidad, 30. 28911 Leganés (Madrid).
Spain

ABSTRACT

Most of the manufacturing processes of ceramic matrix composites are complex and expensive, so it is necessary to reduce the cost of these methods for the product to be competitive. In this work, both static and dynamic bending tests were carried out on a ceramic matrix composite manufactured by a simple and economical method, similar to that used with monolithic ceramics. Not only the measured mechanical properties obtained are similar to those of commercial materials, but also it is less expensive.

INTRODUCTION

Certain industrial applications require materials with some special properties. For example, for automobile and aerospace applications (Woething, 1996, Beesly, 1997, Levine *et al*, 1987), for the production of engines components or gas turbines, the alternative materials should have a high melting point, excellent thermal stability, good wear resistance and low density. On the other hand, in military armour products (Matchen, 1996), materials are required with high hardness, good compression strength, high erosive capacity and low density (Evans 1996).

Advanced structural ceramics exhibit a combination of properties that make them appropriate candidates for the above applications (Buljan *et al*, 1989), i.e. high strength at elevated temperatures, high hardness, good corrosion and erosion behaviour, high Young modulus, low density, low friction coefficient, high melting point, etc. The main handicap in adopting these materials lies in their reduced ductility and fracture toughness, which makes ceramic components prone to catastrophic failure. This is overcome by the

development of ceramic matrix composites (CMCs) which present considerable enhancement of the measured properties: strength, hardness, Young modulus, thermal shock resistance, etc.

The current use of CMCs in structural applications requires a detailed knowledge of their mechanical behaviour in service. For some applications in which the structural component will be subjected to dynamic or impact forces, a mechanical characterization, static and dynamic, should be carried out.

PROCESSING

The materials were manufactured by a cheap and simple production method: dry pressing followed by sintering (Bortzmeyer, 1995). The procedures of this method are uncomplicated; i.e. the powder mixtures are easy to prepare and require no expensive equipment for the previous handling.

Several special tools were designed for the material manufacture, to produce different specimen geometries for all types of mechanical testing. Fig. 1 shows the bending test specimen die.

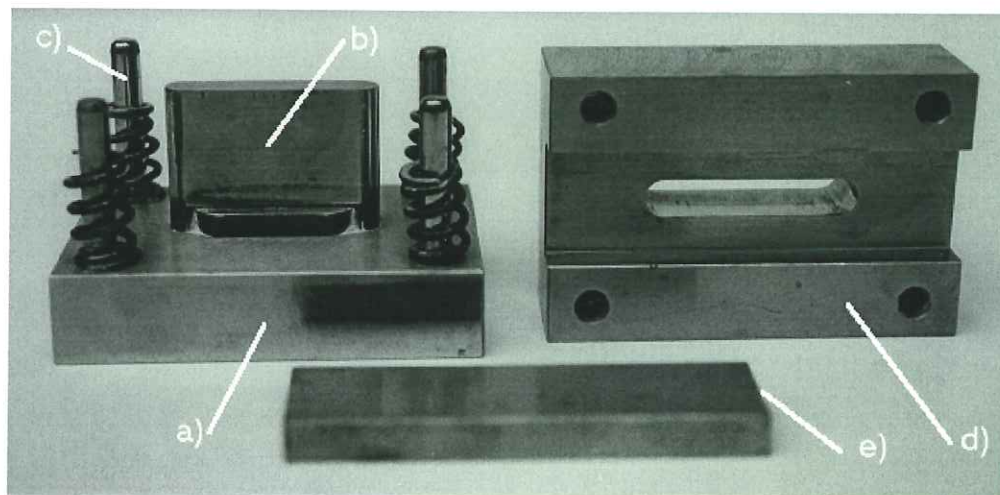


Fig. 1. Floating-die equipment, a) bottom plate, b) punch, c) column and spring (x4), d) die set, e) top plate.

The material was uniaxially pressed at 87 MPa for 120 seconds in a hydraulic press, then sintered at 1650°C for 2 hours in air. The density obtained was 96-98% of the theoretical density (Barbero, 1999).

MATERIAL

The material employed was Alumina powder of 99.7% purity CONDEA APA with 0.5 μm grain size and Zirconia powder, Tosoh 3YB.

Alumina was selected as the matrix for its excellent combination of properties and cost. The type of reinforcement was selected on the basis of the processing method. Using dry pressing the reinforcement should be discontinuous; moreover the sintering in air requires the use of an oxide material.

Three types of materials were manufactured: monolithic Al_2O_3 , and two ceramic matrix composites, Al_2O_3 -15%_w ZrO_2 and Al_2O_3 -30%_w ZrO_2 (Barbero, 1999).

EXPERIMENTAL PROCEDURE

Two types of bending test were performed, static in a universal testing machine, and dynamic in a Charpy pendulum.

Static bending tests were carried out following the ASTM C1161-90 standard using an Instron Universal Test Machine, with 100 kN maximum load. The sample sizes used were: 3x4x45 mm and 10x10x55; the first size following the ASTM standard, the second was selected to compare the results of the test from both, the dynamic and static.

For the static bending test a force-displacement curve was obtained for each sample, as is shown in Fig. 2.a. By means of this test the bending strength was calculated, as well as an estimation of the Young modulus. Because of the great dispersion of the advanced ceramic test results, a total of 15 specimen of each composite material and 30 of the monolithic material were tested.

Dynamic bending tests were carried out in a 300 J Charpy pendulum CEAST using a combination of ASTM C1161-90 and ASTM E23-86 standard (referring to dynamic tests in Charpy pendulum on metallic materials). The specimens measured 10x10x55 mm,

following the ASTM E23-86 standard. The applied impact velocity was 0.47 m/s which corresponds to a total pendulum energy of 2.2 J.

For the dynamic bending test, a force-time curve was obtained for each sample, as is shown in Fig. 2.b.

By means of successive integrations, both the displacement and the absorbed energy could be estimated. In this way the dynamic bending strength, the resilience and an estimation of the Young modulus were calculated for all materials.

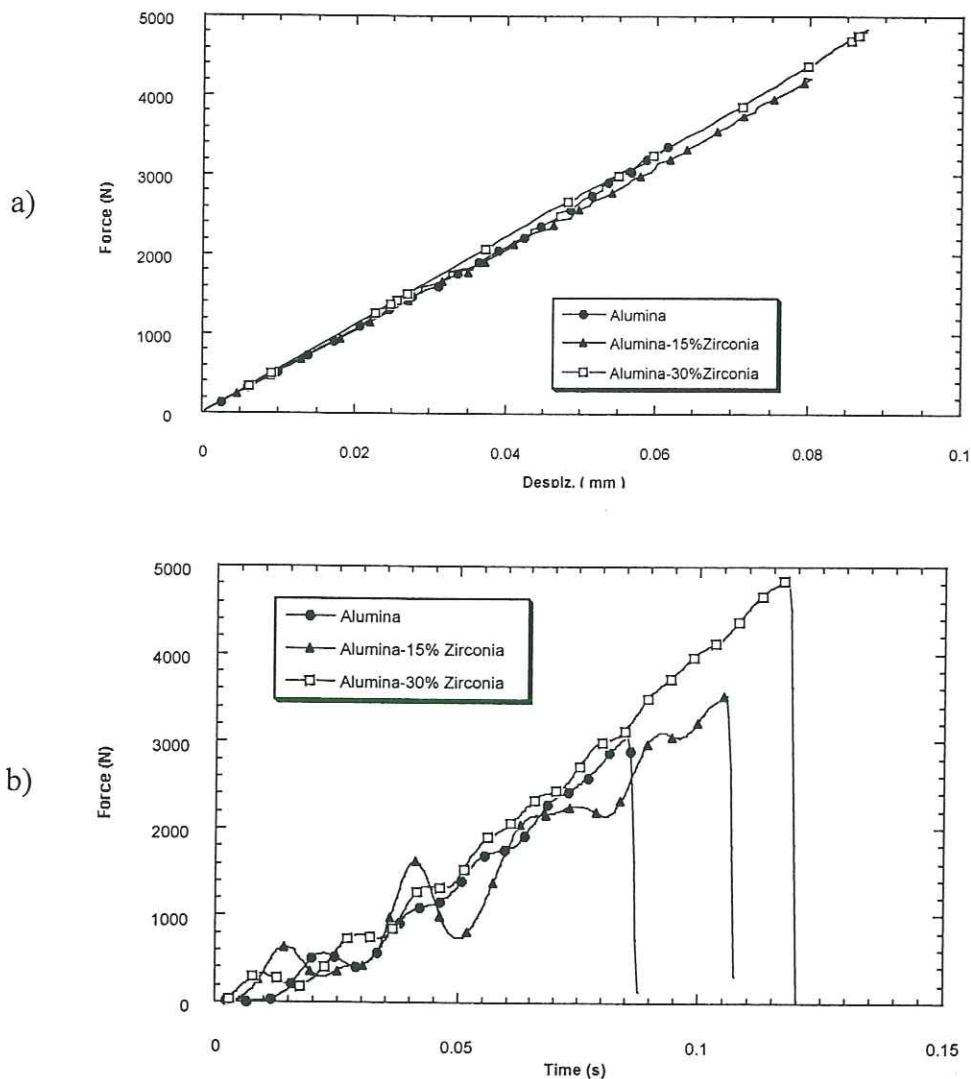


Figure 2. Curves obtained from bending test, a) Curves force-displacement, bending static test, b) Curves force-time, bending dynamic test.

RESULTS

The results obtained from the static test for monolithic alumina are: 289 ± 41 MPa bending strength, 272 ± 19 GPa Young Modulus and 9.15 Weibull modulus.

In this case the static bending strength values obtained for Al_2O_3 -30%_{wf} ZrO_2 composite are 50% higher than that obtained for monolithic alumina, as is shown in Fig. 3a. For the Young modulus, the increment is 35% for the same material.

In the dynamic test an increase of 57% in the bending strength values, as is shown in Fig.3.b., and 94% in the resilience was achieved for the Al_2O_3 -30%_{wf} ZrO_2 composite.

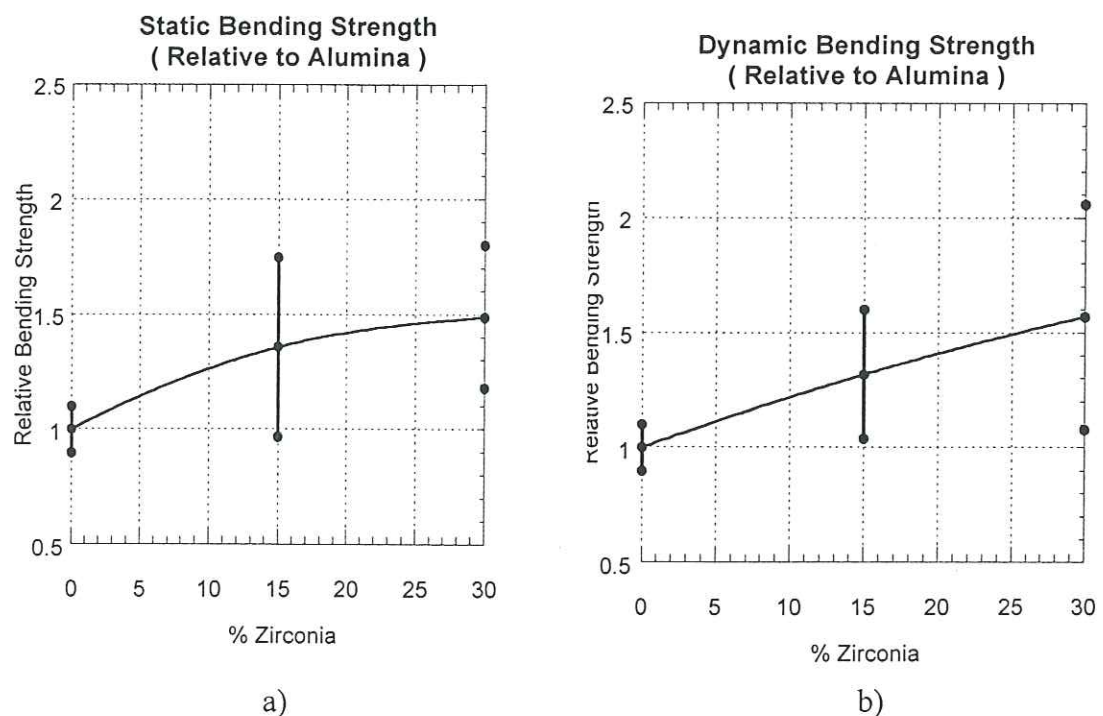


Figure 3. Bending Strength, a) static and b) dynamic.

CONCLUSIONS

- A simple and economical method of processing ceramic matrix composites was developed. It provides a material with good mechanical properties similar to those of commercial material produced with more complex and costly methods.
- A zirconia-toughened alumina was fabricated by the addition of zirconia particles to alumina, which improves the static and dynamic strength, and in particular the ductility.

ACKNOWLEDGEMENT

The authors are indebted to the Fundación Ramón Areces (Área de Materiales, IX Concurso Nacional, Proyecto: "Desarrollo y caracterización macro y micromecánica de nuevos materiales compuestos de matriz cerámica y refuerzo cerámico) for the financial support of this research.

REFERENCES

- Barbero, E., Desarrollo y caracterización mecánica de nuevos materiales compuestos de matriz cerámica y refuerzo cerámico. PhD Thesis, University Carlos III of Madrid, 1999 (in Spanish)
- Bauccio, M.L., (1994) "Ceramic matrix composites", *Engineered Materials Reference Book*, ed. ASM International, 163-179.
- Beesley, C.P., (1997) "The application of CMCs in high integrity gas turbine engines", *Key Engineering Materials*, **127-131**, ed. Trans Tech Publications, 165-174.
- Bortzmeyer, D., (1995) "Dry pressing of ceramic powder", *Ceramic processing*, editor: Terpstra, R.A., Pex, P.P.A.C. y de Vries, A.H., ed. Chapman and Hall.
- Buljan, S.T., Pasto, A. E. y Kim, H. J., (1989) "Ceramic whiskers- and particulate-composites: Properties, reliability, and applications", *Ceramic Bulletin*, **68**, (2), 387-394.
- Evans, K.A., (1996) "The manufacture of alumina and its use in ceramic and related applications", *Key Engineering Materials*, **122-124**, editor: Trans Tech Publications, 489-526.
- Levine, S.R., Herbell, T.P., (1987) "Aerospace Applications", *Engineered Materials Handbook. Ceramic and Glasses*, **4**, ed. ASM International, 1004-1005.
- Matchen, B., (1996) "Applications of ceramics in armor products", *Key Engineering Materials*, **122-124**, ed. Trans Tech Publications, 333-342.
- Seidel, J., Claussen, N. y Rödel, J., (1995) "Reliability of Alumina Ceramics: Effect of Grain Size", *Journal of European Ceramic Society*, **15**, 395-404.
- Woetting, G., Lindner, H.A. y Gugel, E., (1996) "Silicon nitride valves for automotive engines", *Key Engineering Materials*, **122-124**, ed. Trans Tech Publications, 283-292.

Mechanical Behavior of SiC Particulate-Reinforced Magnesium ZM-51 Composite under Impact Loading and High Temperature

Essa, Y. E. and Pérez Castellanos, J. L.

Department of Mechanical Engineering, University of Carlos III, 28911 Leganés, Madrid, Spain

ABSTRACT

This work focuses on investigating the effect of temperature and heating time on the mechanical properties of composite materials under high strain rates. The compressive strength of the SiC particulate reinforced composites and matrix metal of magnesium base alloy under high strain rates up to $1.5 \cdot 10^3 \text{ s}^{-1}$ at elevated temperature and different heating times, have been studied. Dynamic compression diagrams and strain-rate histories were obtained for all the materials. The results show that for SiC particulate reinforced composites and the matrix magnesium alloy, a considerable increase in compressive strength, upper yield stress and ductility between 100 and 200°C during 10 and 120 minutes of heating, were observed.

INTRODUCTION

Metal matrix composites (MMCs) are now emerging as an important class of materials in recent years. They have been developed for use in demanding environments, which require higher specific mechanical properties and durability at elevated temperatures (Hadianfard et al., 1994 and Sarkar et al., 1993) and high strain rate. The reinforcement of lightweight alloys with ceramic particles provides a material with high specific stiffness, which is suitable for advanced engineering applications, such as in the automotive and aerospace fields (Wei, 1992). These applications require materials which are dimensionally stable and maintain their mechanical behavior when used at elevated temperatures. In a number of studies (e.g. Miguélez and Navarro, 1998 and Burgahn et al., 1992), it has been noted that flow stress values and the rate of strain hardening of several MMCs (aluminum base alloys,...) are sensitive to the imposed strain rate and the test temperature.

Particle reinforced magnesium alloys are interesting materials for technological applications because they exhibit higher stiffness, smaller thermal expansion and wear resistance than conventional magnesium alloys. They possess some attractive mechanical properties, both at room and elevated temperatures (Köhler et al., 1993 and Mikucki et al., 1986).

The SHPB (Split Hopkinson Pressure Bar) is a standard experimental technique

nowadays for performing tests under dynamic loading. The technique finds its origin in the work of Hopkinson (1914) who used it to measure a pressure-pulse profile using a long thin bar and it has been well established since the critical study made by Davies (1948). During the SHPB test a cylindrical specimen is compressed axially between two instrumented, coaxial bars. Strain gauges mounted on the incident and transmitter bars enable the stress waves to be measured.

The aim of the present work is to determine whether there are significant differences in the material behavior when a magnesium alloy and reinforced samples are tested under different temperatures and times of exposure.

EXPERIMENTAL PROCEDURE

Split Hopkinson Pressure Bar (SHPB) technique is a well-established method for determining the dynamic mechanical properties of solids at high strain rates. The apparatus consists principally of a striker and two Hopkinson pressure bars mounted and aligned on a rigid base. A schematic of the basic SHPB is shown in Fig.1. The used pressure bars are made from 22.0-mm diameter and 1.0 m Inconel alloy rod. The 33.0-mm long striker was accelerated in an air gun.

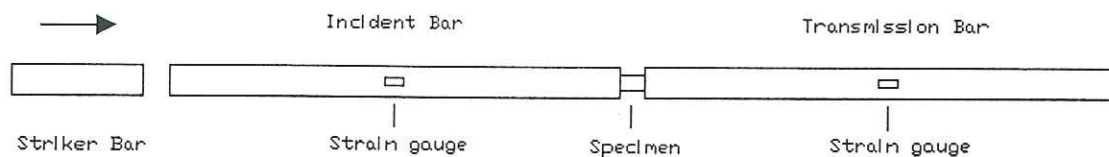


Fig.1 Schematic of the split Hopkinson pressure bar system

In the present investigation, two commercially casting alloys of MELRAM composite of ZM-51 were employed. The chemical composition of this alloy is given in Table 1. The used reinforced material consisted of a magnesium matrix alloy and 12% vol. 10 μm of silicon carbide (SiC) particulate reinforced composite.

Alloying element	Zn	Mn	Mg
%	4.0-5.0	0.5-1.0	Balance

Table 1. Chemical composition of the employed alloy

Uniaxial compression test was performed on cylindrical specimens. They were cut from extruded rods. Specimen dimensions were 13.5 mm in diameter and 7.0 mm in length. The test temperatures were room temperature (RT), 100 and 200°C for 10 and 120 minutes. The cause of selecting the temperature of 200°C is due to the maximum testing temperature is 250°C (Kiehn et al., 1997). They were tested under the same strain rate of to $1.0 \cdot 10^3 \text{ s}^{-1}$. The reinforced materials were also tested under $1.5 \cdot 10^3 \text{ s}^{-1}$ to study the effect of high strain rate. The interface bar-specimen was lubricated with the lubricant MOLYPAUL 516, which has high performance at the test temperatures. The aim of its use is to reduce the friction effect between the specimen and the two bars.

RESULTS AND DISCUSSION

All the materials were tested under ambient, different temperatures and heating times. To take into consideration the experimental scatter, 3 or 4 tests were conducted under each set of nominally similar conditions. Dynamic stress-strain diagrams and strain rate histories were obtained.

True stress-true strain curves were derived from each test and a corresponding flow stress determined. Fig.2 shows the dynamic stress-strain diagrams for ZM-51 material at different temperatures and heating times. Their effect on the upper yield stress is nearly negligible. It is found that the major differences are between the two curves of room temperature and the highest time and temperature of exposure. The ductility is improved by 26% although the maximum strength is decreased (28%) compared with ambient test condition. There is a decrease in the maximum strength for the same temperature of 200°C by 17% and for 100°C by 8% from 10 to 120 minutes. Also there is an increase in the ductility for the same temperature of 200°C by 9% and of 100°C by 11% for the time difference between 10 to 120 minutes.

Fig.3 shows the flow-curves of true stress-true strain in compression for the material of ZM-51/12%SiC at strain rate of $1.0 \cdot 10^3 \text{ s}^{-1}$, which is the same like ZM-51 material tests. At highest temperature and time of exposure, the ductility is increased by 30% although the maximum strength is decreased by 18% compared with ambient test condition. The decrease of the maximum strength for the same temperature (200°C or 100°C) from 10 to 120 minutes, is less than the case of ZM-51 alloy. Also the difference in the ductility is more than that of the base alloy. There is an increase in the ductility of 200°C by 12% and for 100°C by 8% from 10 to 120 minutes.

Fig.4 demonstrates the true stress-true strain in compression for the reinforced material of ZM-51/12%SiC under higher strain rate of $1.5 \cdot 10^3 \text{ s}^{-1}$. At highest temperature and time of exposure tests of 200°C and 120 minutes, the ductility is increased by 43% although the maximum strength is decreased by 16% compared with the ambient test condition. There is a decrease in the maximum strength for the same temperature (200°C or 100°C) from 10 to 120 minutes. This is the same behavior which was happened when tested under the previous case of Fig.3. The increase in the ductility is more than the same material or the base alloy when tested at $1.0 \cdot 10^3 \text{ s}^{-1}$ for the same temperature and heating time conditions.

CONCLUSION

The results obtained show that the stress-strain diagrams for two materials of magnesium base alloy, ZM-51 and ZM-51/12%SiC, are sensitive to temperature, heating time and strain rate dependent. At room temperature the maximum strength exhibited only a fairly weak dependence on strain rate.

Significant increase in compressive yield strength and compressive maximum strength of reinforced material are obtained relative to unreinforced magnesium alloys; unfortunately, the ductility of the composite materials is reduced.

ACKNOWLEDGEMENT

The authors are indebted to CICYT for their financial support to this research under grant No. MAT96-0649.

REFERENCES

- Burgahn, F., Vöhringer, O. and Macherauch, E., 1992, "Modelling of Flow in Steels as a Function of Strain Rate and Temperature," Shock-Wave and High-Strain-Rate Phenomena in Materials (ed. Meyers, M., Murr, L. and Staudhammer, K.), Marcel Dekker, New York.
- Davies, R. M., 1947, "A Critical Study of the Hopkinson Pressure Bar," Philosophical Transactions of the Royal Society of London A, Vol. 240, pp. 375-457.
- Hadianfard, M. J., Healy, J. and Mai, Y., 1994, "Temperature Effect on Fracture Behaviour of an Alumina Particulate-Reinforced 6061-Aluminium Composite," Applied Composite Materials, Vol. 1, pp. 93-113.
- Hopkinson, B., 1914, "A Method of measuring the Pressure Produced in the Detonation of

Explosives or by the Impact of Bullets,” *Phil. Trans. R. Soc.*, A213, pp. 437-456.

Kiehn, J., Bohm, E. and Kainer, K.U., 1997, “Deformation of Continuous Carbon Fibre Reinforced Mg-Alloys by Thermally Induced Stresses,” *Key Engineering Materials*, Vol. 127-128, 861-868.

Köhler, C. and Kainer, K. U., 1993, “Thermal Exposure Effects on the Structure and Mechanical Properties of Short-Fibre Reinforced Magnesium Alloy,” *Proceedings of the Ninth International Conference on Composite Materials (ICCM/9)*, Madrid, July12-16, pp. 347-354.

Miguélez, H. and Navarro, C., 1998, “Dynamic Behaviour of Aluminium-Based Composite Materials at High Temperature,” *Proceedings of the Fifth International Conference on Composites Engineering (ICCE/5)*, Las Vegas, Nevada, July 5-11, pp. 651-652.

Mikucki, B. A, Shook, S. O., Mercer, W. E. and Green, W. G., 1986, “Magnesium Matrix Composites at Dow: Status Update,” *Proceedings of the 43rd Annual World Magnesium Conference*, International Magnesium Association, pp. 13-23.

Wei, W., 1992, “High Temperature MMCs for Aero-Engines: Challenge and Potential,” *Metals and Materials*, Vol. 8, pp. 430-435.

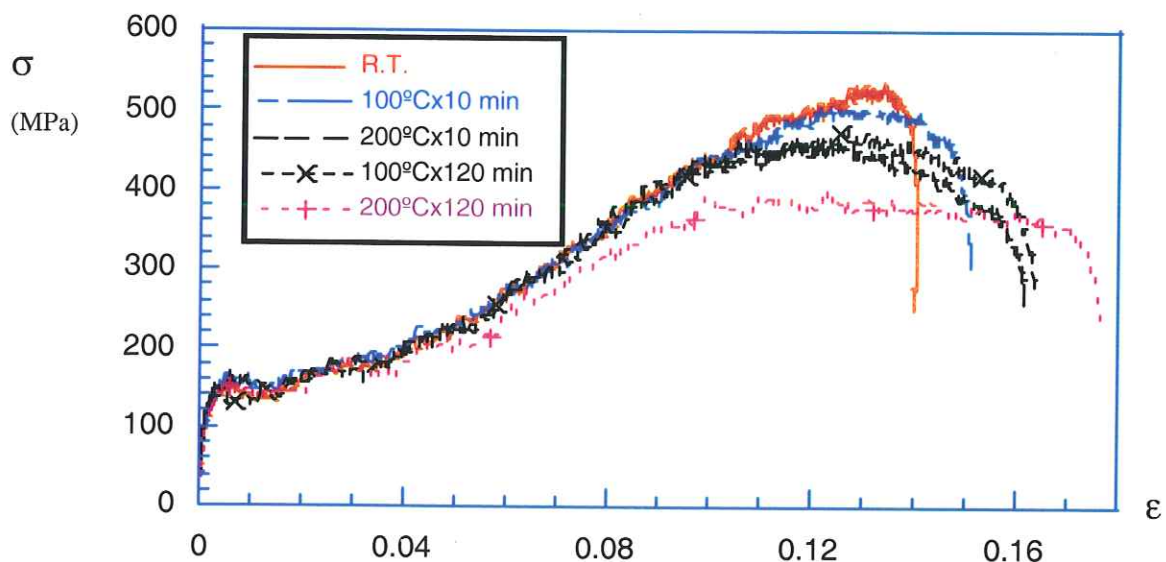


Fig. 2 Effect of test temperature and heating time on flow properties of ZM-51 material at a strain rate = $1.0 \cdot 10^3 \text{ s}^{-1}$

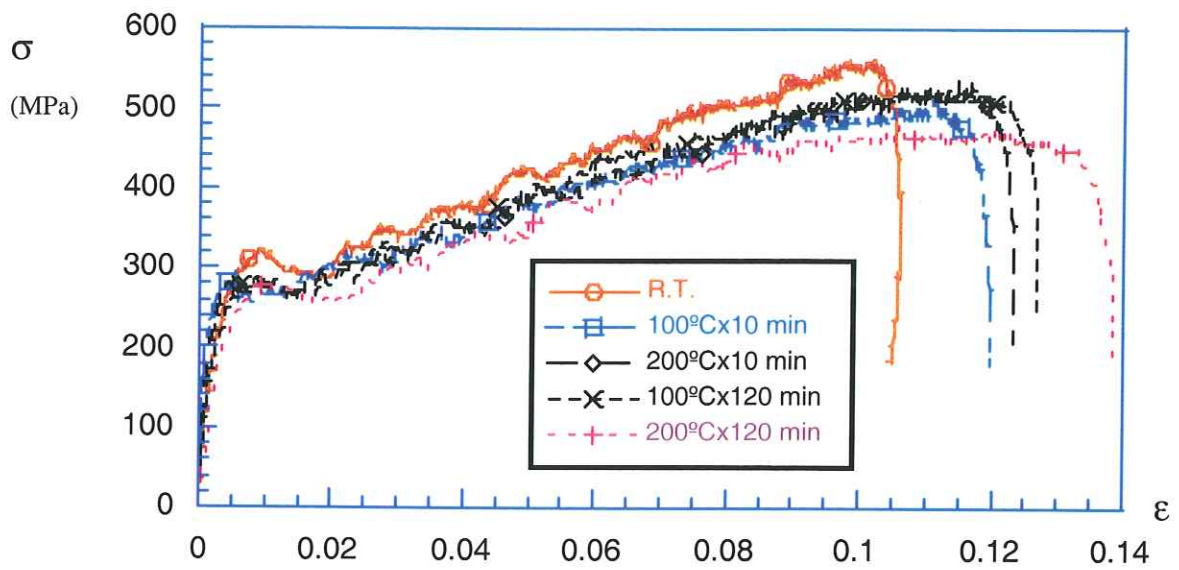


Fig. 3 Effect of test temperature and heating time on flow properties of ZM-51/12%SiC material at a strain rate = $1.0 \cdot 10^3 \text{ s}^{-1}$

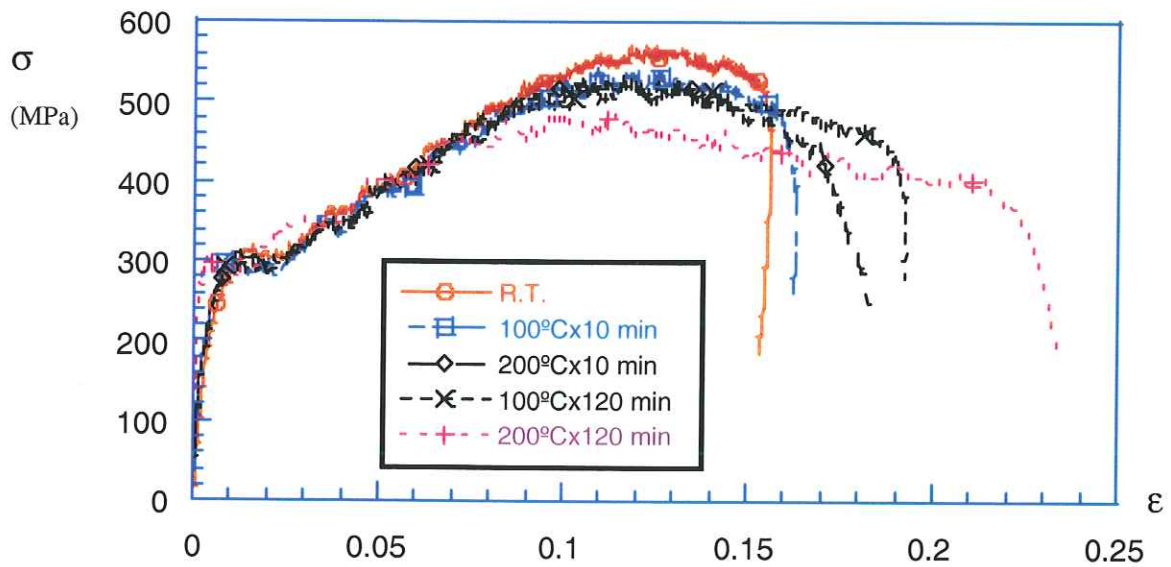


Fig. 4 Effect of test temperature and heating time on flow properties of ZM-51/12%SiC material at a strain rate = $1.5 \cdot 10^3 \text{ s}^{-1}$

DYNAMIC BEHAVIOUR OF CARBON FIBER REINFORCED COMPOSITES AT INTERMEDIATE STRAIN RATES AND LOW TEMPERATURE.

R. Zaera and C. Navarro

Department of Mechanical Engineering, Universidad Carlos III de Madrid,
Avda. de la Universidad 30, 28911 Leganés, Madrid, Spain.
Tfn: 34-91-6249491, Fax: 34-91-6249430. E-mail address: navarro@ing.uc3m.es

ABSTRACT: *This work examines the mechanical behavior, at different strain rates and temperatures, of carbon fiber reinforced polymeric matrix composites. Three point bending tests were carried out in static (at 20 C) as well as in dynamic conditions (at 20 C and -70 C). Several variables were analyzed: strain rate on the specimen, failure mode, applied force history and absorbed energy before first damage. The experimental results showed a correlation between the impact speed and absorbed energy before first damage. Different failure modes were observed at different temperatures. A sudden drop in the strain rate was detected at the beginning of the load stage.*

1. INTRODUCTION

The use of carbon fiber reinforced polymers (CFRP's) has escalated in a wide range of technological applications. In many of their engineering applications, these materials could be subjected to impact loads at low temperature [1]. Unfortunately, the mechanical behavior of CFRP's at low speed impact is not yet well known ([2], [3], [4]), with the added difficulty of the non-existence of standards to help the engineer to design structures with these materials. To further the knowledge of their mechanical properties, three point bending tests were carried out, in both static and dynamic conditions. The tests showed the effect of strain rate and temperature on the mechanical behaviour of the material.

2. MATERIAL DESCRIPTION AND SPECIMEN GEOMETRY.

The material used was carbon fiber reinforced epoxy resin (AS4/8552) with a 58 % fiber content. The laminate was of 22 layers of 0.18 mm thickness, its stacking sequence being $[\pm 45, 0, 90, 0, \pm 45, 0, 90, \pm 45]_s$. Its compressive strength was 640 MPa. The specimens were rectangular (50x15x4 mm) and the span length was 37 mm.

3. EXPERIMENTAL TESTING

3.1 Static conditions:

An INSTRON 8516 universal testing machine with a 5 kN load cell was used. The load application speed was 0.01 m/s. A typical force-displacement curve of the test is sketched in Figure 1. The behaviour is linear elastic until first damage, and the energy absorbed by the specimen at this point, E_{th} , can be easily calculated.

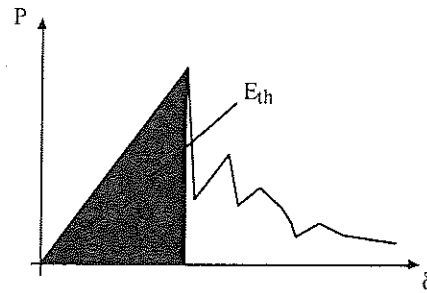


Fig 1. Characteristic force-displacement curve.

3.2 Dynamic conditions

A FRACTOVIS 6785 drop weight test device was used. It has a climatic chamber that can be cooled down to -70 C with liquid nitrogen (Figure 2). An instrumented impactor registered the applied force. The impact velocities were between 1.5 m/s and 2 m/s, and two temperatures (20 C and -70 C) were used. The force-displacement curve obtained in these tests was similar to that in Figure 2, and also E_{th} can be calculated. The maximum strain rate on the specimen could be estimated by:

$$\dot{\varepsilon} = \frac{6c}{d^2} \dot{\delta}$$

where c is the specimen thickness, d is the span length, and $\dot{\delta}$ the velocity at the impactor tip.

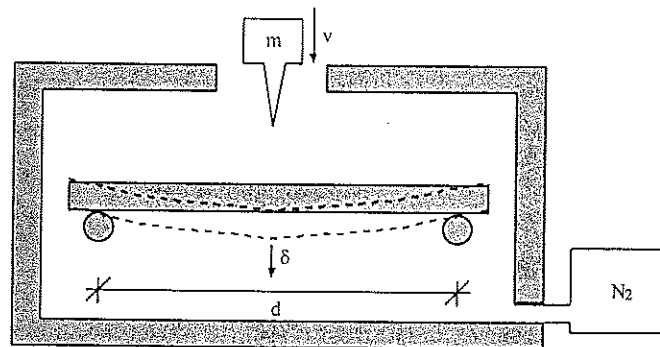


Fig 2. Sketch of the drop weight test device.

4. EXPERIMENTAL RESULTS

4.1 Static conditions:

An energy E_{th} between 2.6 J and 4.2 J was obtained in this set of test. Figure 3 shows the force-displacement curves for these limit cases.

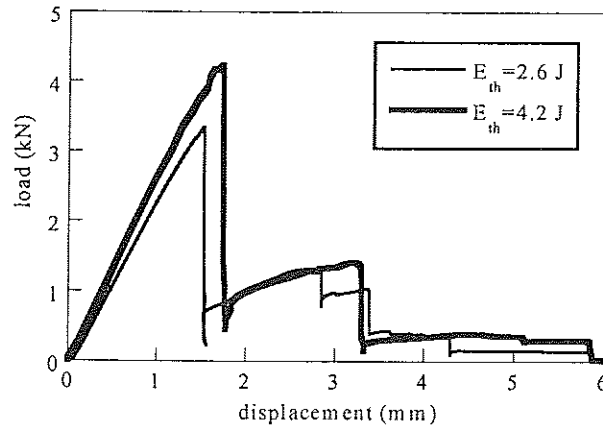


Fig 3. Force-displacement curves in static conditions and at room temperature.

A illustration of a damaged specimen appears in Figure 4, with the characteristic failure by bending of this type of material.

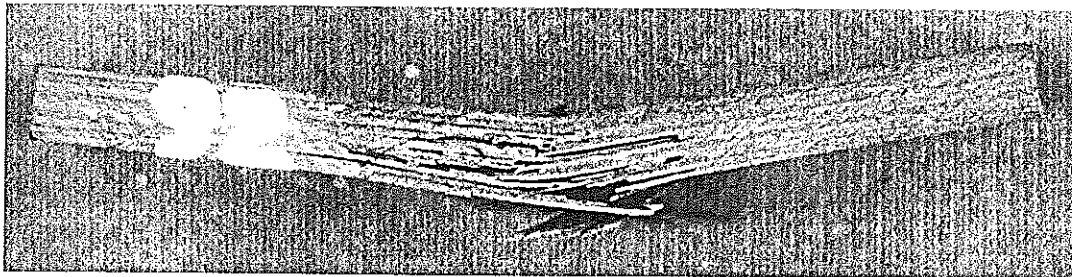


Fig 4. Specimen tested in static conditions at room temperature.

4.2 Dynamic conditions

The impact energy varied between 4 J ($v=1.5$ m/s) and 7.2 J ($v=2$ m/s). Figure 5 shows the force-displacement curves for two 4 J impact energy impacts, at 20 C and -70 C. The energy E_{th} calculated in each case was 2.6 J and 2.4 J respectively, showing the correlation between temperature and energy absorbed by the material until first damage. At the lower temperature, the material behaviour is weaker than at room temperature. Similar conclusion were obtained at higher impact energies.

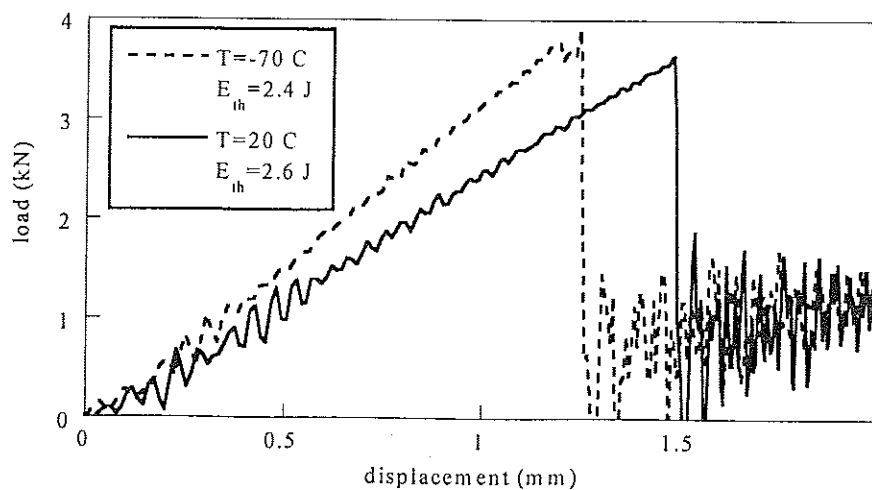


Fig 5. Force-displacement curves in dynamic conditions (4 J) at different temperatures.

This is confirmed on comparing the failure modes and the strains reached in the specimens at different temperatures. Figure 6 shows specimens tested at 20 C and -70 C. The damage increases as temperature decreases, showing much greater fragility at -70 C. Table 1 reports the range of maximum strains in the central section before first damage, and shows that the lower temperature gives lower deformations.

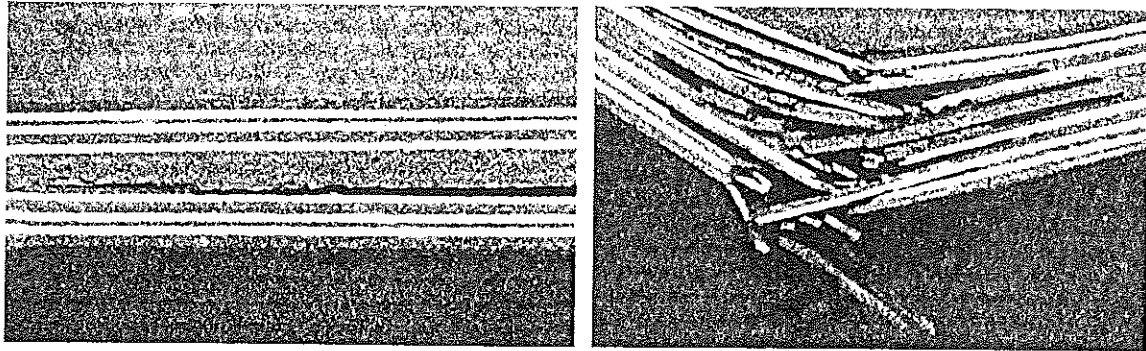


Fig 6. Specimens tested at 20 C (left) and at -70 C (right). Impact energy: 4 J.

Temperature (C)	ϵ_{\max} range (%)
20	2.1 - 2.6
-70	1.9 - 2.3

Table 1. Influence of temperature on maximum strain before first damage. Impact energy: 4 J.

Tests in static conditions (Figure 7) require more energy to produce first damage than is required in dynamic testing. However, in dynamic tests, as the impact is increased, more energy is required to damage the material, which means a rise in ductility with the impact energy. In static conditions, the damage deformation of the material is between 2.7 % and 3.2 % (Table 2), while this deformation increases as the velocity is increased.

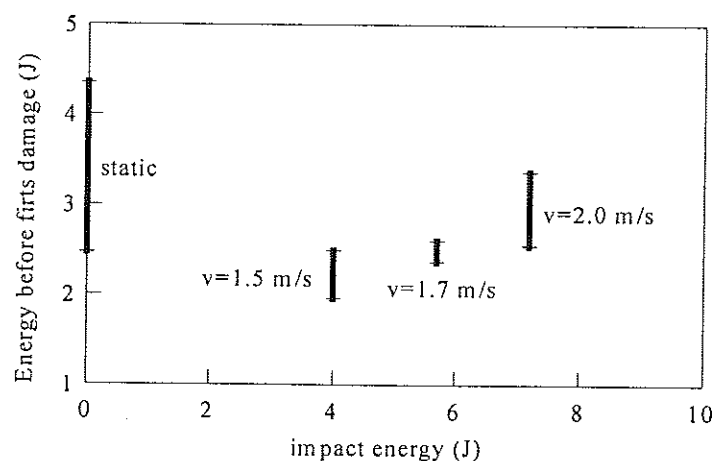


Fig 7. Influence of impact energy on E_{th} . Temperature=20 C.

Impact energy (J)	Impact velocity (m/s)	ϵ_{\max} (%)
≈ 0	10^{-5}	2.7 – 3.2
4.0	1.5	2.1 – 2.6
5.5	1.7	2.5 – 2.7
7.2	2.0	2.8 – 3.0

Table 2. Influence of the impact energy on the maximum strain on the specimen. Temperature: 20 C.

Specimens impacted at room temperature but higher impact loads (5.5 J and 7.2 J) are shown in Figure 8. Together with Figure 4, they show the change in the type of damage as the impact energy is increased.

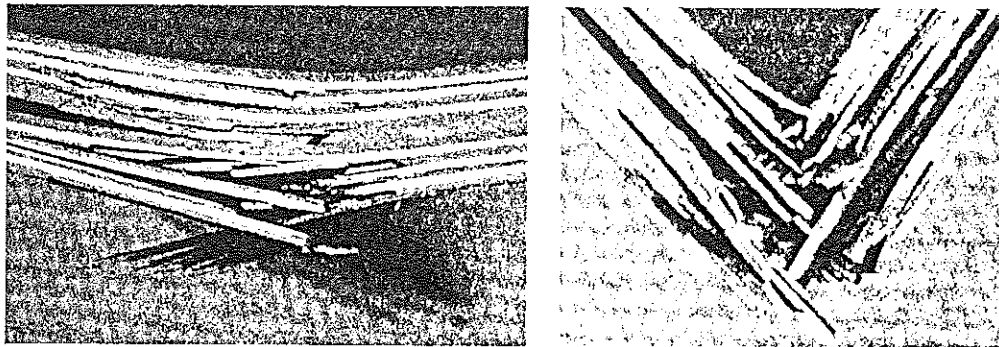


Fig 8. Effect of impact energy on damage after impact. $E=5.5$ J (left), $E=7.2$ J (right). Temperature=20 C.

Figure 9 (a test at room temperature and 5.5 J impact energy) illustrates the fall in the strain rate as the test proceeds. It shows in particular that in the initial stage of loading, before the first damage of the material, the strain rate presents a drop, which means that the results are not those of a single value E .

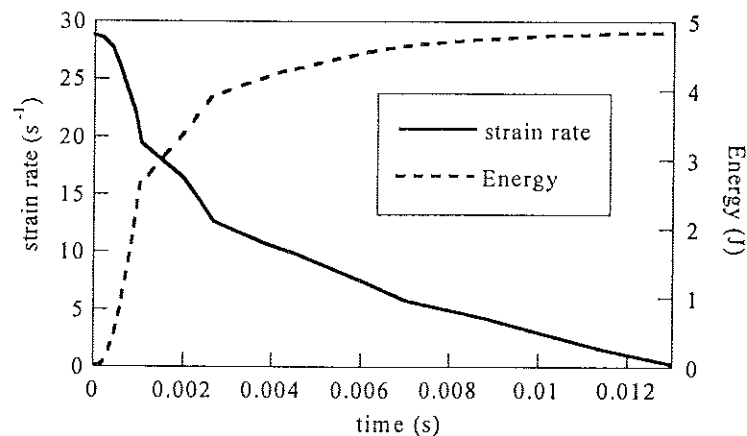


Fig 9. Strain rate and energy history. Temperature=20 C. Impact energy=5.5 J.

5. CONCLUSIONS

The conclusions to be drawn from the above results are as follows:

- The energy required to produce the first damage appears to depend slightly on the impact energy.
- At an identical impact energy, the mode of rupture of the material at low temperature is different from that at room temperature.
- The strain rate falls during the initial stage of loading.

6. ACKNOWLEDGMENTS

The authors are indebted to A. Güemes and J. M. Pintado for the material fabrication and to the Dirección General de Enseñanza Superior for the financial support of this work (Project PB94-0380).

7. REFERENCES

- [1] C. Navarro, Simplified modelling of the ballistic behaviour of fabrics and fibre reinforced polymeric matrix composites, Impact response and dynamic failure of composites and laminate materials, Trans. Tech. Publications Ltd., (1997).
- [2] J. Cantwell and J. Morton, The impact resistance of composite materials, Composites, Vol. 22, No 5, (1991).
- [3] S. Abrate, Impact on laminated composite materials, Appl. Mech. Rev., Vol 44, (1991).
- [4] Zukas, Impact Dynamics, Ed. John Wiley & Sons, (1982).

BEHAVIOR OF Al/ 19% Al₂O₃ and Al/ 10 % Al₂O₃ COMPOSITE MATERIALS AFTER DYNAMIC LOADING AND SLOW COMPRESSION

S. Coniglione and C. Patuelli

Dipartimento di Fisica ed Istituto Nazionale di Fisica della Materia , Universita' di Bologna,
Viale Berti Pichat 6/2 - 40127 Bologna -Italy
phone : 051 209 5148 fax : 051 209 5153
E-mail : patuelli@df.unibo.it

ABSTRACT

Scanning Electron Microscopy (SEM) , Atomic Force Microscopy (AFM) and Optical Microscopy (OM) observations were carried out in order to investigate the deformation mechanisms of shock- loaded aluminium matrix composites reinforced with fibers (19% volume fractions) and particles (10% volume fractions) of Al₂ O₃. The results are discussed taking into account the role played by the Al/ Al₂ O₃ matrix- reinforcement interface and by the powerful deviatoric shear stresses near the shock wave front as hypothesized by Meyers (1). After dynamic loading the composite reinforced with a mixture of fibers and particles of alumina showed a random, non oriented distribution of Al₂ O₃ fractured fibers as a consequence of the high peak loads which activated not otherwise effective (2) dislocation sources.

INTRODUCTION

In previous papers (3,4,) aluminium matrix composites reinforced with SiC whiskers, Al₂ O₃ fibers and particles were investigated by XRD Fourier analysis after dynamic loading and, for comparison, slow compression.

It was found that the dynamic-loaded composite reinforced with SiC whiskers or with a mixture of Al₂ O₃ fibers and particles showed an increase of the crystallite sizes along different lattice planes (111,200,220) with small, negligible variations of lattice distortions associated to an overall uniformly distributed dislocation density.

The aim of this paper is to better understand the deformation mechanism in composite materials after fast deformation, with special focus on the behavior of metal-ceramic interface and reinforcement.

EXPERIMENTAL

The material used was a metal-matrix composite (MMC) obtained by aluminium alloy (A 356) infiltration into a ceramic preform manufactured by S.I.R with proprietary technology (5). The infiltration was performed with gas pressure equipment (Pcast mod875L) under the following conditions : melt temperature 953 K, preform temperature 848 K , vacuum before infiltration 0.13 Mpa , gas pressure during infiltration 8.27 MPa. Figs 2,3 show SEM images of the preforms and optical micrographs of infiltrated composites. The dynamic loading was obtained by an explosively accelerated flying plate which compressed cubic samples (side 5×10^{-3} m) against a quasi -rigid boundary. For the type of the explosive used calculations indicated peak loads of 0.5-1.5 GPa (6). An average compression rate of 1.5×10^{-2} m/s was used for slow conventional deformation. Microhardness tests were carried out with a REMET microdurometer applying a load of 15 gf on a Vickers' indenter.

RESULTS AND DISCUSSIONS

Table 1 reports the macroscopic parameters after slow and fast deformation of the two composite materials:

Al/19% Al₂O₃:

deformability ($\Delta L/L$)	dynamic loading: 85%	slow compression: 77%
hardness Hv (kg/mm^2):	100 \pm 2	117 \pm 3

Al/ 10% Al₂O₃:

deformability ($\Delta L/L$)	dynamic loading: 82%	slow compression: 75%
hardness Hv (kg/mm^2):	116 \pm 2	122 \pm 3

After dynamic loading both composite materials showed higher deformability and lower hardness than that one after slow conventional deformations. These macroscopic data were consistent with the microscopic analyses obtained with TEM and X-Ray diffractions, in other words after such enhanced deformability there was no increase of lattice distortions, but a rather uniform distribution of dislocations (4). The samples reinforced with 19% of alumina showed no appreciable variations after both deformations in the microhardness values of the Al matrix near the alumina fiber (Fig. 4) The interface bond was good. No relevant differences in the wetting characteristics after different deformations were observed by AFM images (Fig. 1a, b); on the contrary the sample reinforced with a mixture of small alumina particles and fibers (Fig. 5 a) showed a wide spreading of all the fractured pieces of alumina fibers with random orientations which might be the consequence of the activation of new glide planes. The sample slow compressed, instead, showed (Fig. 5 b) a preferred orientation of the small fragments of alumina fibers. These small fractured pieces of alumina might serve as tracers of the deformation flow lines.

CONCLUSIONS

SEM, AFM and OM analyses were performed on aluminium metal matrix composites reinforced with fibers and particles of alumina. A good interface bond between the aluminium matrix and the aluminium oxide was observed by AFM after fast and low deformation. The optical micrographs of the dynamic loaded composite reinforced with Al₂O₃ fibers and particles showed a random distribution of the fractured alumina fibers which may be associated to a mechanisms of multiple-slip deformation.

REFERENCES

- 1) M.A. Meyers " A Mechanism for Dislocation Generation in Shock-Wave Deformation" Scripta Met. 12, (1978) 21.
- 2) P. Gondi, C. Patuelli and R. Tognato" Dislocation Source Activation by Load Impulses" Phy. Sta. Sol. a) 44, (1977) 333.
- 3) C. Patuelli and M. Zaffagnini" X-Ray Diffraction Line Broadening Fourier Analysis of a Dynamic Loaded Metal Matrix Composite Obtained by Liquid Infiltration" in Shock Waves, Takayama editor, Springer-Verlag, Berlin Heidelberg (1992) 387.
- 4) C. Patuelli, " X-Ray Line Broadening Analysis of Dynamic Loaded Aluminium Metal Matrix Composite" in Shock Waves, R. Brun and L.Z. Dumitrescu eds, Springer-Verlag, Berlin Heidelberg (1995) 311.
- 5) U. S. Patent n. 5164336, 16 November 1992.
- 6) P.S. Carli and M.A. Meyers in Shock Waves and High Strain Phenomena, Plenum Press, N.Y. (1981) 387.

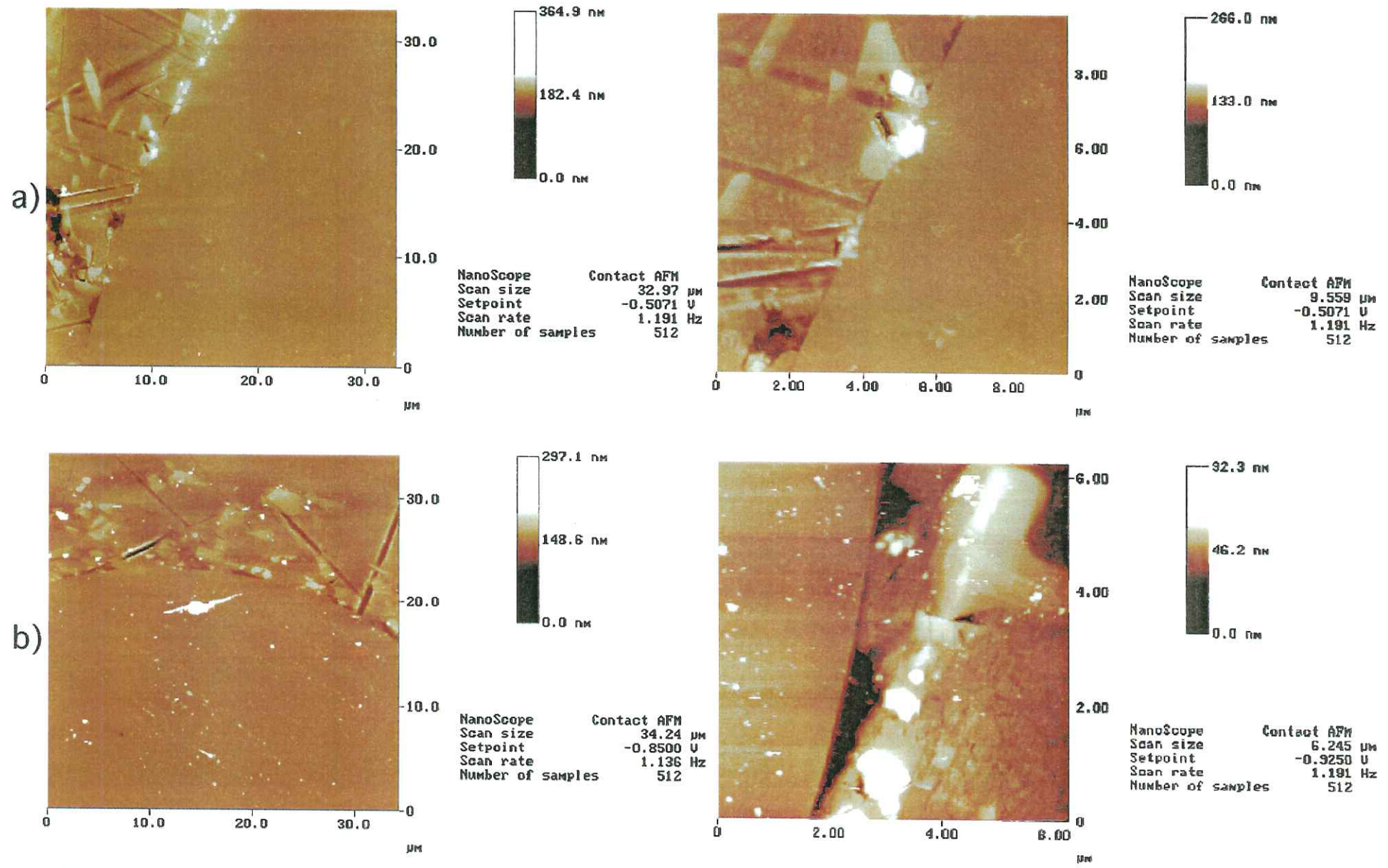
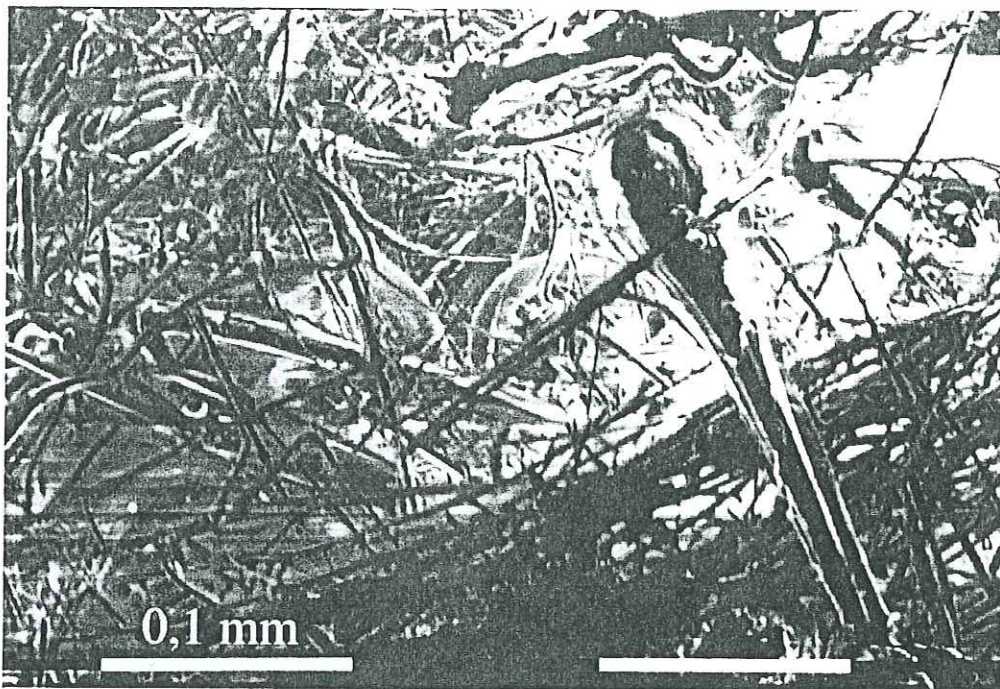


Fig.1 (a-b): a) AFM image of Al/19% Al₂O₃ interface after dynamic loading
b) AFM image of Al/19% Al₂O₃ interface after slow compression

a)



b)

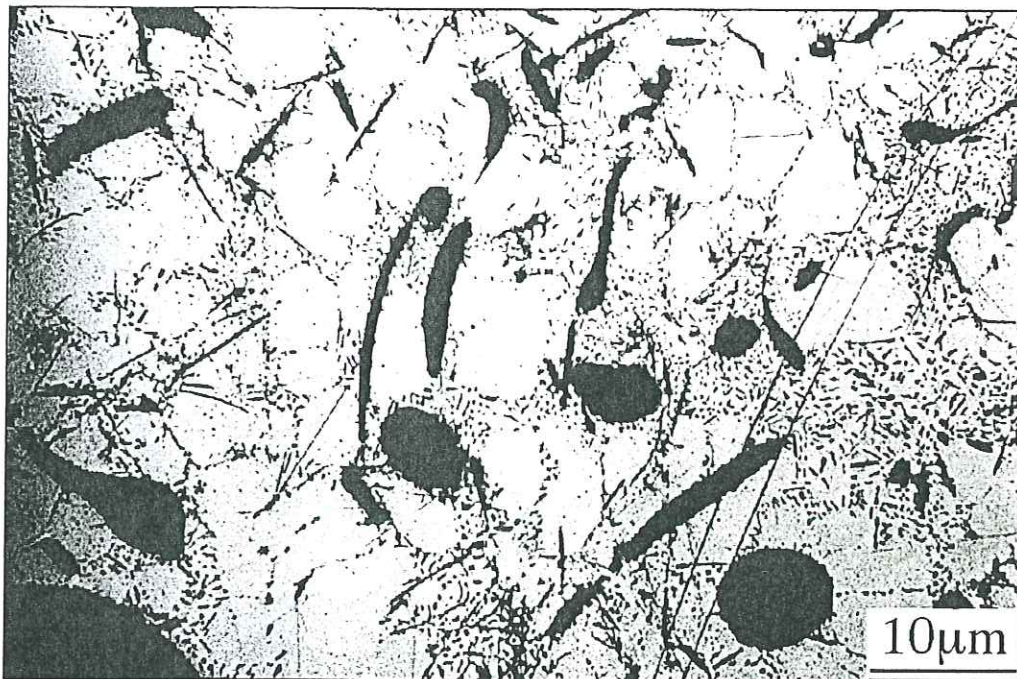
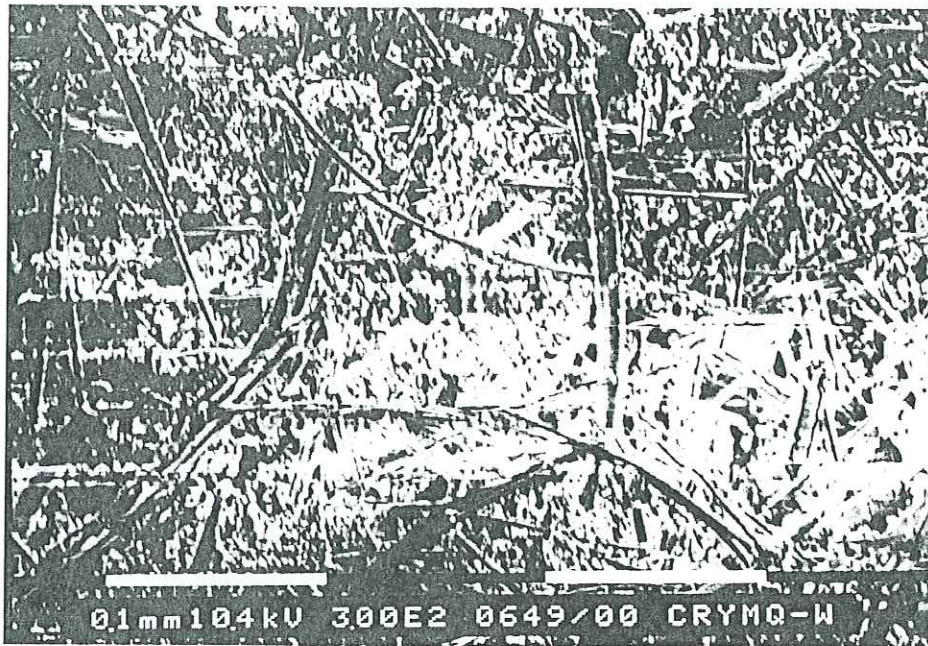


Fig.2 (a-b) :a) SEM image of Al/19%Al₂O₃ preform
b) Optical micrograph of Al/19%Al₂O₃ composite before deformation

a)



b)

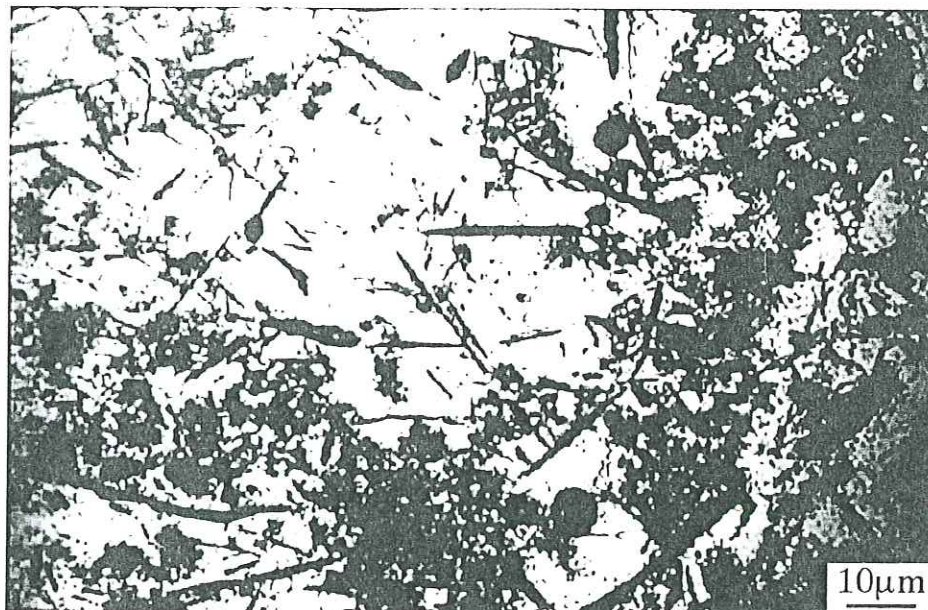


Fig.3 (a-b): a) SEM image of Al/10% Al₂O₃ preform
b) Optical micrograph of Al/10% Al₂O₃ composite before deformation

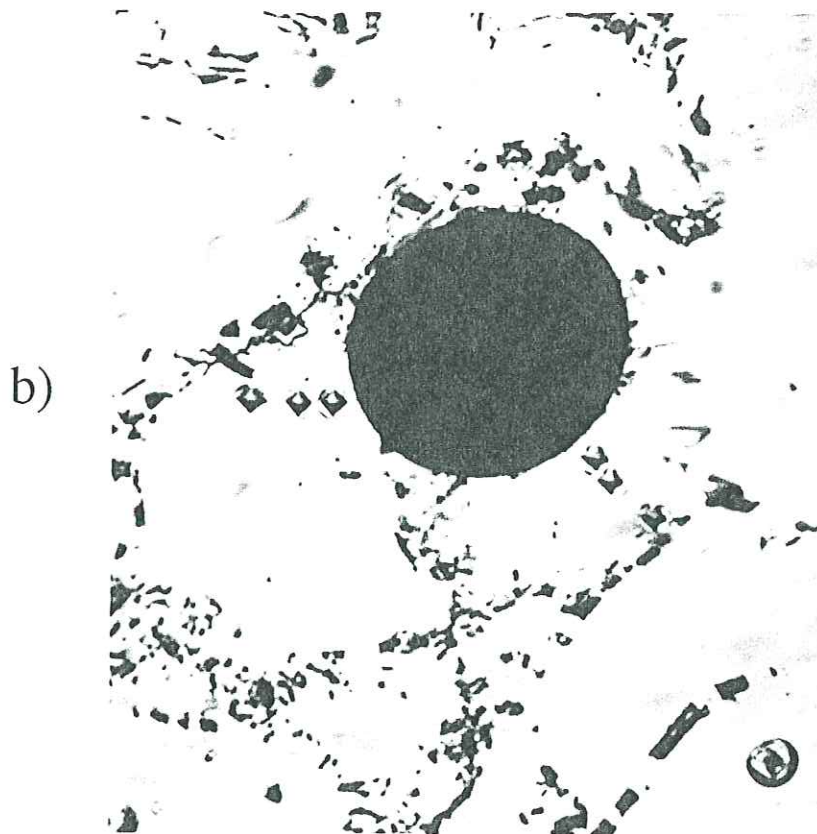
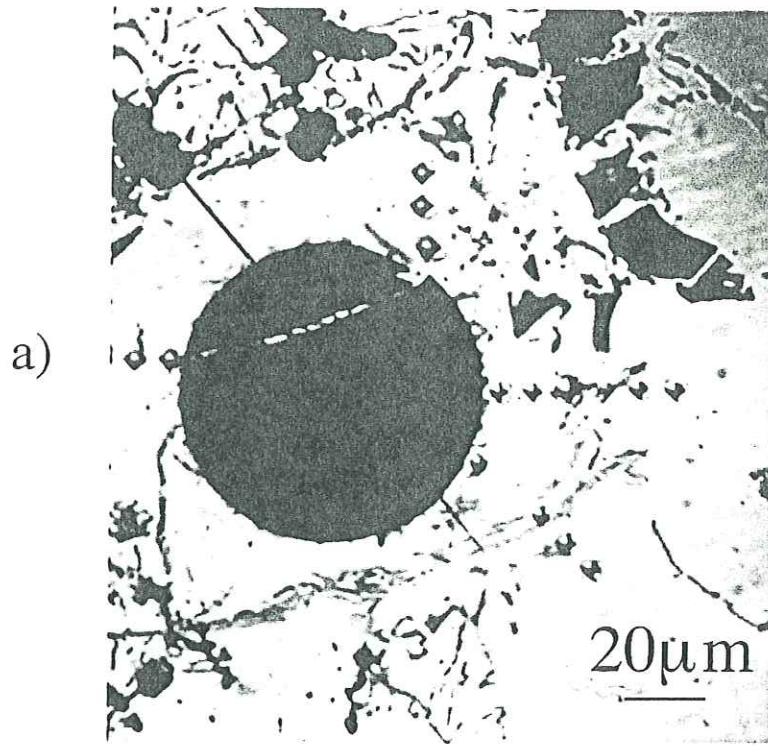
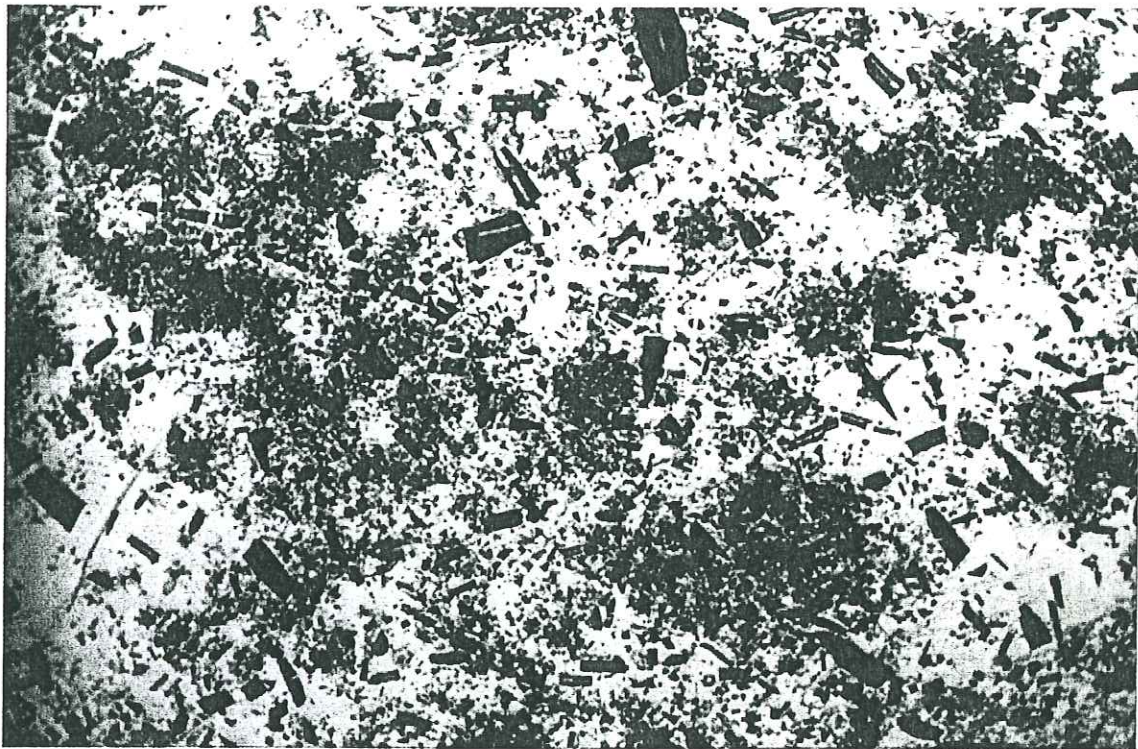


Fig.4 (a-b): a) Microhardness optical image of dynamic loaded sample (19% Al_2O_3)
b) microhardness optical image of slow compressed sample (19% Al_2O_3)

a)



b)

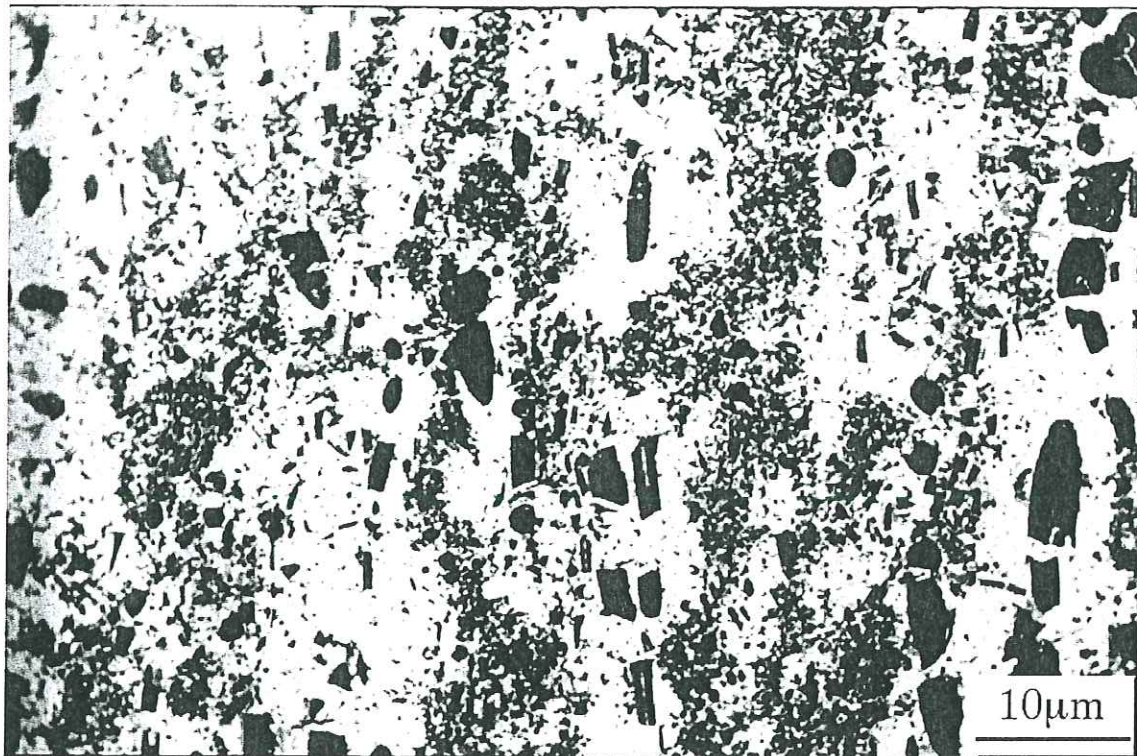


Fig.5 (a-b): a) Optical micrograph of dynamic loaded Al/10% Al₂O₃
b) Optical micrograph of slow compressed Al/10% Al₂O₃

THE SHOCK HUGONIOT OF CEMENT PASTE UP TO 5 GPa

K. Tsembeis, W. G. Proud and J.E. Field

PCS, Cavendish Laboratory, Madingley Road, Cambridge, CB3 0HE. UK.

A series of plate impact experiments has been performed to determine the shock loading behaviour of cement paste (grout with no aggregates) with water to cement ratio of 0.35 by weight. Hugoniot stress data were collected by means of embedded manganin gauges, up to 5 GPa. Results are compared to those obtained in previous studies on concrete with varying aggregate size using a plate reverberation technique coupled with velocity interferometry. Results indicate that the average loading of cement and concrete are comparable. In addition, the in-material gauge technique has the advantage of measuring the cement Hugoniot directly and provides measurements of the rise times, which were found to be inversely related to impact stresses.

INTRODUCTION

Considerable interest in characterising the dynamic loading of concrete under impact conditions exists because of its extensive use as a structural material [1-4]. Concrete is a heterogeneous material containing aggregates in a cement matrix. Therefore its characterisation under dynamic conditions is more complicated compared to homogeneous materials. For instance, impedance differences inside the concrete emanating from its component parts lead to variations in the particle velocities and longitudinal and lateral stresses. A way to remedy the situation is to average these variations by a plate reverberation technique where a disc-shaped specimen of the test concrete is mounted on the projectile and undergoes planar impact on a stationary diagnostic target (PMMA, copper, tantalum) [1-4]. However, it is impossible to obtain any further information such as wave rise time using the above technique. For this reason, the material understanding has to be built up starting from studies of the matrix (cement paste) and individual aggregates. In this paper, results are presented on the behaviour of the matrix material.

EXPERIMENTAL PROCEDURE

All shots were carried out on the single stage 50 mm gas gun at the University of Cambridge [5]. Tiles of cement paste were lapped flat to five optical fringes using 15- μ m silicon carbide grit. Commercial stress gauges (Micromasurements type LM-SS-125CH-048) were embedded between tiles using a low viscosity epoxy adhesive.

Target configurations are presented in Fig. 1. The gauges were made of manganin, the resistance-stress relationship of which is according to the earlier work of Rosenberg and Partom [6]. Specimens were aligned to the barrel of the gun using an adjustable specimen mount to within 1 mradian.

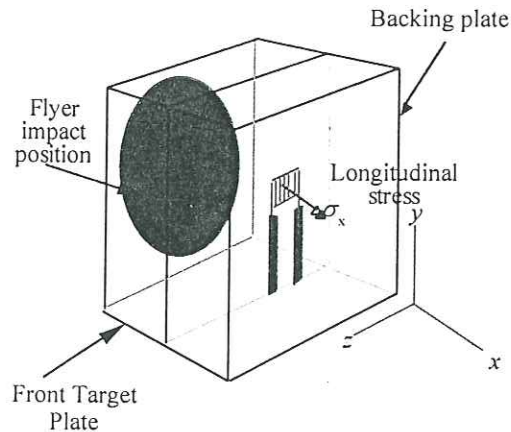


Fig 1: Target configuration

Polymethylmethacrylate (PMMA), aluminium alloy 6082-T6 and copper impactors were fired over a range of velocities to induce stresses between 0.5 - 5 GPa in the cement targets. Impactor velocities were measured using shorting pins giving an accuracy to within $\pm 0.5\%$. The cement paste tiles were supplied as 75-mm by 75-mm squares with two different thicknesses of 2-mm and 10mm. The gauge was mounted between a thin tile 2-3 mm and a thick one 5-20 mm. One experiment was performed (Table 1: 15Hcem) where a 10-mm cement flyer impacted onto an aluminium target.

MATERIAL DATA

Cement paste tested in this study was prepared and supplied by Concrete Structures Section (CSS), Department of Civil & Environmental Engineering, Imperial College, London, UK. The paste had a water-to-cement ratio of 0.35 by weight with free water content of 7.4 – 8.9% by weight. Specimens were cured for 21 days in a water-bath at 20 °C. Density and ultrasonic measurements were performed after grinding, using samples from different sets. The density had a value of $2.0 \pm 0.2 \text{ g cm}^{-3}$ while the longitudinal and shear elastic wave velocities were determined to be 3.7 ± 0.2 and $2.2 \pm 0.2 \text{ km s}^{-1}$, respectively. Density variations resulted from different initial porosity. Density measurements and variations were in good agreement with independent measurements performed by CSS.

RESULTS AND DISCUSSION

Figure 2 illustrates some typical stress wave profiles as obtained from the gauges. The cement Hugoniot results are summarised in table 1; the number in parentheses is the error in the stress amplitude. The Hugoniot curve is shown in Fig. 3, while the shock velocity versus particle velocity data are plotted in Fig. 4. It should be noted that the error bars in both figures represent the errors in measurements. The Hugoniot Elastic Limit (HEL) was directly estimated from the stress profiles showing a two- wave structure. The stress at HEL was $0.30 \pm 0.05 \text{ GPa}$, while the particle velocity

was $40 \pm 10 \text{ m s}^{-1}$. The Hugoniot curve and shock velocity – particle velocity plot show some scatter in the data which can be attributed to different initial porosity in the samples. Different free water content during manufacture together water evaporation during target preparation may contribute to these differences. A linear least square fit of the shock velocity to particle velocity plot yields $U_s = 952 + 5.45 u_p$. The large slope, S , can be attributed to the porous nature of the material. Figure 5 again illustrates the cement paste Hugoniot curve with Hugoniot data for two different kinds of concretes, that is, SAC-5 and CSPC [2,4].

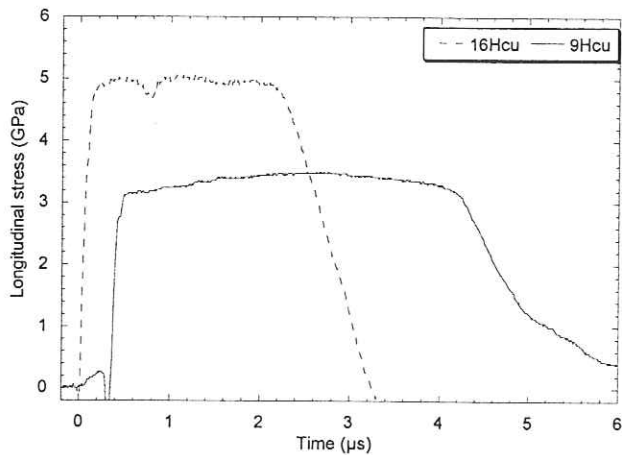


Fig 2: Representative stress wave profiles
(see Table 1 for impact conditions)

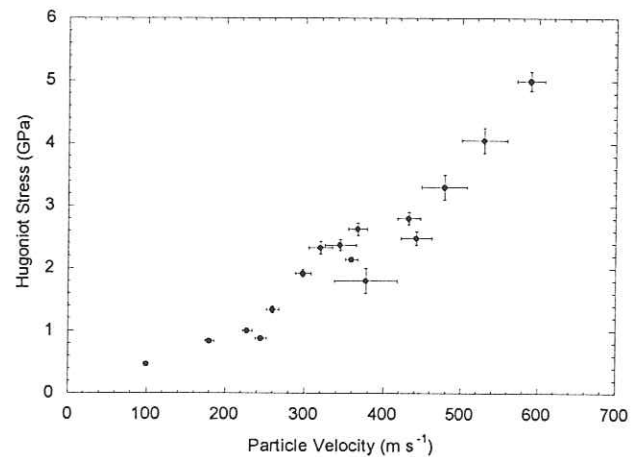


Fig 3: Cement Hugoniot curve in stress-particle velocity space

It can be seen that the data are tightly grouped together, suggesting that making concrete by the inclusion of aggregates in a cement matrix does not significantly affect the Hugoniot curve up to stresses of 5 GPa. Finally, the in-material gauge technique has the advantage of acquiring further information about the cement paste. The time required for the stress wave profiles to reach a steady value is inversely proportional to the Hugoniot stress as a result of increased void collapse and kinetics. This is illustrated in Fig. 6 where the data are well described by a fit of $\sigma = 1.29/t$, where σ is the Hugoniot stress and t is the rise time. In addition, at high stresses the rise time seems to asymptote to a value of *ca.* 400 ns. This value lies close to the generic embedded gauge response time (*ca.* 200 ns). Therefore, this asymptote may be an artefact of the gauge response. However rise times greater than 500 ns cannot be attributed to this effect.

CONCLUSIONS

Hugoniot data have been collected for the cement paste using the in-material gauge technique up to 5 GPa. Results indicate that Hugoniot curves of cement paste and concrete are comparable suggesting a weak dependence on aggregate inclusion. The shock velocity vs. particle velocity is well described by the linear relation $U_s = 952 + 5.45 u_p$. In addition, the rise time of the stress profiles is inversely proportional to the Hugoniot stress showing the porous nature of the material.

TABLE 1: Experimental Parameters and Hugoniot Data

Shot No.	Impactor Material and Thickness (mm)	Target Front (mm)	Target Back (mm)	Impact Velocity (m s ⁻¹)	Stress (GPa)	Shock Velocity (m s ⁻¹)	Particle Velocity (m s ⁻¹)
1Hal	10 Al	2	5	250	0.84 (0.04)	1955 (305)	180 (6.0)
2Hal	10 Al	2	6	511	1.80 (0.20)	2242 (416)	378 (40)
3Hal	10 Al	4	10	359	1.34 (0.06)	2384 (246)	260 (8.0)
4HPMMA	10 PMMA	3	10	228	0.47 (0.01)	1454 (509)	100 (3.0)
5Hcu	10 Cu	2	13	511	2.48 (0.11)	2726 (226)	442 (20)
6Hal	10 Al	2	10	435	1.92 (0.06)	3152 (259)	298 (10)
7Hcu	10 Cu	2	10	509	2.80 (0.10)	3199 (224)	432 (15)
8Hal	10 Al	2	10	510	2.37 (0.09)	3403 (328)	345 (20)
9Hcu	10 Cu	3	10	569	3.30 (0.20)	3432 (346)	478 (30)
10Hcu	6 Cu	2	10	641	4.05 (0.20)	3829 (330)	530 (30)
11Hal	10 Al	2	10	484	2.33 (0.10)	3633 (342)	320 (15)
12Hal	6 Al	2	10	548	2.63 (0.10)	3570 (269)	367 (12)
13Hal	10 Al	2	10	314	0.88 (0.03)	1443 (165)	245 (7.0)
14Hal	10 Al	2	10	510	2.14 (0.04)	2898 (170)	359 (8.0)
15Hcem	10 Cem	5	5	292	1.00 (0.03)	1887 (202)	228 (6.0)
16Hcu	6 Cu	2	20	727	5.00 (0.15)	4271 (235)	590 (18)

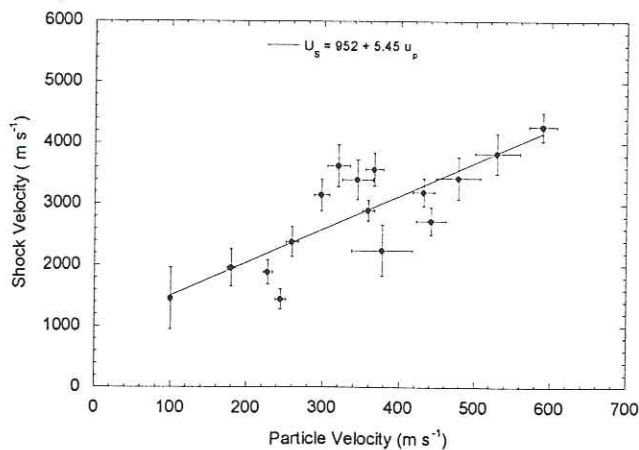


Fig 4: Shock velocity – particle velocity data for cement

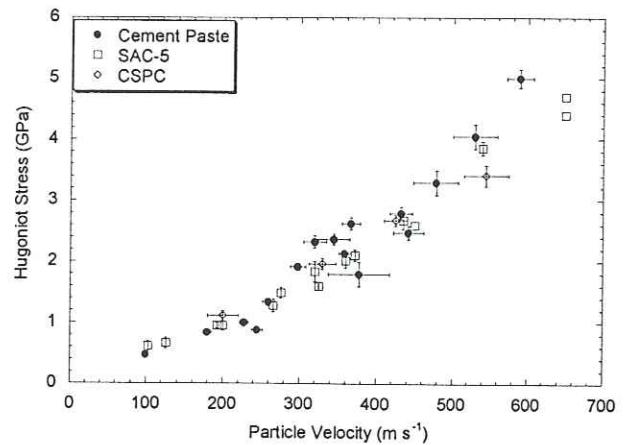


Fig 5: Stress – particle velocity plot for cement and concrete

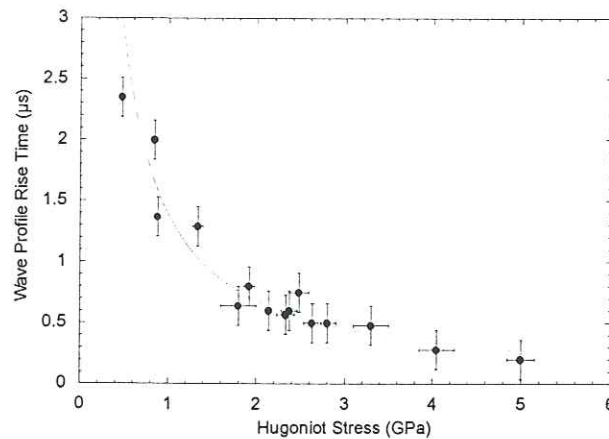


Fig 6: Rise time of wave profiles versus Hugoniot stress

ACKNOWLEDGEMENTS

The Defence and Evaluation Agency, UK has sponsored this work, under contract WSS/U3257. Professor N.K. Bourne provided assistance during the early stages of this program. Dr. A. Pullen from Imperial College provided the cement samples. Dr J. Sheridan, I.G. Cullis and P.H. Church are thanked for their interest. Finally, we thank D.L.A. Cross and R. Flaxman for technical support.

REFERENCES

1. Grady, D. E., "Impact Compression Properties of Concrete", in *Proceedings of the Sixth International Symposium on Interaction of Nonnuclear Munitions with Structures, Panama City Beach, Florida*, pp. 172-175, May 3-7 (1993)
2. Hall, C. A., Chhabildas, L. C., and Reinhart, W. D., "Shock Hugoniot and Release States in Concrete Mixtures with Different Aggregate Sizes from 3 to 23 GPa," in *Shock Compression in Condensed Matter-1997*, edited by S. C. Schmidt et al., AIP Conference Proceedings 429, New York, 1998, pp. 119-122.
3. Grady, D. E., "Shock Equation of State Properties of Concrete," in *Structures under Shock and Impact IV*, edited by N. Jones et al., Computational Mechanics Publications, Southampton, 1996, pp. 405-414.
4. Kipp, M. E., Chhabildas, L. C., and Reinhart, W. D., "Elastic Shock Response and Spall Strength of Concrete," in *Shock Compression in Condensed Matter-1997*, edited by S. C. Schmidt et al., AIP Conference Proceedings 429, New York, 1998, pp. 557-560.
5. Bourne, N. K., Rosenberg, Z., Johnson, D. J., Field, J. E., Timbs, A. E., and Flaxman, R. P., *Meas. Sci. Technol.* **6**, 1462-1470 (1995).
6. Rosenberg, Z., Yaziv, D., and Partom, Y. J., *J. Appl. Phys.* **51**, 3702-3705 (1980).

BALLISTIC IMPACT ON POLYMERIC COMPOSITE MATERIALS

Silva, N.M.* , Travassos, J.M.C.†, Freitas, M.J.M.*

Presentation of an analysis method to simulate ballistic impact of small ammunition with a known cylindrical radius, mass and speed.

This method requires experimental data at two different speeds (with several shots for statistical purpose) for the same type of target. With these results we are able to trace a chart (speed - extension) that will allow an extrapolation of the behaviour for different impact speeds and thicknesses, on the same material.

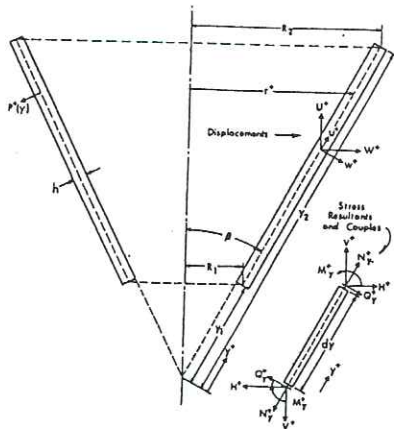
* Instituto Superior Técnico

† Instituto Superior de Engenharia de Lisboa

BALLISTIC IMPACT ON POLYMERIC COMPOSITE MATERIALS

⇒ THEORETICAL BACKGROUND

• CONICAL SHELL THEORY



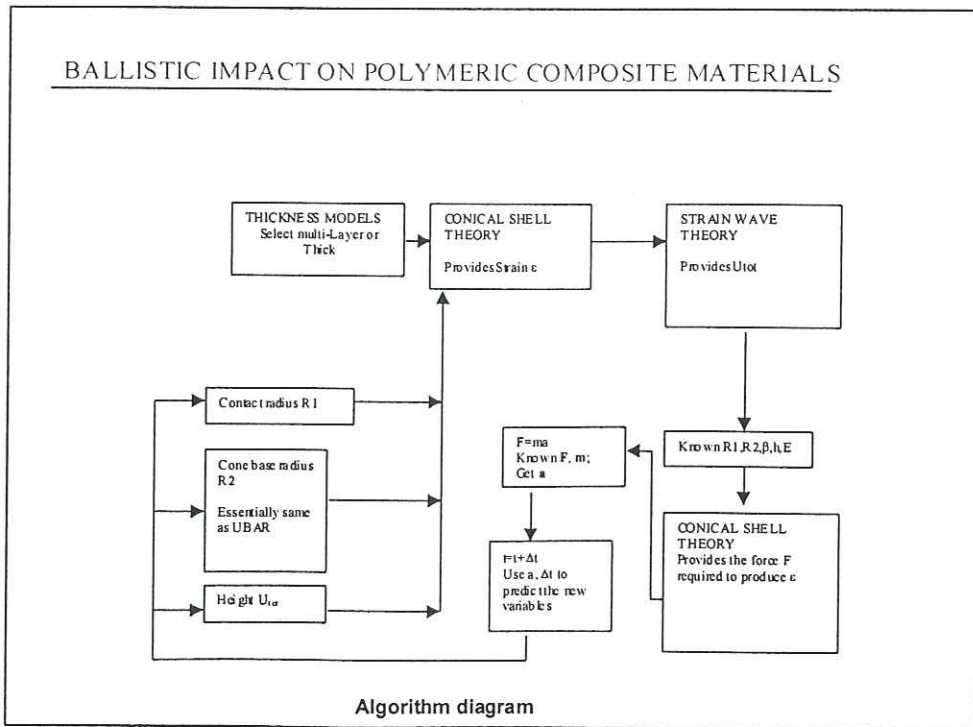
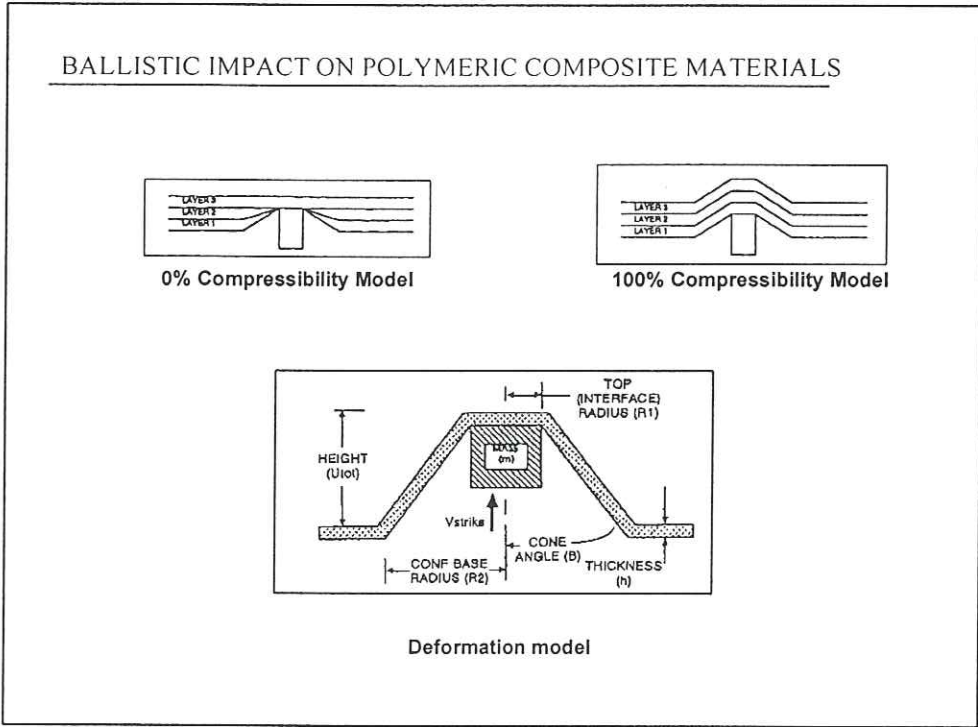
$$H = \frac{C_9}{y \cos \beta}; N_y = \frac{C_9}{y \sin \beta \cos \beta}; N_\theta = Q_y = 0$$

$$\epsilon_y^0 = \frac{C_9}{Eh \sin \beta \cos \beta} \frac{1}{y}; w = \frac{-C_9}{Eh \cos^2 \beta} \ln y$$

$$\beta_y = \frac{C_9}{Eh \cos^2 \beta} \frac{1}{y}$$

$$U = \frac{C_9}{Eh \cos^2 \beta \sin \beta} \ln y + \text{constant}$$

• TRANSVERSE PROPAGATION WAVE THEORY



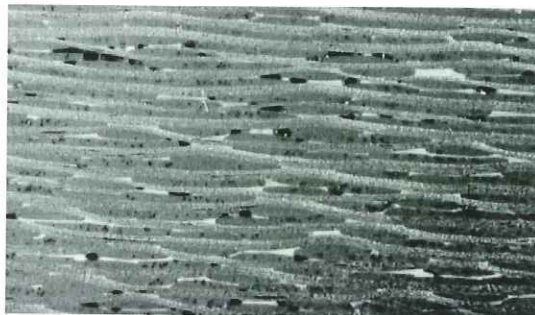
BALLISTIC IMPACT ON POLYMERIC COMPOSITE MATERIALS

An iterative procedure is formulated that uses a computer to obtain extensions, decelerations and residual speeds, as a function of time.

The analytical results are compared with experimental data for an impact in a target of glass fiber, with a 7.62NATO ammunition.

BALLISTIC IMPACT ON POLYMERIC COMPOSITE MATERIALS

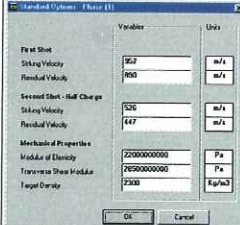
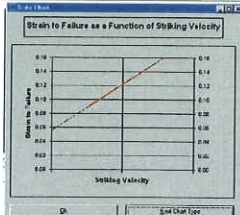
⇒ MATERIAL CHARACTERISTICS



•Fibre	E Glass
•Matrix	Polyester
•Thickness	9mm
•Stacking sequence	[(0/90) _{fg}] ₁₀
•Density	1.81
•Young modulus	22GPa
•Transverse shear modulus	28.5GPa

BALLISTIC IMPACT ON POLYMERIC COMPOSITE MATERIALS

⇒ COMPUTATIONAL METHOD

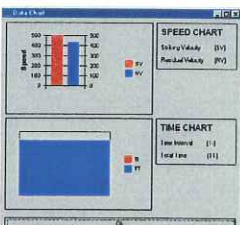



Projectile Mass: 0.03045 Kg Material Density: 2380 Kg/m ³ Material Thickness: 0.01 m Young Modulus: 22000000000 Pa Transverse Modulus: 2850000000 Pa Rt: 0.007249 m CS: 3520.12845615413		Beta Calculus Run Calculus Abort Calculus Pause Calculus Reinitalize Calculus Print Show Chart Exit		
Time: 0.000025 Acceleration: -3315911.55898293 Projectile Speed: 447.250314803937 Urot: 0.04209572642089 R2: 9.5252214038534E-42 Angle Beta: 82.1739364146215 Max Strain: 8.73016656984591E-02 Vyt: 261795.189134787				
Shot1 Iterations	9	Shot2 Iterations	26	
SECOID SHOT Extension Calculus Time Interval: 0.000001 s				
First Shot	Striking Velocity	952	Extension Value1	0.156208858765202
	Residual Velocity	890	Projectile Speed	882.530248510768
	Speed precision due to time gap: 99.1607820798616 %			
Second Shot	Striking Velocity	576	Extension Value2	0.90318886824892E-02
	Residual Velocity	447	Projectile Speed	443.334403875835
	Speed precision due to time gap: 99.1799561479832 %			

Phase 1 - Characteristic function

BALLISTIC IMPACT ON POLYMERIC COMPOSITE MATERIALS

⇒ COMPUTATIONAL METHOD

Projectile Mass: 0.03045 Kg Striking Velocity: 500 m/s Material Density: 2380 Kg/m ³ Material Thickness: 0.01 m Young Modulus: 22000000000 Pa Transverse Modulus: 2850000000 Pa Rt: 0.007249 m CS: 3520.12845615413 TA = 0.00000001		Run Simulation Abort Simulation Pause Simulation Reinitalize Simulation Show Chart Print Exit Next Iteration
Projectile Speed 433.281124329767 Extension 8.49948675483576E-02 Urot 1.21648215133482E-02 Angle Beta 82.3562691898265		Number of Iterations 2576
Axial Loading 7487067.18345867 Acceleration -3728123.1048518 R2 9.78923077459644E-02 Time 1.38589999999973E-04		Max Extension 8.49879515889593E-02

Phase 2 - Simulation

BALLISTIC IMPACT ON POLYMERIC COMPOSITE MATERIALS

⇒ COMPUTATIONAL METHOD

Optimization Type: Thickness Maximization		Initial Speed	500 m/s
Optimization Iterations	11	Initial Thickness	0.01 m
Number of Iterations	4083	Optimized Thickness	0.02 m
Max Extension	8.4987951568999E-02	TA	0.00000001 s
Projectile Speed	-0.186686762333176 m/s	Axial Loading	1518290.92482859 N/m
Extension	5.36892280352809E-02 Pa	Acceleration	-2271044.62437423 m/s ²
Utot	2.40313652325958E-02 m	R2	0.380382616352346 m
Angle Beta	86.3150815811291 °	Time	1.06206000000042E-04 s

Phase 3 - Optimisation

BALLISTIC IMPACT ON POLYMERIC COMPOSITE MATERIALS

⇒ COMPUTATIONAL METHOD

Projectile Mass: 0.03045 Kg
Striking Velocity: 500 m/s
Material Density: 2300 Kg/m³
Material Thickness: 0.01 m
Young Modulus: 22000000000 Pa
Transverse Modulus: 28500000000 Pa
R1: 0.007249 m
CS: 3528.42845615413
TA = 0.00000001

Max Extension	8.4987951568999E-02	Number of Iterations	2576
Number of Layers	XXXXXXXXXX		
Time	2.89408999999976E-04		
INCOMPRESSIBILITY METHOD		COMPRESSIBILITY METHOD	
Projectile Speed	433.281124329767	Projectile Speed	492.800285500108
Extension	8.49904675463576E-02	Extension	5.39265238650592E-02
Utot	1.21648215133402E-02	Utot	1.28004831640884E-02
Angle Beta	82.3562691890265	Angle Beta	5156.62015617741
Axial Loading	2487062.16345667	Axial Loading	288944.004628638
Acceleration	-3720123.1048518	Acceleration	-432199.58815296
R2	9.78923877459664E-02	R2	9.78923877459664E-02
% METHOD DIFFERENCE		12.077748637107 %	

Compressibility Vs. Incompressibility Model

BALLISTIC IMPACT ON POLYMERIC COMPOSITE MATERIALS

⇒ EXPERIMENTAL RESEARCH



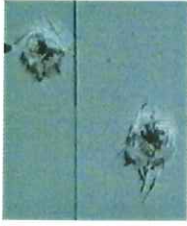
Data acquisition



Infra-red cells for speed measurement



Target holder



Target impact on entry



Target impact on exit

BALLISTIC IMPACT ON POLYMERIC COMPOSITE MATERIALS

⇒ COMPARISON OF ANALYTICAL AND EXPERIMENTAL RESULTS

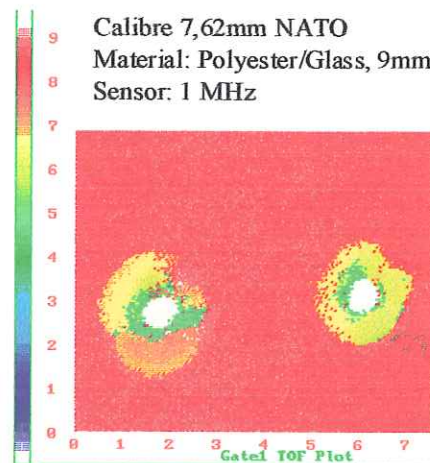
7.62NATO AMMUNITION

Striking Velocity	Predicted Residual Velocity	Actual Residual Velocity
839	771	798
554	470	512
357	321	322
226	174	174

Striking Velocity	Predicted Number of Layers to Stop	Actual Number of Layers to Stop
345	3	4
338	3	4
243	2	2

BALLISTIC IMPACT ON POLYMERIC COMPOSITE MATERIALS

C-Scan shows the influence of the projectile impact on delamination. The flaw size, shape and location of delamination is regular from shot to shot confirming the ability of the material to produce ballistic targets.



Left shot:
Initial velocity
586m/s
Residual velocity
551m/s

Right shot:
Initial velocity
521m/s
Residual velocity
473m/s

BALLISTIC IMPACT ON POLYMERIC COMPOSITE MATERIALS

BIBLIOGRAPHY

- Vinson, J. R. & Walker, J. M., "Ballistic Impact of Thin-Walled Composite Structures", AIAA Journal, Vol. 35, Nº 5, May 1997, pp.876-878.
- Taylor, W. J. Jr., "An Analytical and Experimental Investigation of Ballistic Impact into Fabrics", M.S. Thesis, Dept. of Mechanical Engineering, Univ. of Delaware, Newark, DE, June 1988.
- Vinson, J. R., "Edge Load Solutions for Conical Shells," Journal of Engineering Mechanics Division, ASCE, Vol. 92, Feb. 1966, pp.37-58.
- Smith, J. C., Fenstermaker, C. A., & Shouse, P. J. "Stress-Strain Relationships in Yarns Subjected to Rapid Impact Loading. Part X: Stress-Strain Curves Obtained by Impacts with Rifle Bullets", Textile Research Journal, Nov. 1963, pp.919-934.
- Vinson, J.R. & Zukas, J.A., "On the Ballistic Impact of Textile Body Armor", Journal of Applied Mechanics, Vol.42, June 1975, pp.263-268
- Taylor, W. J. Jr. & Vinson J. R., "Modeling Ballistic Impact into Flexible Materials", AIAA Journal, Vol.28, Nº 12, 1990, pp 2098-2103.

AKNOWLEDGMENTS

- Artur M. J. Baptista, Nuno L. A. Mesquita e Carla A. S. Pessoa, Universidade Autónoma de Lisboa.
- António J. Fialho, Indústrias e Participações de Defesa S.A..
- Cristina C. V. Montez, Oficinas Gerais de Material Aeronáutico.

The behaviour of aluminium metal matrix composites in cold forming using superimposed hydrostatic pressure, large strains and elevated strain rates.

M. Nastran, K. Kuzman

Faculty of Mechanical Engineering, University of Ljubljana, Slovenia, 1000 Ljubljana, Aškerčeva 6

B. Dodd (of Adtek International Ltd.)

93, Jack Straw's Lane, Oxford, OX3 0DW, UK

Abstract

A new approach to the evaluation of the flow curve of an aluminium composite with the help of a steel ring is presented. The results are extracted using numerical simulation supported by a large number of experiments. Several compression tests were carried out using cylinders made of aluminium metal matrix composite (MMC). There is an additional hydrostatic pressure, which is the result of the steel ring, superimposed on the basic stress state. This hydrostatic pressure allows the MMC to be deformed to very large strains without cracking, thus showing that cold forming of these materials is possible. Finally, the comparison between two different cross-head speeds is presented and discussed; one of these cross-head speeds is typical of an industrial press while the other is to be found in laboratory presses. It is shown that forming at impact rates provides more ductility in the material because of the effects of adiabatic heating.

1. Introduction

There is a tendency in modern engineering to use lighter alloys for many applications, particularly in the aerospace and automobile industries. An example of such a material is aluminium which has a density which is about a third of that of steel. The problem with these materials is their bad mechanical properties [1,2]. These weaknesses could be improved by using a basic alloy reinforced with different kind of hard particles. There are obvious improvements in Young's modulus and tensile strength for aluminium MMCs, for example [3,4]. The test material used here is aluminium alloy 2124 reinforced with 10 micron diameter SiC particles (10% of volume fraction).

As the tensile strength increases there is a decrease in the elongation as the material is more brittle. This property is unwelcome in cold forming processes and some problems dealing with the formability of such materials have already been published [5,6,7]. Metal matrix composites are difficult to cold form. The investigations published so far are restricted only to low strains which means that they are not suitable for cold forming by conventional techniques.

The formability of these materials is improved by proper heat treatment before the forming process. The strains achieved in this case are up to 0.6. From the economic point of view it is not the cheapest way for improvement, in addition, the mechanical properties are also affected. It is more suitable to use non-heat treated material and to use different forming techniques.

Using new materials in cold forming technologies means a completely new approach to process planning (die making, forming machinery, tool life and wear etc.) because the forming properties are not known beforehand. The most important factors are the flow curve and formability. It is necessary to know very exactly the flow stress of the work material at different strains and at different cross-head speeds because a

successful process planning depends on both of them. It is also necessary to know the limiting deformation before the on-set of cracking.

2. Problems connected with forming of MMC to high strains

2.1 Material properties of MMC 2124 10%SiC

The material used is an aluminium composite based on aluminium alloy 2124 reinforced with 10 % volume fraction of SiC particles with an average diameter of 10 microns. It is well-known that aluminium is difficult to form [8]. Even though it is basically very soft with a low yield strength, it causes many problems in forging. Friction between the die and the work-piece is a problem because of the adhesion of the work material to the forming tool. Great care has to be taken with forging to high strains and suitable lubrication must be used. Cold forming of MMCs is further more complicated because in addition to the forming problems of the base material, other problems are expected due to brittleness caused by the SiC particles. The elongation to failure of test specimens decreases with increasing volume fraction of SiC. It is possible to overcome this problem with proper heat treatment, but only to a certain extent.

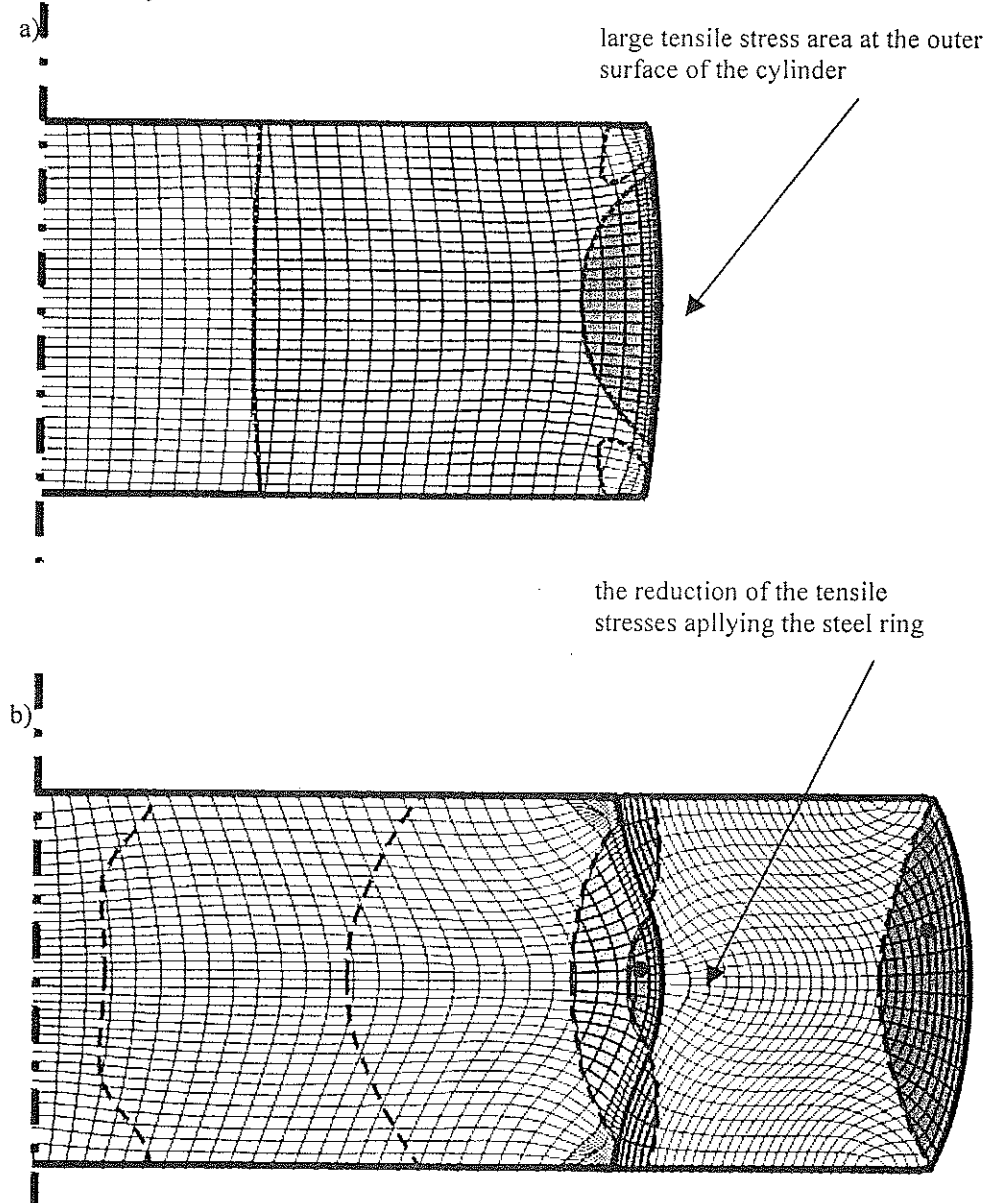


Fig 1: Numerical simulation showing the development of tensile stresses on the outer surface of the cylinder. a) without ring (the tensile stress area is larger), b) with ring (smaller tensile stress area, shaded regions show an equal stress level)

The materials have to be formed by predominantly compressive processes. The hydrostatic pressure which is superimposed on the basic stress state is necessary for a successful forming process [9,10]. This is because the pressure stops the work material from cracking. This particular MMC material exhibits a large difference between the flow properties in tension and compression. Also there is a large difference in failure mechanisms for both stress states.

To form this brittle material successfully, it is necessary to simulate the stress state that will be used in practice. Therefore conventional compression testing within a hydrostatic pressure chamber is unrealistic. The method proposed here is to use a steel ring surrounding a cylinder of MMC. The ring restricts flow of material within the cylinder and induces a high hydrostatic pressure.

It is impossible to eliminate friction in cold upsetting of a cylinder. Friction causes tangential stresses in the outer region of the specimen. (the results of the numerical simulation is presented in fig.1) It is a matter of fact that such a stress state also occurs at relatively low coefficients of friction (lubricated with Teflon $\mu=0.02-0.03$). Cracks occur at very low levels of plastic deformation and cause failure [11,12].

In addition, when forming with high cross-head speed there is a strong impact of the heat generated which may perhaps lower the forming force. Heat generation has not been explicitly evaluated but knowing the cross-head speed at forming it is possible to compare this upsetting test with other forming processes where speed coincides with experiment.

3. Improving the formability of the aluminium MMC

Usually the superposition of hydrostatic pressure is made using a fluid in a special chamber, but in practice, in mass production, it is impossible to assure this kind of process improvement. A new approach of applying hydrostatic pressure is to squeeze a cylinder in the radial direction. In this case the tangential pressure equals the radial pressure, which can be derived through the basic elasto-mechanical equations [8].

$$\sigma_{rr} = A + Br^{-2}$$

$$\sigma_{\varphi\varphi} = A - Br^{-2}$$

The method for inducing a radial pressure is to use a ring made of a ductile steel with good forming properties as shown in fig.2. The outer ring compresses with the cylinder and it restrains the inner material from flowing outwards. Of course the material flows outwards, radially but with an additional radial stress. Reduction of the tensile stress area is clearly noticeable, as presented in fig.1.

The force and height were measured during deformation and using a numerical simulation it is possible to derive the flow curve for the MMC.

4. Determination of dimensions using numerical simulation

The finite element analysis was conducted with the ABAQUS package. The outer diameter of the steel ring was estimated using the numerical simulation. It was necessary to ensure a high inner hydrostatic pressure to ensure proper material flow of the MMC, so that it did not to crack. It was impossible to ensure a proper hydrostatic stress, which will not be too high and at the same time not to low, to prevent crack growth. There are two important aspects; firstly, the outer diameter should not be to large, because increasing it means also an increase in the forming force and a low accuracy of measurement and therefore only an approximate evaluation of the flow stress-strain curve. If the outer diameter of the ring is too small, then no advantage of the hydrostatic pressure is obtained. Thus the dimensions

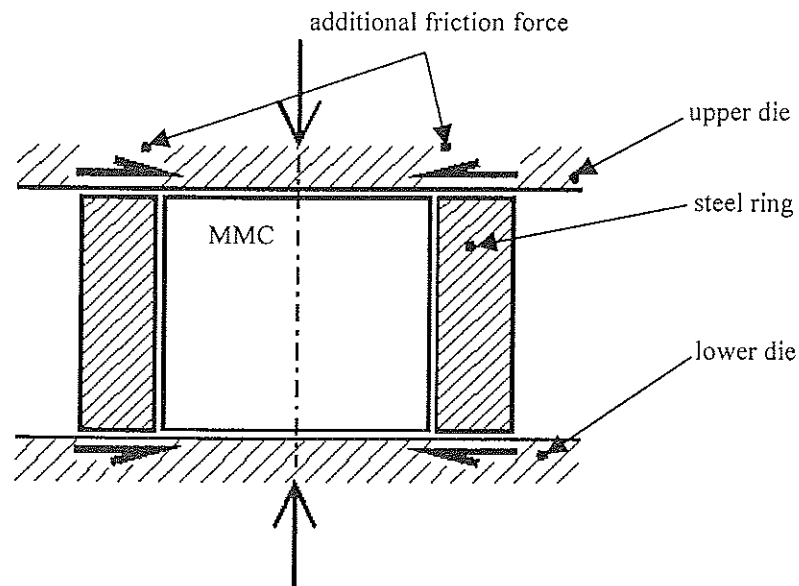


Fig 2: Experimental set-up

were determined such that the forming force needed for upsetting of a cylinder equalled the forming force needed for upsetting of the ring.

The second problem when using a thin ring is buckling. The coefficient of friction was also simulated and this is very important for good experiments. Friction is very important in obtaining a high inner hydrostatic pressure. So it is not suitable to use good lubricants, but to use proper lubricants and to grease as much as required. The higher the friction the more the cylinder material is prevented from flowing outwards radially and the higher is hydrostatic pressure.

This is a doubled-edged problem because it is necessary to balance the induced hydrostatic pressure with the inhomogeneous plastic deformation caused by high coefficients of friction. It would be ideal if the cylinder were frictionless and the steel ring is subjected to sticking friction. As a compromise oil was used to lubricate the MMC cylinders and the steel ring. It is also helpful to understand the nature of the contact between the ring and the cylinder. The material flow of the cylinder is completely different when applying a steel ring on the outer surface.

The degree of slipping friction between these surfaces depends on the coefficient of friction there. It is difficult to determine the nature of friction in this region. The ring was manufactured to have a clearance of 0.01 mm with the cylinder. It has to be as small as possible in order to ensure high inner hydrostatic pressure.

5. Method of determination of the flow curve

Using two different materials in a compression test, where the flow curve of one material is well known, it is possible to extract the flow properties of the other. The forming force is measured by experiment and, supported with numerical simulation, it is then possible to find what part of this force is used for forming the ring and the cylinder. The statement is again very controversial because the material properties of the MMC, which it is necessary to input to ABAQUS in order to obtain meaningful calculations are not known. Thus, the whole procedure consist of three iterations, taking into account the numerical results and experimental data. Data from the literature [8] was used for the first approximation.

Using numerical simulation and numerical integration over the contact surface between the steel ring and the tool, it is possible to determine the force needed for forming of the cylinder exactly. The force needed for upsetting of the cylinder equals:

$$F_z = \int_{Rin}^{Rout} \sigma_{zz}(r) 2\pi r dr \approx \sum_{i=1}^{i=n} \left[\sigma_{i-1}(x_i^2 - x_{i-1}^2) + \frac{\Pi}{3}(\sigma_i - \sigma_{i-1})(2x_i^2 - x_i x_{i-1} - x_{i-1}^2) \right] \quad (1)$$

x_i - coordinate of node i in x direction on the contact surface between the tool and the work-piece

σ_{zz} - vertical stress

σ_i - vertical stress in the node i

The result obtained is the vertical force on the steel ring. We have to subtract this force from the overall forming force. The second step is the calculation of the average radial pressure on the contact surface between the ring and cylinder. This was carried out using the following equation:

$$\overline{\sigma_{rr}} = \frac{1}{h_{cil}} \int_0^{h_{ob}} \sigma_{rr}(h) dh \approx \frac{1}{h_{cil}} \sum_{i=1}^{i=n} \frac{(\sigma_{i-1} + \sigma_i)}{2} * (y_i - y_{i-1}) \quad (2)$$

y_i - coordinate of node i in y direction on the contact surface between the steel ring and MMC cylinder

σ_{rr} - radial stress

σ_i - radial stress in the node i

h_{cil} - the height of steel ring and MMC cylinder

It was assumed that the deformation of the cylinder was completely homogenous (this is not true but it is necessary to propose it for the calculations). So the average logarithmic strain could be calculated based on the height reduction.

The overall forming force subtracted by the vertical force on the steel ring gives us the necessary force for forming of MMC cylinder.

$$F_{all} = F_{st} + F_{MMC} \quad (3)$$

$$F_{MMC} = F_{flow} + F_{friction} + F_{rad\ stress}$$

We can divide this normal stress into three parts: the stress state induced by the material, the friction stress and the stress applied with radial pressure of the steel ring.(eq.3) Because of the ring set-up, the ring causes an additional radial pressure which requires a higher overall vertical load on the cylinder.

It was impossible to obtain the true results of the flow curve in the first step of calculation. The simulation had to be performed in three iterations. The numerical and experimental results were in this case almost the same. The measured forming force and simulated force were practically identical.

Calibration of the results was necessary due to the assumption of the homogeneity of plastic deformation. Friction on the contact surfaces prevents the material from flowing radially, so a smaller plastic deformation in that region occurs. However, the deformation in the inner region of the cylinder is higher than that theoretically calculated (fig.3).

The ratio between the calculated deformation and real deformation in the inner area is approximately 0.9 and changes as the overall deformation increases. Due to this fact it is necessary to calibrate the flow curve obtained. [13] A calculated point in the flow curve diagram is for deformation in the inner area. So there are two possibilities; adjusting the deformation rate or adjusting the flow stress. This problem is the only reason for using the numerical method.

$$\sigma_f = \left[\frac{4(F_{all} - F_{st})}{\pi d_{in}^2} - \sigma_{rr} \right] \cdot \frac{1}{1 + \frac{\mu}{3} \cdot \frac{d_{in}}{h_{cil}}} \quad (4.)$$

σ_f - flow stress of MMC
 F_{all} - total load on the cylinder and ring
 F_{st} - load on the steel ring
 d_{in} - inner diameter of the steel ring
 σ_{rr} - radial pressure on the MMC cylinder
 μ - coefficient of friction
 h_{cil} - the height of steel ring and MMC cylinder

In order to calibrate the numerical calculation a cylinder made of the same material as the steel ring was used. In that case the result of the calculation is known, so the coefficient, used later for a real calculation, can be defined (fig.3). If the calculation method were completely accurate, the extracted results of the flow curve would be the same as those input in the simulation programme. It is not the case and so the calibration curve has to be applied.

6. Flow curve of MMC 2124 + 10%SiC

Two different materials were used for experiments. The first one was artificially over-aged (two hours at 275°C) and the second as received not heat-treated. The second one was used to perform the test with high cross-head speed and with low cross-head speed. The difference in flow curves is clear (see Fig.5-7), as the first one is softer. The rate of hardening stays approximately the same regardless the overaging and cross-head speed. There is also the development of the hydrostatic pressure presented on the first diagram. The results are of a great help to the tool maker because the tools have to be constructed in

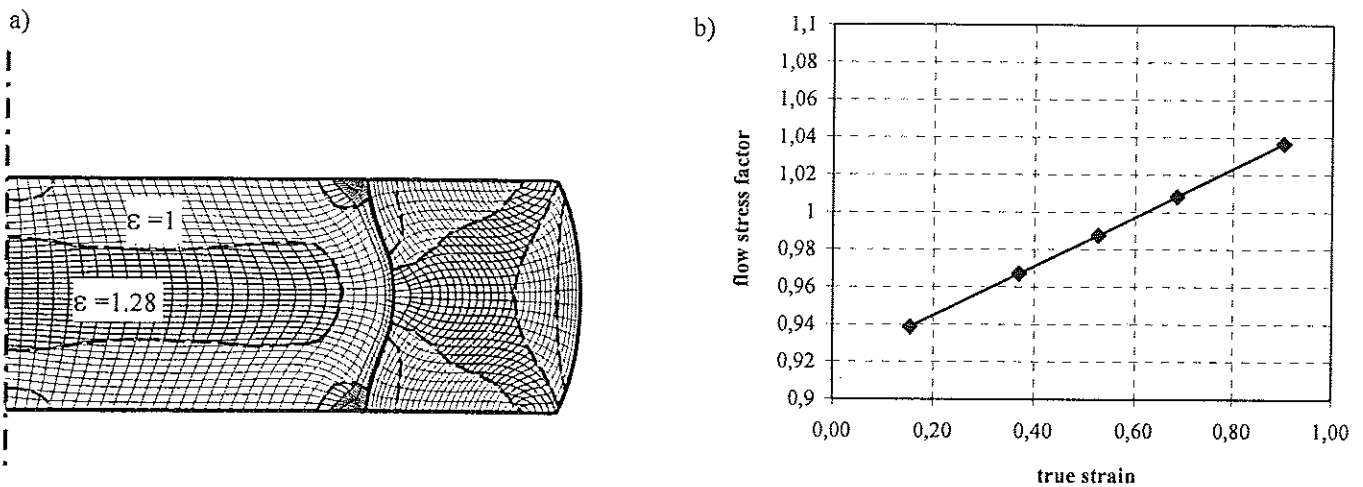


Fig 3: a) Numerical simulated strains (the strains are higher at the centre of the cylinder because of friction)

b) Calibration curve used for the calculation of the flow curve

such a way that they induce enough hydrostatic pressure to the MMC. If it is possible to establish the prescribed hydrostatic pressure at a certain true strain, than we can believe that the work material would not crack.

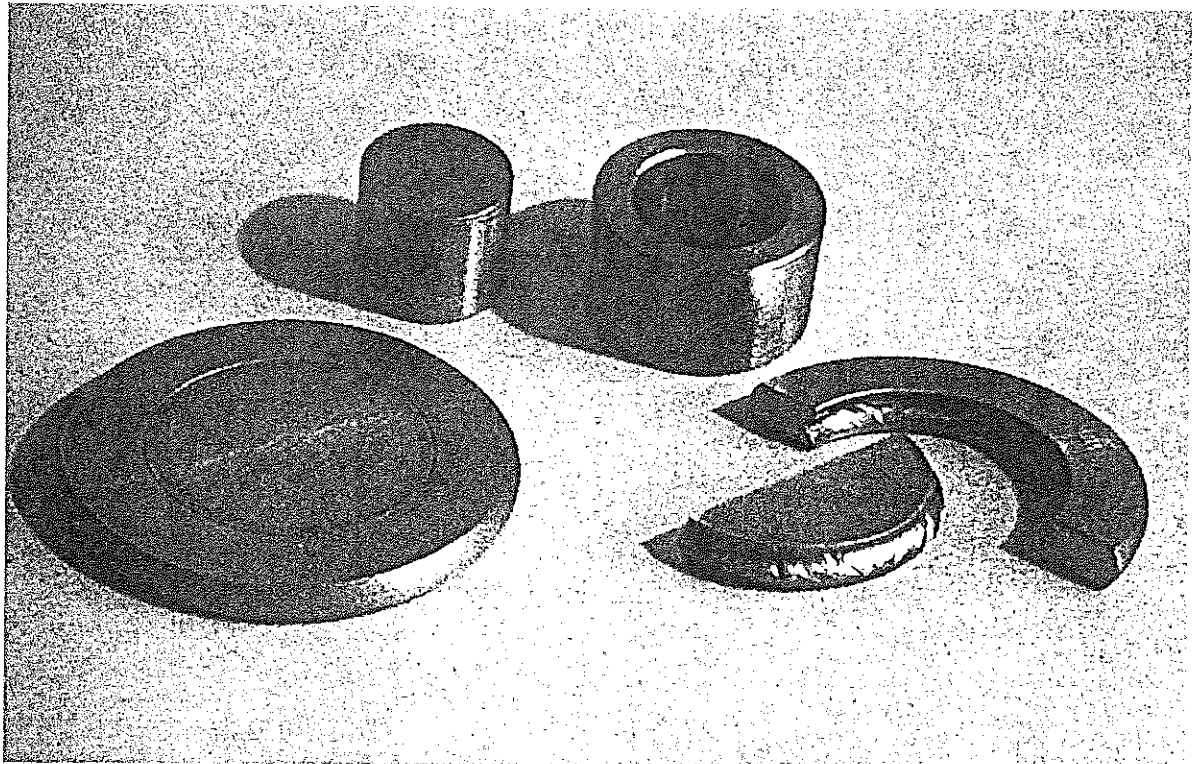


Fig 4.:Cracks on the outer surface of the cylinder

It is also interesting to compare the forming force at high cross-head speed and at low cross-head speed. It is higher in the first case when forming slower. The explanation for this phenomenon can be found in heat generation during forming. When the speed is slow, the system is approximately isothermal, which is not the case at forming with high cross-head speed. We have to consider in this case that the system is quasi-adiabatic and the heat generated stays within the specimen and causes the temperature rise up to say 200 °C [14]. The increase in temperature causes the material to become softer which reflects in the lowering of the forming force.

Combined flow stress for the system MMC - steel at high strain rate is presented in the fig.8-9 (upsetting on a mechanical press). It is assumed in the calculation as to have the cylinder and ring made of the same material. It was made just to show that due to temperature rise the flow curve of the system falls.

If the flow curve for steel at high cross-speed is calculated, one can realise that the material is much softer then in slow speed forming. Further calculations and results show that lower forming forces at high cross-head speeds are a consequence of lowering the steel ring flow stress, while the flow stress of aluminium stays approximately the same. But together, when coupled in the system ring-cylinder their forming resistance is lower.

It can be concluded that this kind of material forming, on this press, under such conditions, require such forming capabilities. Many more experiments should be completed in order to gain a more general picture about forming of MMCs under industrial conditions.

It is interesting to compare the experimental results with numerical simulations at the end, though the whole idea is to combine both methods. The experimental work supported with proper numerical simulation gave important results. The problem which remains through

the experiments is the development of tensile stresses at the outer surface of the cylinder. Despite the presence of the ring there is a small region of tensile tangential stress present in the cylinder. In the experiments there are some small cracks on the outer surface but they are limited to a small area (Fig.4).

The simulation and experiments coincide very accurately. But the wish was to use simulation as a numerical tool to the problem. The program input parameters were varied until that both results (numerical and experimental) were identical.

7. Conclusion

A measuring method for evaluation of the flow curve for brittle composite materials is presented. The plastic strain obtained was 1.2 which is high. For forming of such materials it is necessary to control the stress state in such a way as to have the tensile stressed regions of the specimen as small as possible. Superimposing a hydrostatic pressure on the basic stress state makes those conditions possible. The problem in this case is a higher forming force. It is also to form these brittle materials with high cross-head speeds. It is only important to establish enough hydrostatic pressure to avoid the material cracking.

The friction coefficient plays an important role in developing the hydrostatic pressure. For forming of brittle materials it is sometimes better to keep the friction at a high level in order to produce as much additional pressure as possible. Tool and forming process design (including die speed) should be carried out in such a way to ensure such a stress state.

This is a novel technique for plastic forming of brittle MMCs without prior heat-treatment and requires only high superimposed hydrostatic pressure. It is possible in principle, to apply this technique to any brittle MMC, or indeed any other brittle material.

It is an interesting feature of these experiments that the total forming force decreased with increasing cross-head speed; this shows an industrial advantage to using impact die speeds because of the resulting quasi-adiabatic heating in the work-piece.

Further work is necessary on the combined effects of elevated strain rate and high superimposed hydrostatic pressure on the forging process to optimise these conditions.

References

- [1.] T. W. Clyne and P. J. Withers, "An Introduction to Metal Matrix Composites", pp. 509, 1993, C. U. P.
- [2.] L. Luo, Z. Ling, J. Jiang and B. Dodd, "Effects of Microstructure on the Fracture Al-2124/SiC_p Composites", pp. 7.1-7.5, 1993, Proc. 8th DYMAT Technical Conference, Ispra, Italy.
- [3.] Z.Kampuš, J.Jiang, B.Dodd, Net shape cold plastic forming of aluminium-based metal matrix composites, J. Mat. Sci. Letters 13 (1994) 80-81,
- [4.] J. Jiang, B. Dodd, E. Sellier and Y. Le Petitcorps, "Large Cold Plastic Deformation of Metal-Matrix Composites Reinforced by SiC Particles", pp. 1519-1521, vol. 12, 1993, J. of Mat. Science Letters.
- [5.] B.Dodd and Y.L.Bai, "Ductile Fracture and Ductility", pp.310, 1987, Academic Press Inc(London) Ltd.
- [6.] L. Luo, J. Jiang and B. Dodd, "The Deformation Mechanism and Formability of a Metal Matrix Composite--- Al-2124/SiC_p", pp. 311-315, 1994, Proc. Int. Symposium on Advanced Materials for Lightweight Structures, ESTEC, Noordwijk (ESA-WPP-070)
- [7.] J. Jiang, Z. Kampus and B. Dodd, "A Study on the Cold Plastic Formability and Fracture Behaviour of Particle Reinforced Metal Matrix Composites", pp. 665-672, 1995, Key Engineering Materials, Trans Tech. Publications.
- [8.] K. Lange, Handbook of metal forming, Mc Graw Hill, 1985
- [9.] J. Jiang and B. Dodd, "Workability of Aluminium-based Metal Matrix Composites in Cold Compression", pp. 62-66, vol. 26, 1995. Composites

- [10.] T. von Karmen, "Festigkeitsversuche unter allseitigem Druck", pp. 1749-1757, vol. 55, 1911, Zeitschrift des Vereins deutsche Ingenieure
- [11.] Y Le Petitcorps, B. Guillaume, J. Jiang and B. Dodd, "Forgeage de Précision de Matériaux Composites a Matrice d'Alliage d'Aluminium" Matériaux et Techniques pp. 23-28 No 3-4 1999.
- [12.] P. W. Bridgman, "Studies in Large Plastic Flow and Fracture", pp. 362, 1952, McGraw-Hill Book Co.
- [13.] Pöhlandt, Mechanical Testing for Metal Forming Applications, Springer-Verlag, 1986
- [14.] Y. L. Bai and B. Dodd, "Adiabatic Shear Localization", pp.378, 1992, Pergamon Press

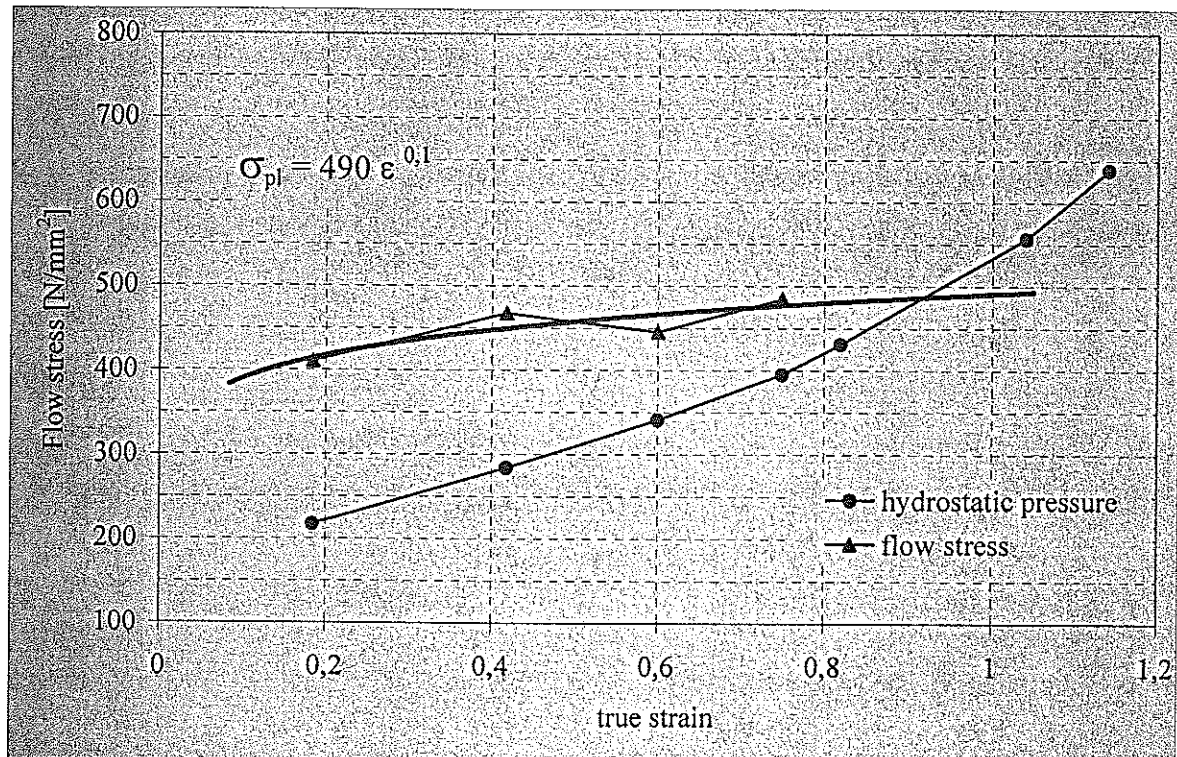


Fig 5.: Flow stress of the heat-treated MMC

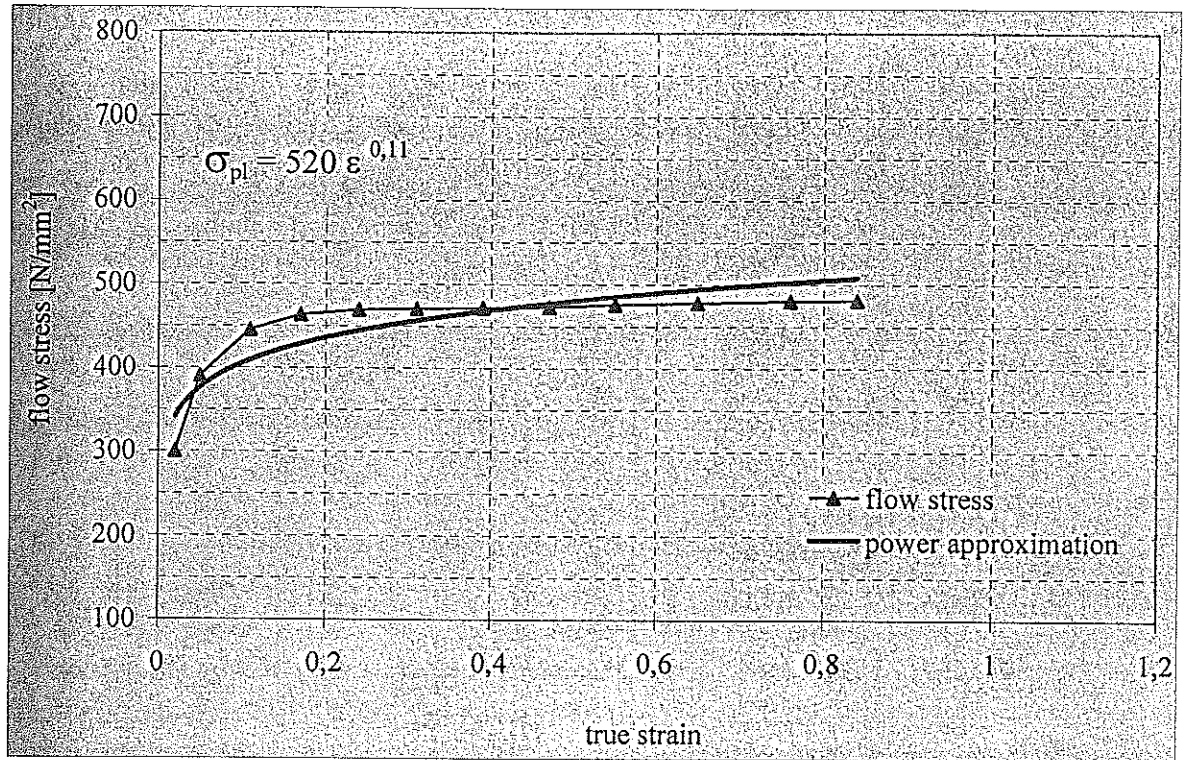


Fig 6.: The flow curve for non heat-treated MMC at high cross head speed ($v=20$ mm/sec)

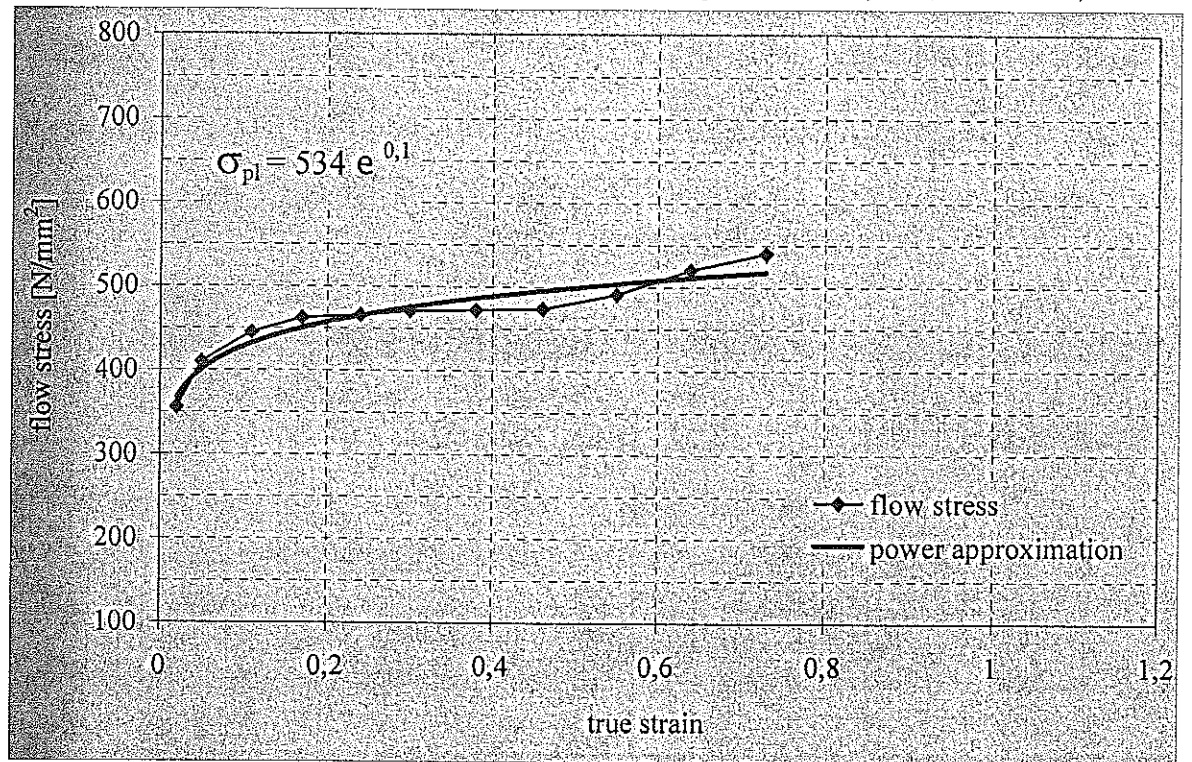


Fig 7.: The flow curve for non heat treated MMC at high cross head speed ($v = 0,02$ mm/sec)

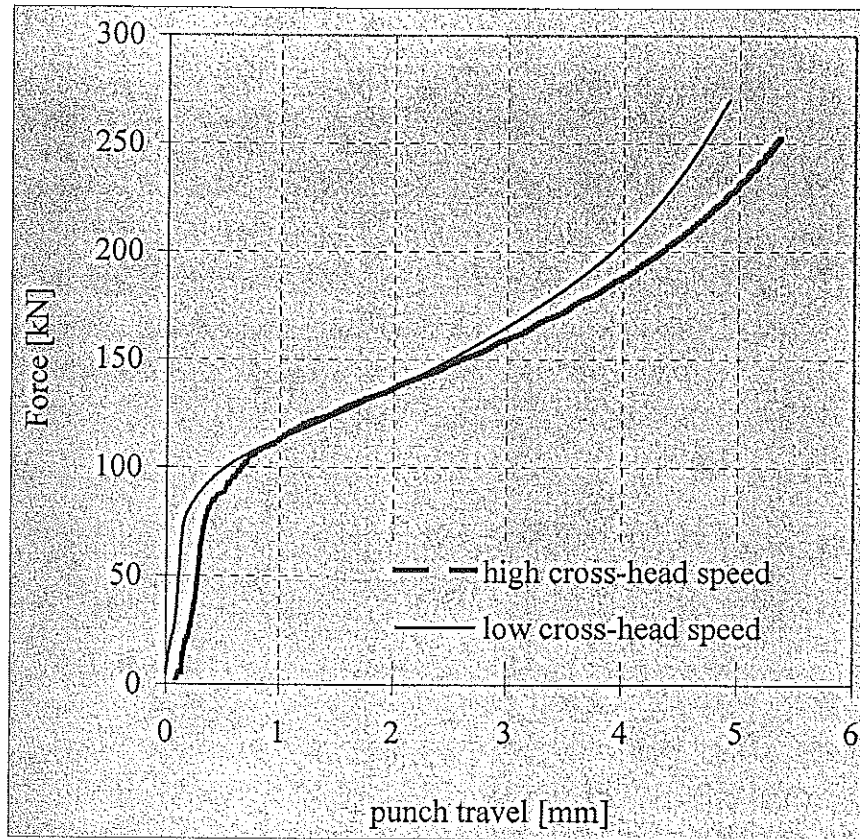


Fig 8.: Forming force at slow and fast cross-head speed

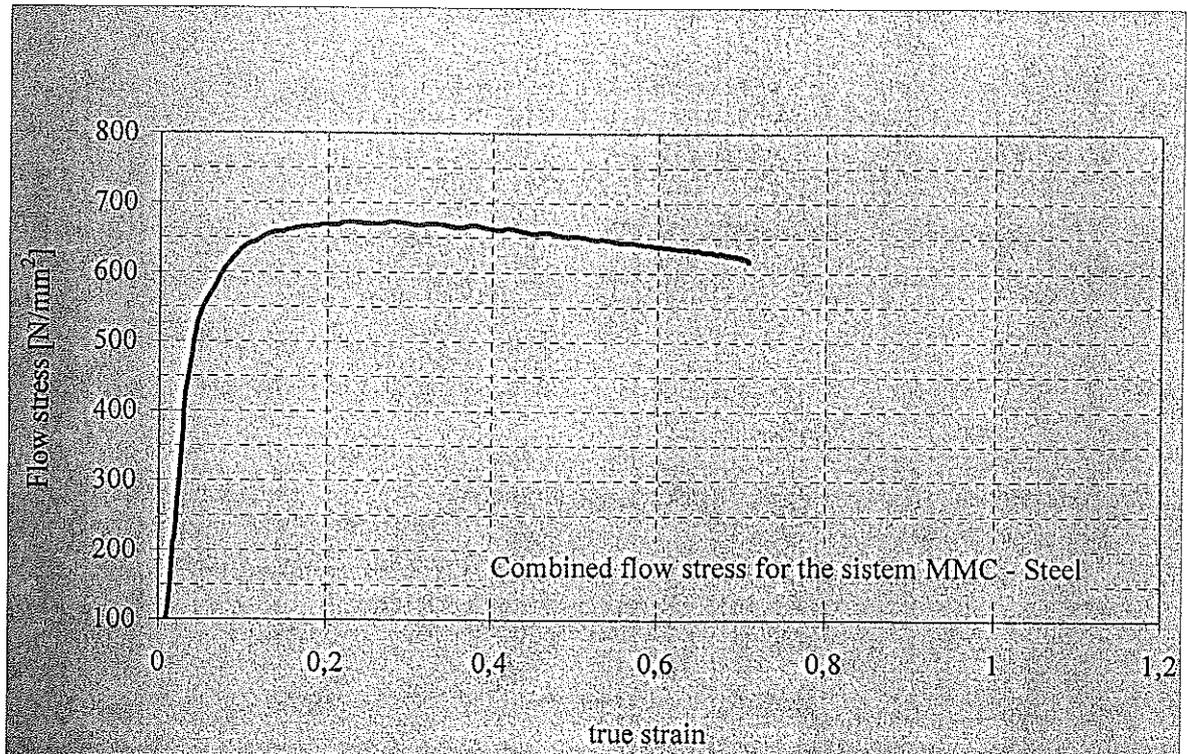


Fig 9.: The decrease of flow stress as the reason for material heating

INTERACTION OF L/D=4 WHA PROJECTILES WITH GRP TARGETS AT 1500 M/S

F. Rondot

ISL, French-German Research Institute of Saint-Louis, 68301 France

This paper deals with results of a computational and experimental investigation on the behavior of glass fiber reinforced plastic (GRP) impacted by tungsten heavy alloy (WHA) projectiles.

Using a powder gun, cylindrical projectiles (mass 28 g) were fired at striking velocities around 1500 m/s against inclined GRP plates. In a parallel way, oblique impact was simulated using the erosion algorithm implemented into the Lagrangian finite element code LS-DYNA.

It came out that the response of the composite material under investigation, for this particular impact loading, could be predicted in good agreement with experiments without need for a complex orthotropic constitutive law. This was principally true with regard to the residual projectile main features (length, velocity). Nevertheless, efforts are still to be focused on improving the behavior description of such materials, to model for instance the possible deflection of the projectile due to delamination of the composite modulus.

INTRODUCTION

Numerical solution techniques have advanced to the point where numerous calculations in the field of terminal ballistics can be performed as a matter of routine on current wave propagation computer codes, popularly known as hydrocodes. Nevertheless, due to their heterogeneity, behavior of composite materials still remains a challenge for code user.

In this paper, results of a computational and experimental investigation on the behavior of glass fiber reinforced plastic (GRP) impacted by tungsten heavy alloy (WHA) projectiles at 1500 m/s are exposed. For comparison with experiments featuring woven GRP inclined plates, hydrocode calculations were carried out using the Lagrangian finite element code LS-DYNA [1].

TEST RESULTS

A series of experiments was conducted to investigate the interaction of WHA projectiles with woven GRP targets. Using a powder gun, several projectiles were fired at striking velocities around 1500 m/s against inclined GRP plates. Aerodynamic stabilization of the projectile was ensured with an aluminum alloy flare. Two types of targets were investigated: a single inclined composite modulus and a plate with a XC 48 mid-steel back casing (196 HV30). The lateral dimensions were 100x300 mm². Projectile velocity was measured by two laser

light barriers. Flash X-radiographs were taken prior to impact to determine the inclination of the projectiles and during the penetration process to obtain terminal diagnostics. Figures 1 and 2 illustrate the projectile design and the composite modulus. Projectiles are cylinders made of DX2-HCMF alloy supplied by *Cimé-Bocuze*. Density is 17.6 g/cm^3 and hardness is 420 HV30. The ratio between the length and the diameter of the cylinder is $L/D=4$. The mass is approximately 28 g. Target material is an E-Glass fiber reinforced Polyester matrix. The density is 2 g/cm^3 . Figure 2 exhibits the taffeta weaving.

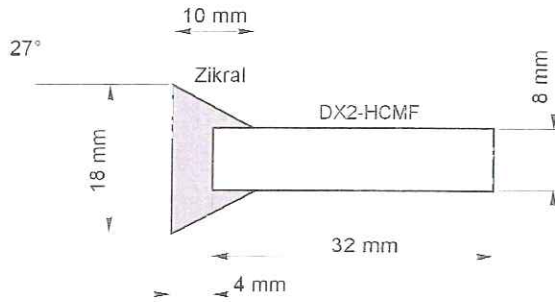


Figure 1. L/D=4 WHA projectile

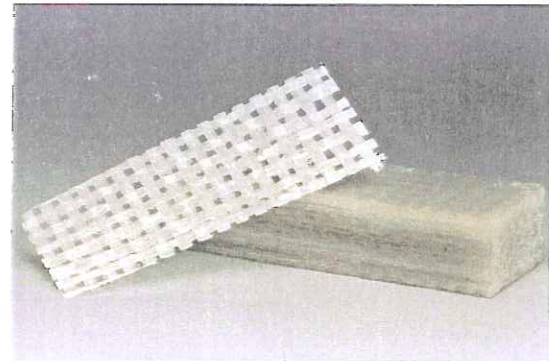


Figure 2. GRP specimen

Representative experimental results are reported in Table 1 where V_i , L_r and V_r are respectively the impact velocity, the residual length and the residual velocity of the projectile after perforating the target. Examples of X-ray pictures and recovered targets are given in Figures 3 and 4.

Table 1. Examples of test results

Target	Layers	Obliquity	V_i (m/s)	V_r (m/s)	L_r (mm)	Comments
T1	55 mm GRP	45°	1490	930	19-20	back delamination, tumbling, trajectory deviation
T2	44 mm GRP	55°	1490	920	19	back delamination, tumbling, trajectory deviation
T3	35 mm GRP	65°	1500	930	20	back delamination, tumbling, trajectory deviation
T4	22 mm GRP	75°	1510	910	20-21	back delamination, tumbling, trajectory deviation
T5	22 mm GRP	60°	1510	/	22	total delamination, tumbling
T6	22 mm GRP 2 mm Steel	60°	1480	1060	19	no delamination, tumbling
T7	22 mm GRP 4 mm Steel	60°	1520	950	15-16	no delamination, tumbling

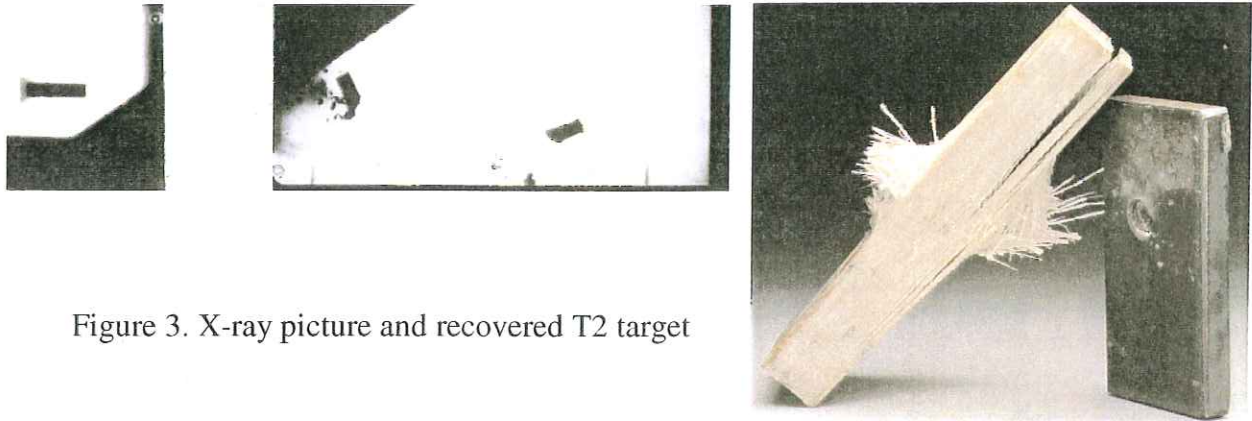


Figure 3. X-ray picture and recovered T2 target

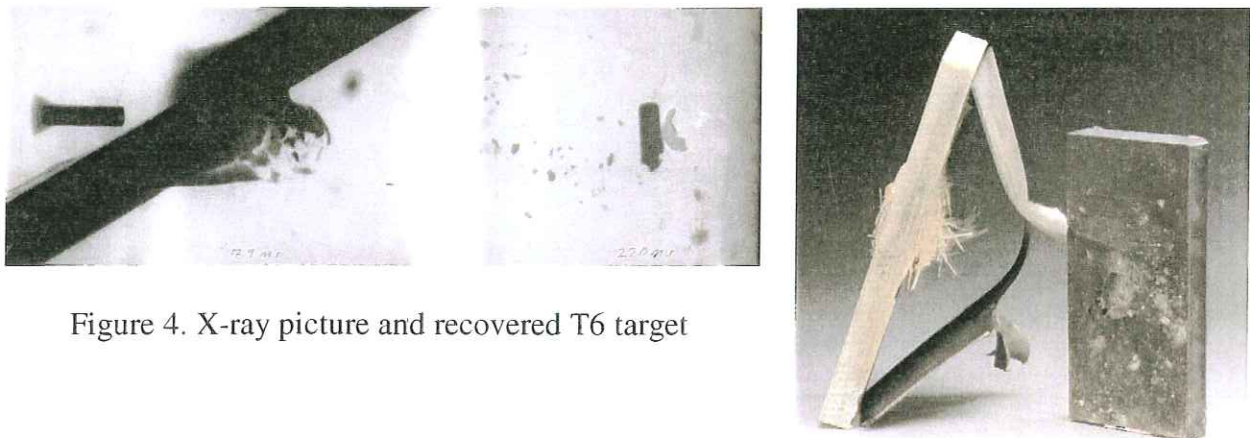


Figure 4. X-ray picture and recovered T6 target

NUMERICAL SIMULATIONS

Hydrocode calculations were carried out using the erosion algorithm implemented into the Lagrangian finite element code LS-DYNA [1]. Oblique impact of the projectile was simulated using a 1-mm square constant mesh size for the region of most interest ("contact zone"). Beyond this strong interaction region, the target is coarsely meshed. A "tied with offset" interface was used to connect these two parts. Interactions between the aluminum flare, the WHA body and the target were treated using "eroding surface to surface" contacts. WHA, aluminum alloy and mid-steel were modeled using a Mie Grüneisen equation of state and an elastic-perfectly-plastic constitutive law, based on the Von Mises yield criterion. Constant yield strength was respectively 1600 MPa, 400 MPa and 650 MPa. To start with a simple approach and according to previous published results [2], GRP was treated as an isotropic material with an equivalent yield strength of 400 MPa. Equations of state parameters were taken from the home material library.

Lagrangian hydrocode achieves penetration by a user defined erosion strain, i.e. strain required for an element to be deleted. This critical value determines when an element is thought to no longer contribute to the penetration process. Erosion strains of 2.5, 1.0 and 1.0 have been used in the WHA projectile, the aluminum flare and the GRP target respectively. Different steps of the perforation process are illustrated by Figure 5 for T7 target. Examples of correlation between predictions and tests are illustrated in Figure 6. Representative results of numerical simulation are listed in Table 2, using the same denomination as previously.

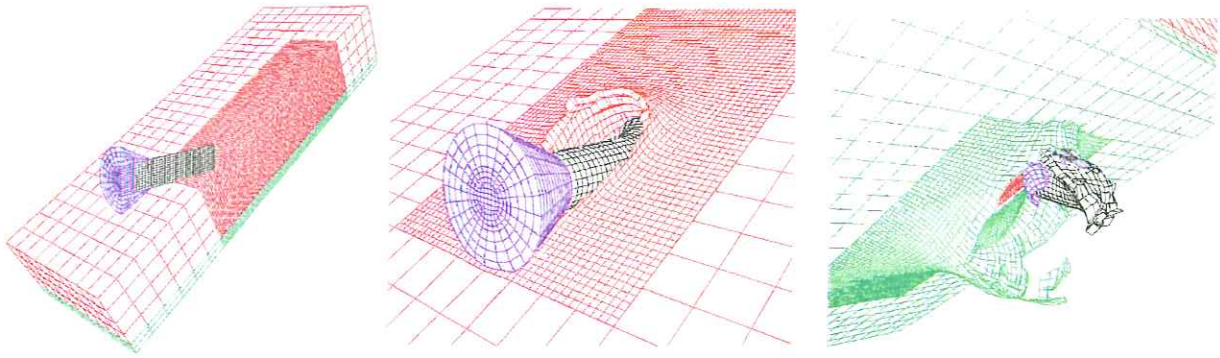


Figure 5. T7 target: (a) Initial mesh. (b) 20 μ s after impact. (c) 80 μ s after impact.

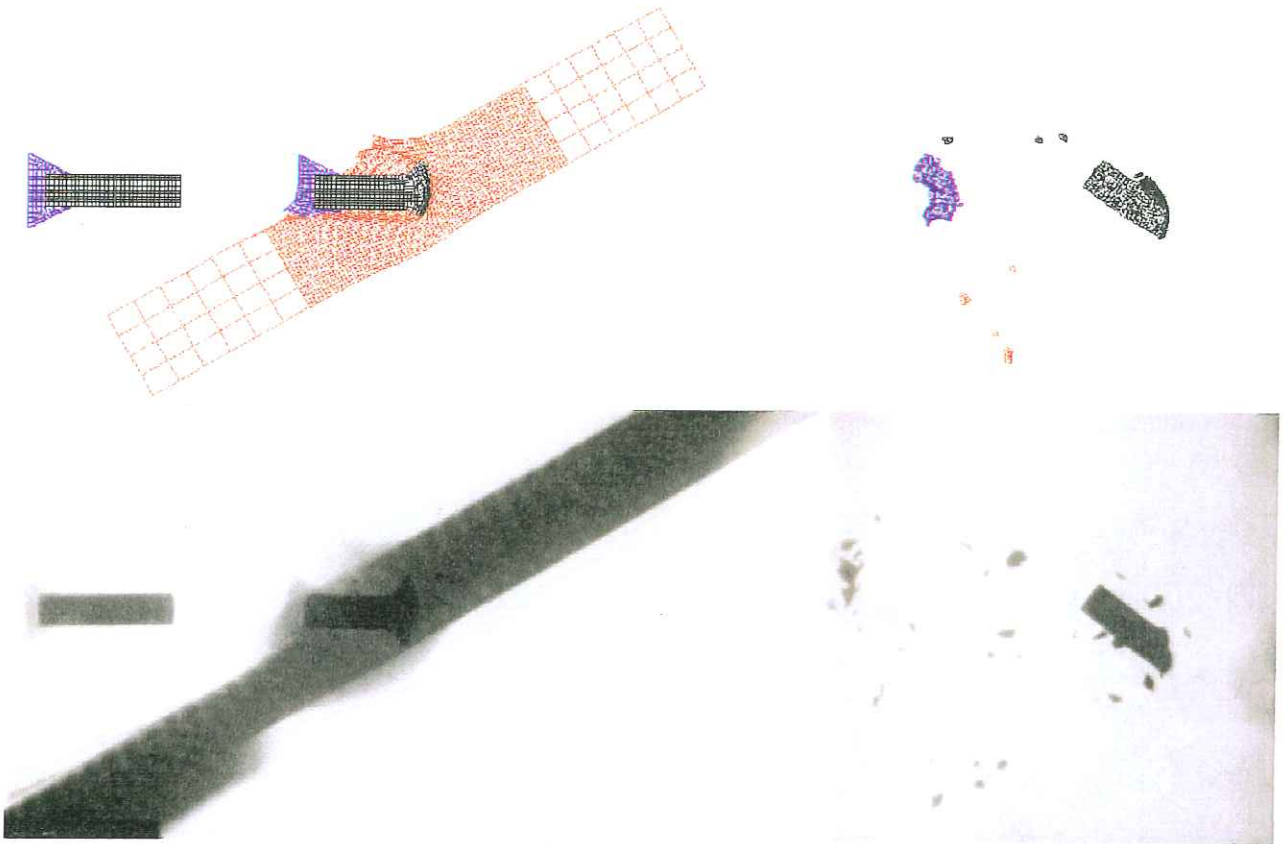


Figure 6. Hydrocode prediction compared to X-ray pictures - T5 target
Prior to impact, 25 μ s after impact, and 185 μ s after impact

Table 2. Examples of numerical simulation results

Target	V_i (m/s)	V_r (m/s)	L_r (mm)	Comments
T2	1500	910	18-19	tumbling
T5	1500	1170	22	tumbling
T6	1500	1070	18	tumbling
T7	1500	990	15	tumbling

DISCUSSION

The computational results are coherent and show a good quantitative agreement with experimental data. Even a very simple approach using an isotropic constitutive law can give satisfactory results. This confirms some published conclusions [2]. Moreover, use of a complex orthotropic law is often liable to debate on account of a lack of set of parameters [3].

Generally, a rotational impulse (so-called tumbling) is induced by the perforation of an inclined plate, because of opposed forces that act at the instantaneous projectile tip during the plate entrance and exit phase. The projectile head is deflected in the direction of the target plate normal, but the center of mass is still moving in the direction of the original trajectory. From Figures 5 and 6, it can be seen that the stabilization flare hits the side wall of the front face hole, what tends to emphasize this rotational impulse of the projectile.

As it can be observed on X-ray picture of Figure 3, the trajectory of the projectile was also deflected about 10° towards the normal vector of the plate exit face. This may be due to the delamination (through the thickness) of the composite modulus, not supported by the current simulations. It is noteworthy that this experimentally observed delamination is localized at the back part of the target.

No trajectory deviation occurred with T5 target (see Figure 5). It has to be mentioned that the width of the composite plate tested was reduced to permit visualization of the penetrating projectile through the modulus. This led to the total delamination of the composite: delamination through the thickness and delamination from the edges. Calculated residual velocity of the projectile cannot be compared with experimental value because only one picture was taken of the residual projectile after perforation of the target (most of the time, three radiographs were taken: one before the impact and two after, at intervals around 140 μ s).

When the back face of the modulus is supported by a steel plate, the initial trajectory of the projectile is no more deflected. Emerging residual projectile just tumbles (see Figure 4). This phenomenon is analogous with perforation of a single steel plate [4]. Recovered composite modulus is no more delaminated. Here again, the computational predictions are coherent and show a satisfying quantitative agreement with trials.

Qualitatively, the phenomenology of delamination has been studied in extensive [5-8]. But undertaken studies have to be carried on for a complete predictive aspect of the numerical simulations [9-15].

CONCLUSIONS

A series of experiments and hydrocode simulations was conducted to study the behavior of woven GRP inclined plates against WHA cylindrical projectiles at 1500 m/s. It came out that the impact response of the composite material under investigation, for this particular impact loading, could be predicted in good agreement with trials, without need for a complex orthotropic constitutive law. This was principally true with regard to the residual projectile

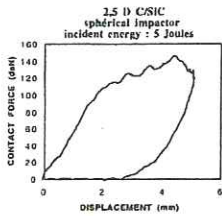
main features (length, velocity) and when the composite modulus is supported by a metallic plate. Nevertheless, efforts are still to be focused on improving the behavior description of such materials, to model for instance the possible deflection of the projectile, due to the delamination of a single inclined composite modulus. Finally, one has to keep in mind that discrepancies are sometimes obtained with composite materials when comparing two supposed reproducible experiments. Another crucial point is the scaling effect of impact damage [16]. Extrapolation of laboratory reduced scale tests is then hazardous.

REFERENCES

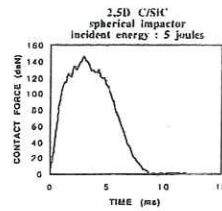
- [1] "LS-DYNA Keyword User's Manual - Version 950", LSTC Report, May 1999.
- [2] C. Cazeneuve, "Comportement dynamique de composites", Journées Matériaux ETCA, pp. 333-345, Arcueil, 16-17 septembre 1986.
- [3] P. Mariotti, G. Paziienza, G. Pedrotti, "Experimental and Theoretical Studies on Impact of Fragments Against Composite Plates", MAT-TEC 91, pp. 356-371, Paris, October 07-11 1991.
- [4] F. Rondot, "Performance of Tantalum EFP Simulants", 17th International Symposium on Ballistics, Midrand South Africa, March 23-27, 1998, ISL PU 329/98.
- [5] C.Y. Chiem, "Wave Propagation in Composites and High Strain Rate Interlaminar Shear of Composites", COMETT, Lecture notes for the International Summer School on Dynamic Behaviour of Materials, ENSM, Nantes, September 11-15 1989.
- [6] J. Harding, "Impact Mechanical Behaviour of Fibre Reinforced Composites", COMETT, Lecture notes for the International Summer School on Dynamic Behaviour of Materials, ENSM, Nantes, September 11-15 1989.
- [7] J.L. Lataillade, J. Pouyet, S. Sahraoui, "Polymères et composites : sollicitations dynamiques", 5^{ème} colloque Mécanique et Métallurgie, Tarbes, 14-16 mars 1984.
- [8] R.H. Zee and C.Y. Hsieh, "Energy Loss Partitioning During Ballistic Impact of Polymer Composites", Polymer Composites, Vol. 14, No. 3, pp. 265-271, June 1993.
- [9] C. Bathias, "La rupture des matériaux composites à hautes performances", La Revue de Métallurgie-CIT/Science et Génie des Matériaux, pp. 241-251, Février 1995.
- [10] C.T. Sun and S.V. Potti, "Modelling Dynamic Penetration of Thick Section Composite Laminates", AIAA-95-1203-CP, pp. 383-393, New Orleans, April 10-13 1993.
- [11] M. Pilling and S. Fishwick, "The Application of Progressive Damage Modelling Techniques to the Study of Delamination Effects in Composite Materials", 6th European Conference on Composite Materials, pp. 269-274, Bordeaux, 1993.
- [12] L.T. Kisielwicz and E. Haug, "An Intrinsic and Objective Engineering Equation of State for Composite Materials Accounting for Damage and Rupture", 4th International Offshore and Polar Engineering Conference, pp. 182-191, Osaka, April 10-15 1994.
- [13] D. Schaeffer, "Simulation Numérique du comportement et de la rupture des solides composites ou homogènes", Revue du GAMI, Mécanique Industrielle et Matériaux, Vol. 48, N° 3, pp. 140-143, Septembre 1995.
- [14] T. A. Bogetti, C.P.R. Hoppel, B.P. Burns, "LAMPAT: A Software Tool for Analyzing and Designing Thick Laminated Composite Structures", ARL-TR-890, September 1995.
- [15] T. A. Bogetti, C.P.R. Hoppel, W. H. Drysdale, "Three-Dimensional Effective Property and Strength Prediction of Thick Laminated Composite Media", ARL-TR-911, October 1995.
- [16] S.R. Swanson, "Scaling of Impact Damage in Fiber Composites", Workshop on Scaling Effects in Composite Materials and Structures, NASA Langley Research Center, pp. 245-264, July 1994.

LOW-ENERGY IMPACT ON 2,5 D C/SiC CERAMIC MATRIX COMPOSITE

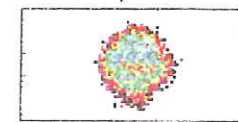
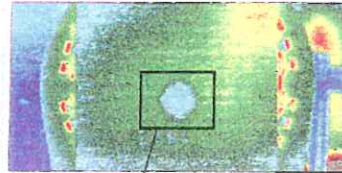
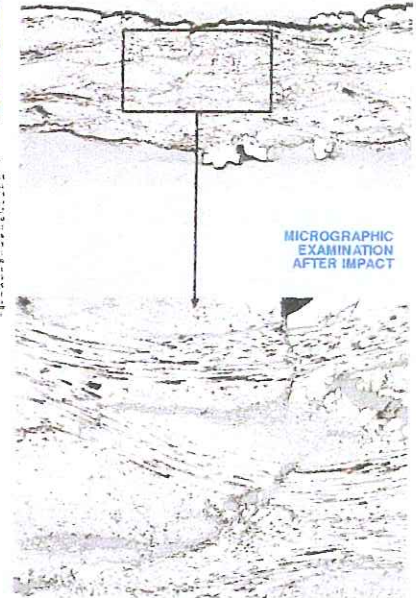
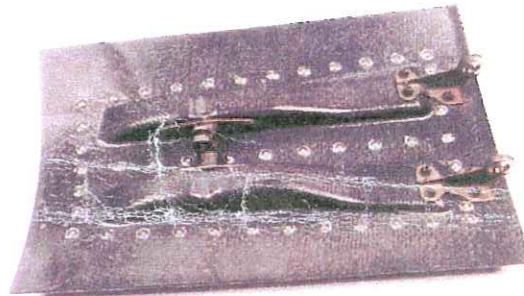
Ch. Marfaing



Contact force-displacement curve



contact force-time curve

INFRARED THERMOGRAPHY
AFTER IMPACTMICROGRAPHIC
EXAMINATION
AFTER IMPACT

MILITARY AIRCRAFT ENGINE OUTER FLAP

- **2,5 D C/SiC**
Military aircraft engine outer flaps can be subjected to low energy impacts (e.g. dropped tools used during maintenance).
- **THERMAL CYCLING BEFORE IMPACT**
To evaluate the in-service tolerance to impact of a 2,5D C/SiC, thermal cycles were applied to represent thermal stresses in aircraft.
- **DROP WEIGHT IMPACT RIG**
-incident energy range : 1 to 45 joules (N.m)
-impact velocities : 0,94 to 4,5 m.s⁻¹
-various impactors and different methods (plane, simple and cantilever supports)
-contact force, impact energy and displacement acquisition data during impact.
- **ANALYSES AFTER IMPACT**
-Infrared thermography tests
-micrographs and residual bending
- **RESULTS**
For a CMC, the 2,5D C/SiC impact behaviour is acceptable.
Only the impacted zone is damaged.
There is no delamination outside this local zone.
Thermal cycles (200°C to 600°C of 4 min.) during 240 hours were applied to the specimens before impact.
These cycles result in a contact force and displacement decrease of 50%.

CEAT - 23 AVENUE HENRI GUILLAUMET - 31056 TOULOUSE CEDEX - FRANCE
TEL : + 33 (0)5 61 58 71 00 - FAX : + 33 (0)5 61 58 71 79



DGA/CEAT - REI - Service infographie - 1999

A HYBRID METHOD BASED ON AN APPROACH TO PSEUDO-DYNAMIC TECHNIQUES IN THE DYNAMIC ANALYSIS OF PIPING STRUCTURES

F. Q. de Melo, J. O. Carneiro, H. R. Lopes, J. D. Rodrigues,
J. F. Silva Gomes

Experimental Mechanics and New Materials Research Unit
FEUP, Faculty of Engineering of the University of Porto
Rua dos Bragas, 4099 Porto Codex Portugal

Abstract

An alternative method for the linear elastic dynamic analysis of piping systems using a sequential procedure is described. In a first step, a numerical dynamic analysis of the structure is carried out with a finite element modelling. A displacement vector referred to a given time step is then obtained. This displacement vector, eventually corresponding to the largest amplitude of a time variable motion, assigned to a structure node or set of nodes, is prescribed to a test specimen, which is a detail of a piping structure. This test specimen is mounted in a test rig equipped with a set of precision actuators, prescribing the computed displacement field. This methodology makes possible to investigate the stress distribution in some geometric details of the test specimen, which may be difficult and expensive to model in the finite element problem. Assuming a linear elastic analysis, the maximum measured stress level, which must be lower than the material yield stress, will set the maximum allowable amplitude of the motion to the structure calculated by a scale factor. The here described method does not follows the procedure of pseudo-dynamic techniques.. Details concerning the main differences between the method presented here and the pseudo-dynamic techniques are discussed in the text.

1 – Introduction

Due to the broad industrial applications of piping systems, their design must consider the presence of dynamic loads, even in those cases where variable force generator sources are not part of the structure. The seismic loads are an important item always included in the design specifications. Usually, a seismic disturbance is numerically simulated at the level of supports or rigid equipment fitted to the piping system. Having modelled the piping structure by a finite element method for example, a seismic analysis may be modelled by prescribing a time-variable displacement on selected supports. The presence of a time-variable force resulting from the presence of a dynamic load generator source may be also carried out by prescribing it on selected nodal points.

The work presented here is based on only a part of the whole procedure of pseudo-dynamic techniques. These techniques consists essentially in a combined numerical and experimental iterative scheme, where prescribed displacements coming from a first step lead to the measurement of forces at the level of the degrees of freedom of the structure; such forces are input in the numerical iterative algorithm for the integration of the dynamic equation, giving rise to a new deformation step (Pinto *et al*, (1992), (1994), (1994a), (1994b), (1995), (1995a)). The present procedure does not measures the reactions from prescribed variables, limiting its application field to linear problems only. However, the

method appears as a promising research tool, reliable and accurate, provided that the mechanical properties of the structural parts do not change during the tests.

2 - Analysis of the structure response to transient disturbances with the modified Newmark method.

The essential procedure for the method consists on following the Newmark method (Newmark (1959)), where the convergence to the solution is unconditional. This does not mean, however, that an accurate solution is always obtained. One starts from equation (1), referred to the time-step $t+\Delta t$:

$$[\mathbf{K}]\mathbf{U}_{t+\Delta t} + [\mathbf{C}]\dot{\mathbf{U}}_{t+\Delta t} + [\mathbf{M}]\ddot{\mathbf{U}}_{t+\Delta t} = \mathbf{F}_{t+\Delta t} \quad (1)$$

where (·) and (··) represent, respectively, the first and the second time derivatives; $[\mathbf{K}]$, $[\mathbf{C}]$ and $[\mathbf{M}]$ represent the global stiffness, damping and mass structure matrices, resulting from the discretization in a set of elements. In the present analysis, the damping was not considered. This assumption leads not only to more simple solution methods but also warrants conservative design procedures.

The final iterative expression gives the acceleration at the time step $t+\Delta t$:

$$\left(\frac{\Delta t^2}{4} [\mathbf{K}] + [\mathbf{M}] \right) \ddot{\mathbf{U}}_{t+\Delta t} = \mathbf{F}_{t+\Delta t} - \Delta t [\mathbf{K}] \dot{\mathbf{U}}_t - \frac{\Delta t^2}{4} [\mathbf{K}] \ddot{\mathbf{U}}_t \quad (2)$$

where $\mathbf{F}_{t+\Delta t}$ is the external force vector. Other values for the velocity and displacement referred to $t+\Delta t$ are easily obtained

3 – Procedure for the hybrid test for dynamic analysis of piping structures

3.1 – Description of the experimental system

A small sized test rig used for the analysis of seismic loads in piping structures is sketched in fig. 1.

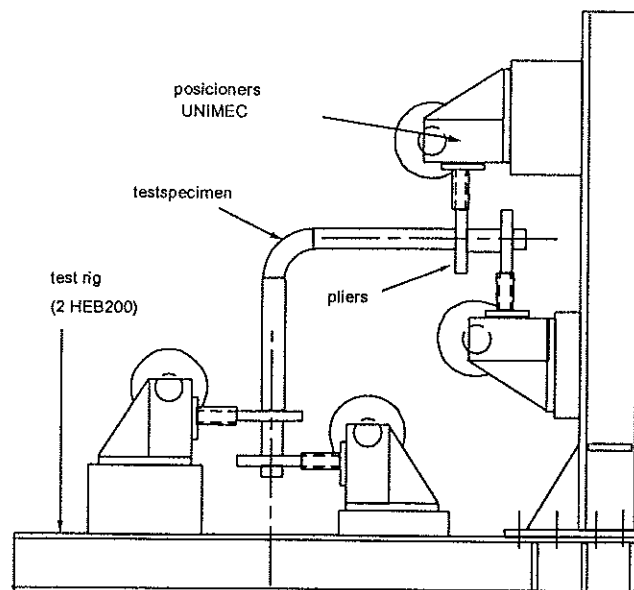


Fig. 1 Test rig for the static analysis equivalent to the dynamic configuration of the structure

The system deals with test specimens forming a part or a detail of a complete piping layout. This rig is fitted with precision actuators positioned at the level of the degrees of freedom considered in the substructure or detail in investigation. Once calculated the displacement vector for a dynamic disturbance corresponding to a time-step, the extreme nodes of the detail are submitted to prescribed displacements and rotations, after the global displacement vector calculation. The process is inexpensive, since very simple beam elements are used to model the curved pipes, considering that the pipe flexibility factor K_α , (Thomson (1980)) is used to evaluate an equivalent Young modulus for the curved accessories

3.2 – Performing an example. Stress analysis in the curved pipe of the detail using modified stiffness beam (MOSBEAM) finite elements

To model the curved pipe flexibility, the K_α factor was included as a scale factor of the Young modulus. Values for the factor K_α were read from Thomson (1980).

A piping structure sketched in fig. 2 was considered to be submitted to a dynamic harmonic load acting in the far right node along the vertical direction

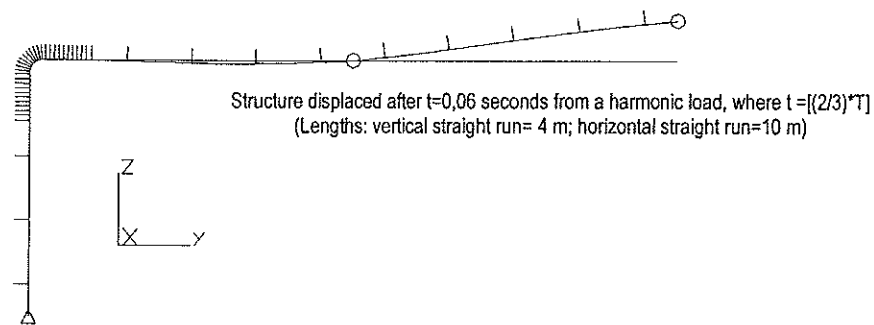


Fig. 2 – a simple piping structure submitted to a dynamic load

Fig. 3 shows the graphical results for the longitudinal membrane stress carried out with the modified stiffness beam elements (for the elbow part) combined with straight beams for tangents.

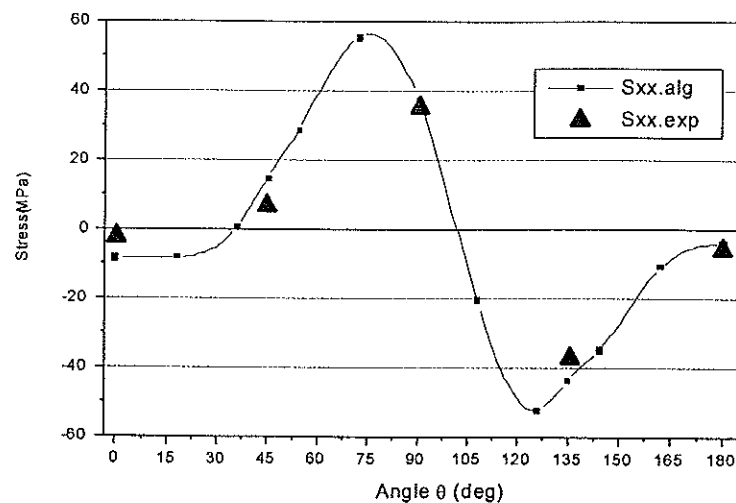


Fig. 3

($S_{xx}.alg$ = longitudinal shell stress from ALGOR at outer pipe surface)
 ($S_{xx}.exp$ = longitudinal Mosbeam stress; experimental at outer pipe surface)

4 – Conclusions and future development

A hybrid method for seismic analysis in civil engineering met here an alternative application, where the dynamic behaviour of piping structures was investigated. Because of its accuracy as well as handling facilities, this method appears to be very promising in structural investigation where dynamic actions. However, limitations are assigned to the present method, as the problems to be studied must be linear and in the elastic field. Also, interferometric techniques coupled to image processing software will be included as an improvement of the in the present technique. Due to the high accuracy of such optical methods, it is foreseen that a high precision tool for structural dynamic analysis will be developed, this involving less powered precision actuators.

5 – References

- Pinto, A., Verzeletti, G., Negro, P. and Guedes, J. (1995) *Cyclic Testing of a Squat Bridge-Pier*, Report EUR 16247 EN, Joint Research Centre (CCR; JRC), Ispra (VA), Italy, June 1995.
- Guedes, J., Pinto, A. (1995a) *Numerical Simulation of the PSD Test on Bridges*, Rep. I-21020, JRC of Ispra (VA), Italy, June 1995.
- Arede, A., Pinto, A. (1994) *Analysis of a 4-Storey R/C Building to be Tested in ELSA - The Influence of Global Modelling Parameters*, Proc. of ERCAD 94, T.U., Berlin, 15-17 June 1994.
- Donea, J. , Jones, P. M. and Pinto, A. (1992) *Technical Note N° I-92-146*, presented in the 2nd Meeting of European Association of Structural Mechanics Laboratories (EASML), JRC of Ispra (VA), Italy, Oct 1992.
- Guedes, J., Pegon, P. and A. Pinto (1994a) *PSD Testing of Bridges - A Numerical Validation Study*, ERCAD 94, T.U., Berlin, 15-17 June 1994.
- Guedes, J., P. Pegon, P. and Pinto, A. (1994b) *PSD Testing of Bridges - A Numerical Validation Study*, ERCAD 94, T.U., Berlin, 15-17 June 1994.
- Newmark, N. M. (1959) *A Method of Computation for Structural Dynamics* ASCE Journal of Engineering Mechanics Division, Vol. 85, pp. 67-94.
- Thomson, G. (1980) *In-Plane Bending of Smooth Pipe Bends* PhD Thesis, University of Strathclyde, Scotland.

Holographic Interferometry Techniques for Dynamic Characterization of Structures

M. A. P. Vaz, F. M. Santos and J. F. Silva Gomes

INEGI/FEUP- Faculty of Engineering, University of Porto
Laboratory of Optics and Experimental Mechanics
E-mail: gmavaz@fe.up.pt

Abstract

Laser interferometry techniques are useful and extremely powerful tools in Experimental Mechanics and non-destructive testing of structures and materials. These techniques are widely used for measuring strains and displacements; to study the static and dynamic behaviour of structures. Being nondestructive, interferometric techniques, are extremely sensitive and can be applied without contact to assess the displacement or strain on the surface of diffuse objects. This means that no mass is added to the structures ensuring, this way, high accuracy in the results. We describe here some application of these techniques to study the dynamic behaviour of structures.

Introduction

Several interferometric techniques are now available for applications in the scope of Experimental Mechanics. Some of them are based on the holographic recording of wavefronts like: holographic interferometry, TV-holography and Shearography. In other cases, conventional interferometers, such as the laser Doppler technique, are used to assess the displacement, velocity or strain in discrete points of the object.

The techniques based on holographic recordings are field techniques that can be applied to measure the displacement or velocity distributions on the objects surface. In these techniques, a laser beam is divided into secondary beams by a beam-splitter. One of them, the object beam, is used to illuminate the object while the other, the reference beam, is oriented directly to the surface of the recording media. The two wavefronts, obtained in such way, are brought to overlap on the surface of the photodetector which can be a photographic emulsion, in conventional holographic interferometry, or a CCD detector in TV-holography and Shearography. The photodetector records the interferometric pattern resulting from the combination of the two coherent wavefronts. By the correlation between holographic recordings made in different situations of the object, it is possible to obtain an interferometric fringe pattern with information about object behaviour [1, 2, 3]. Depending on the way the holograms are correlated each fringe may represent equal displacement or equal amplitude of vibration.

Nowadays the most used technique is based on the CCD recording of the interferometry patterns. Using the electronic media for recording and processing the holograms is possible to build-up compact and reliable systems which can be used for on site measurements directly on the structures. In these systems the correlation between holographic recordings can be performed in three different ways:

- ✓ In real time, a hologram of the unloaded object is recorded and used as reference in a real time comparison with incoming video records of new holograms. This way the deformation of a given object can be followed during several loading cycles.

- ✓ Using correlation by double exposure, two holograms of the object, recorded in two different times, are compared to evaluate the object deformation. This technique can be used with pulsed lasers to record the object deformation between two instants of time and record its velocity spatial distribution. This technique is very useful for studying transient phenomena or reducing the influence of environmental disturbances. One example can be seen in figure 1.

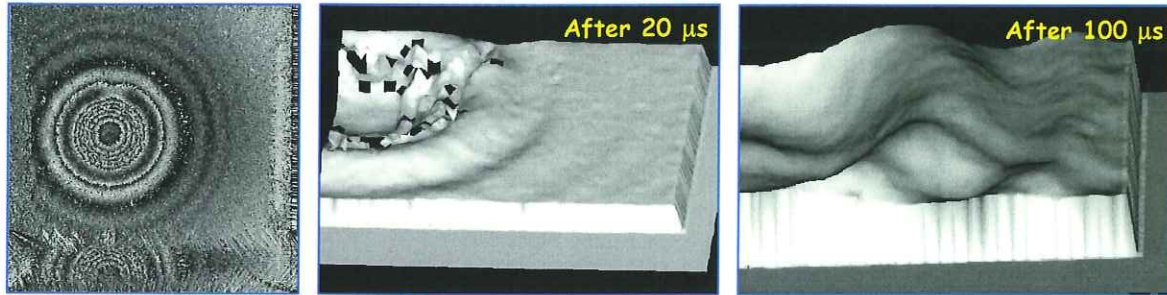


Fig 1 Shock wave propagation on a steel plate –a) phase map 20 μs after impact, b) pseudo 3D presentation of the displacements distribution 20 μs and 100 μs after impact.

- ✓ The correlation can also be performed by time average if a harmonically vibrating object is to be investigated. In this case the hologram is recorded with the object vibrating harmonically in one of its eigen-frequencies. If the exposure time is greater than the vibration period several cycles will be recorded in the same hologram which leads to an interferometric pattern where fringes represent equal amplitude of vibration as shown in figure 2. Sinusoidal phase modulation of the reference beam can be used to improve the measuring capacities of these methods [4].

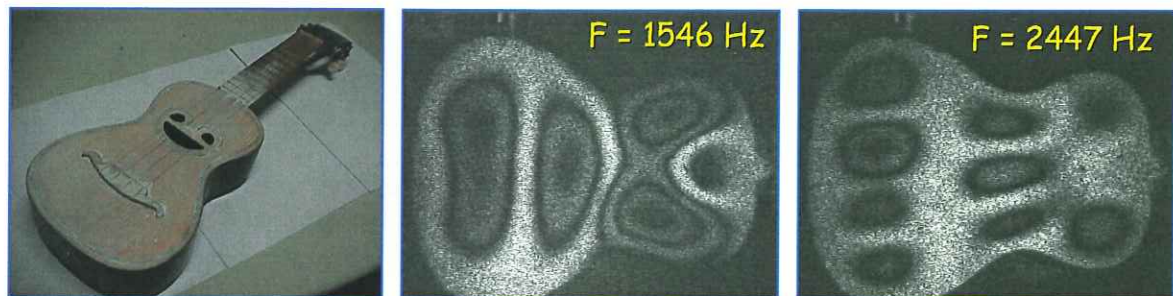


Fig. 2 Eigenmodes of a Portuguese Mandolin

Shearography for NDT inspection

The Shearography techniques are a special case of holographic interferometry in which the two speckled wavefronts, that interfere, are at the same time reference and object waves. In this case the resulting fringe patterns correspond to displacement gradients distribution instead of the displacements itself. These measurements can be very useful in the detection of localized gradients due to the presence of defects. To get full advantage of this technique in industrial environments the optical set-ups should be adapted to record information in a few microseconds. The use of pulsed lasers diminishes drastically the influence of any environmental perturbation on the final results. In this case a fast rate dynamic excitation source should be available. Some results are presented on fig.3 corresponding to a defected sandwich structure that was tested using an electronic striker to generate a bending wave propagation along the object surface.

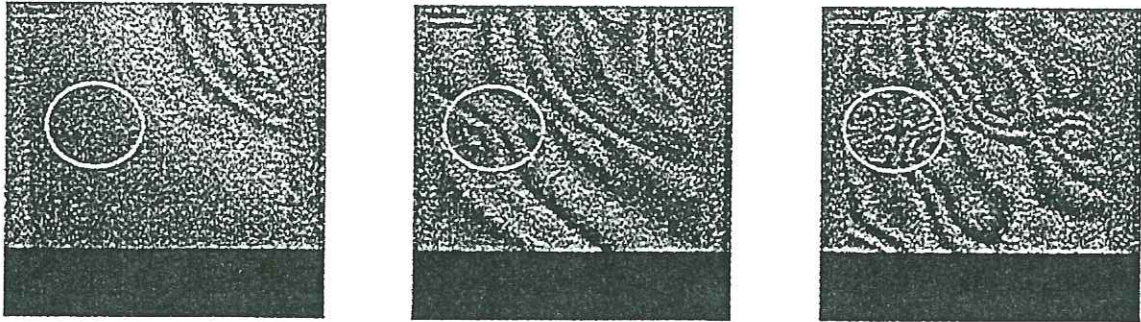


Fig 3 Phase maps obtained from shearographic recordings with shock excitation a) 25 μ s, b) 60 μ s and c) 205 μ s after impact.

In the results presented in fig. 3 is perfectly visible the presence of a localized gradient in the area corresponding to the defect.

Conclusions

The holographic interferometry techniques are very useful for Experimental Mechanics and NDT inspection of structures. Pulsed techniques can be applied whenever dynamic excitation may arise. Image processing techniques can be used to improve the experimental data analysis.

References

- [1]-Powell, R.L.; Stetson, K. A.; "Interferometric Vibration Analysis by Wavefront Reconstruction", Journal of Optical Soc. Of America, Vol. 55, n^o12, pp. 1593-1598, 1965.
- [2]-Creath, K.; Sletmoen, A.G.; "Vibration-Observation Techniques for Digital Speckle Pattern Interferometry", Journal of Optical Soc. Of America, Vol.2, n^o10, pp. 1629-1636, 1985.
- [3]-Vikagen, E.; "Vibration Measurement Using Phase-Shifting TV-Holography and Digital Image Processing", Optics Communications, Vol. 69, n^o 34, pp. 214-218, 1989.
- [4]-Aleksoff, C.C.; "Temporally Modulated Holography", Applied Optics, Vol.10, n^o6, pp.1329-1341, 1971.